Observational study of thundercloud radiation bursts using a segmented organic scintillator installed at a mountaintop

26   12

Abstract

Long-duration radiation bursts related to thunderclouds were observed at Norikura Observatory (2,770 m above sea level) of The Institute for Cosmic Ray Research, The University of Tokyo in 2014 using a segmented organic scintillator originally developed as an antineutrino detector for reactor monitoring. 12 bursts were observed in 54 days and the energy spectra extended up to 10 - 25 MeV. According to thunder information, the bursts seemed to be related to thunder activity. Besides, two types of burst termination were observed in a short interval, which suggested that long-duration bursts could terminate simultaneously with lightning discharges.

In addition, the energy and height of runaway electron sources in thunderclouds were estimated by Monte Carlo simulation. The estimated energies of 12 bursts were higher than those of 3 bursts observed at Ohi Power Station located in the coastal area of the Sea of Japan. On the other hand, the estimated flux of runaway electrons at the source height was remarkably smaller at Norikura Observatory than at Ohi Power Station. The difference of bursts between two locations might imply the existence of unknown mechanisms of electron acceleration and multiplication process in thunderclouds.

Contents

List of Figures

List of Tables

xiii

Chapter 1

Introduction

1.1 Electron acceleration through electric field in thunderclouds

1.1.1 Basic idea and first observation of electron acceleration process

It is known that strong electric fields of the order of 100 kV/m exist in thunderclouds. Since C. T. R. Wilson suggested that electrons could be accelerated by the strong electric field in thunderclouds in 1920s [4, 5], a number of experiments have been performed with various approaches to observe the electron acceleration in thunderclouds.

A part of the electrons traversing through thunderclouds are accelerated by the strong electric field and imparted kinetic energy which can overcome the stopping power caused by collisions with air molecules. These electrons which reach relativistic energy are called "runaway electrons" and are considered to produce radiation X-rays/gamma-rays in the air through bremsstrahlung process. The bremsstrahlung X-rays of the energy of up to > 110 keV in association with lightning activities were actually detected from the aircraft flown into thunderclouds in 1980s [6, 7]. However, the count rate of X-rays observed in these measurement turned out to be significantly higher than expected from the acceleration of the electrons originated from atmospheric radionuclides and cosmic ray secondaries [8].

1.1.2 Behavior of electrons in the air

An electron traversing through the air experiences the stopping power by inelastic collisions with air molecules which cause ionization or atomic excitation. This stopping power by ionization is described by the well-known Bethe's equation for electrons [9]:

$$
-\left\langle \frac{d\epsilon}{dx} \right\rangle_{\text{ion}} = \rho \frac{1}{2} K \frac{Z}{A} \frac{1}{\beta^2} \left[\ln \frac{m_e c^2 \beta^2 \gamma^2 \{m_e c^2 (\gamma-1)/2\}}{I^2} \right.
$$
$$
\left. + (1-\beta^2) - \frac{2\gamma-1}{\gamma^2} \ln 2 + \frac{1}{8} \left(\frac{\gamma-1}{\gamma} \right)^2 - \delta \right], \quad (1.1)
$$

where ρ is the density of medium ($\rho_{\text{air}} = 1.293 \times 10^{-6}$[g/cm^3] at STP), Z is the atomic number of medium ($Z_{\text{air}} = 7.2$), A is the atomic mass of medium ($A_{\text{air}} = 14.4$[g/mol]), $m_e c^2 = 0.511$ [MeV] is the electron mass and I is the mean excitation energy of medium ($I_{\text{air}} = 85.7 \times 10^{-6}$[MeV]). $K = 4\pi N_A r_e^2 m_e c^2 = 0.307$[MeVcm^2/mol], where $N_A = 6.022 \times 10^{23}$[/mol] is Avogadro's number and $r_e = 2.818 \times 10^{-15}$[m] is the classical electron radius. $\beta = v/c$ and $\gamma = 1/\sqrt{1-\beta^2}$. The density effect correction δ corresponds to the polarization of the medium by high energy incident electrons. δ effectively reduces the stopping power of incident electrons in the relativistic region above 30 MeV in the air.

The stopping power by ionization in the air at STP is plotted in Figure 1.1 as the blue dashed line. In non-relativistic region 10^{-2} - 10^0 MeV, the stopping power decreases proportionally to $\sim 1/\beta^2$ because faster incident electrons feel electric force of atomic electrons for shorter time. The stopping power by ionization gets minimum at around 1 MeV ("minimum ionization") and shows gradual increase in relativistic region corresponding to the logarithmic term $\sim \ln(\beta\gamma)^2$ in Equation (1.1). This so-called "relativistic rise" is due to the increase of the interaction cross section caused by extension of the transversal electric field of fast incident electrons.

High energy incident electrons also lose energy by radiative effects when passing near the atomic nuclei. The radiative energy loss by bremsstrahlung dominates the stopping power in the high energy region above 10^2 MeV in the air. The stopping power of bremsstrahlung is described as a function of

2

the kinetic energy of incident electrons [9]:

$$-\left\langle \frac{d\epsilon}{dx} \right\rangle_{\text{brems}} = \rho \frac{\epsilon}{X_0}, \tag{1.2}$$

where $X_0[\text{g/cm}^2]$ is the radiation length. X_0 is calculated by

$$\frac{1}{X_0} = 4\alpha r_e^2 \frac{N_A}{A} \left\{ Z^2 \left[L_{\text{rad}} - f(Z) \right] + Z L'_{\text{rad}} \right\}. \tag{1.3}$$

Here $\alpha = 1/137$ is the fine structure constant, $L_{\text{rad}} = \ln(184.15 Z^{-1/3})$ and $L'_{\text{rad}} = \ln(1194 Z^{-2/3})$ are Tsai's radiation logarithm for $Z > 4$ [10]. The function $f(Z)$ can be obtained from

$$f(Z) = a^2 \left[(1+a^2)^{-1} + 0.20206 - 0.0369a^2 + 0.0083a^4 - 0.002a^6 \right], \tag{1.4}$$

where $a = \alpha Z$. The stopping power by bremsstrahlung in the air at STP is plotted in Figure 1.1 as the green dashed line. The stopping power by bremsstrahlung increases proportionally to the energy of incident electrons.

Consequently, the total stopping power of electrons traversing through the air can be obtained from the summation of those of ionization and bremsstrahlung (Equation (1.1) and (1.2)):

$$\left\langle \frac{d\epsilon}{dx} \right\rangle_{\text{tot}} = \left\langle \frac{d\epsilon}{dx} \right\rangle_{\text{ion}} + \left\langle \frac{d\epsilon}{dx} \right\rangle_{\text{brems}}, \tag{1.5}$$

which is plotted as the red solid line in Figure 1.1.

1.1.3 Relativistic runaway electron avalanche mechanism

To explain the intensive bremsstrahlung X-ray enhancements observed in [6, 7], an avalanche-type multiplication model of relativistic runaway electrons was proposed by Gurevich *et al.* in 1992 [11], which is so-called relativistic runaway electron avalanche (RREA) mechanism.

The change of electron energy $d\epsilon$ through travel length dx in an electric field is described as

$$\frac{d\epsilon}{dx} = eE - F(\epsilon), \tag{1.6}$$

where E is the electric field strength and $F(\epsilon)$ is the stopping power of electrons, i.e.

$$F(\epsilon) = -\left\langle \frac{d\epsilon}{dx} \right\rangle_{\text{tot}}. \tag{1.7}$$

3
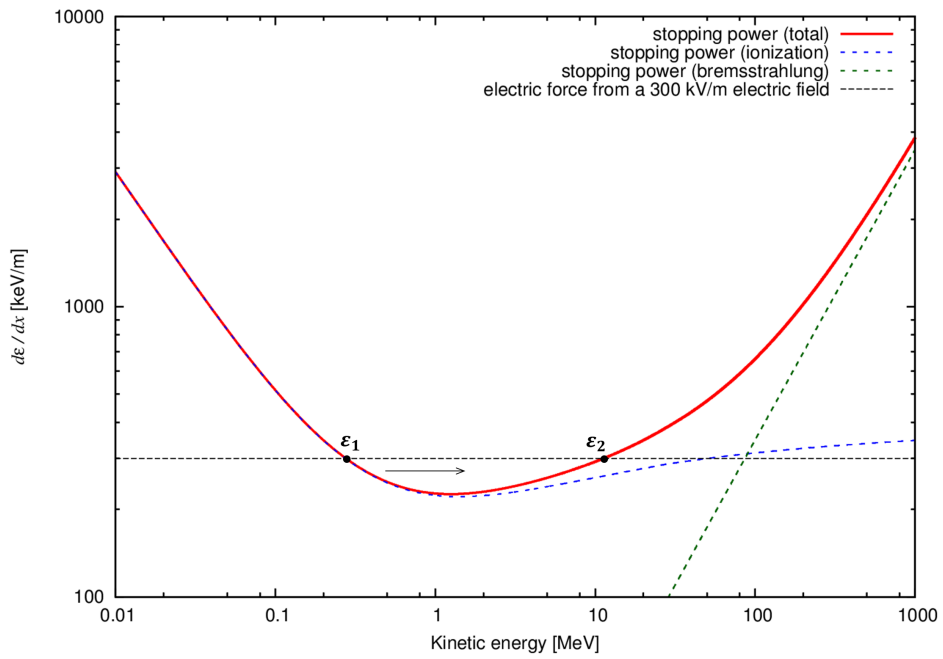
Figure 1.1: Stopping power (energy loss per unit length) of an electron moving through the air at STP : Blue and green dashed lines show the stopping power by ionization and bremsstrahlung respectively. Red solid line shows the total stopping power. For reference, electric force from 300 kV/m electric field is shown as black horizontal dashed line.

As described above, the stopping power (slowing-down force) as a function of the kinetic energy of electrons is plotted in Figure 1.1. When the energy loss in the air is smaller than the energy gain in an electric field ($eE > F(\epsilon)$), electrons can be accelerated and become relativistic runaway electrons.

The total stopping power by ionization and bremsstrahlung decreases with electron energy in non-relativistic region, while it increases in relativistic region. Therefore, the stopping power $F(\epsilon)$ has the minimum value F_{min} at a characteristic electron energy,

$$F_{min} = eE_{th}. \tag{1.8}$$

Here, $\epsilon \sim 1$ MeV and the threshold of the electric field which can produce runaway electrons is $E_{th} \sim 218$kV/m. According to the detailed simulation [12], the practical E_{th} at sea level is approximately 280 kV/m in the air at the standard condition. This 30% higher threshold of the electric field seems to be due to elastic scattering with air molecules, which was taken into account in the simulation.

In enough strong electric field $E > E_{th}$, an electron which has non-relativistic energy higher than ϵ_1 (shown in Figure 1.1) can be accelerated overcoming the slowing-down stopping power and reaches relativistic region as the arrow in Figure 1.1 shows. However, the electron energy cannot exceed a particular value in relativistic region ϵ_2 (aslo shown in Figure 1.1) because $F(\epsilon)$ surpasses eE again and thus the electron slows down to ϵ_2 emitting bremsstrahlung X-rays/gamma-rays. Consequently, electrons with energy $\epsilon > \epsilon_1$ reach the equilibrium state around $\epsilon = \epsilon_2$ after being accelerated by a strong electric field. In stronger electric fields, ϵ_1 becomes lower and ϵ_2 becomes higher.

Therefore in thunderclouds, "seed electrons" originated from cosmic ray secondaries or airborne radionuclides such as radon which have higher energy than ϵ_1 are accelerated to relativistic energy ϵ_2 by electric fields overcoming the stopping power and produce knock-on electrons out of air molecules. Some of the knock-on secondary electrons will have energy of higher than ϵ_1 and can be accelerated to relativistic energy by electric fields along with the primary runaway electrons. Through this acceleration process, avalanche-

type exponential increase of runaway electrons and accompanying production of bremsstrahlung X-rays/gamma-rays will occur in thunderclouds.

This RREA model is expected to account for the observed intensive radiation bursts in association with thundercloud activities and have been modified up to date with additional calculations or simulations such as [12, 13, 14, 15, 16].

1.2 Previous observation of radiation bursts related to lightning discharges or thunderclouds

Since RREA model was suggested, X-ray/gamma-ray enhancements in association with lightning discharges or thunderclouds have been reported repeatedly.

1.2.1 Long-duration bursts and short-duration bursts

Brief flashes of gamma-rays related to thunderstorms were first observed by BATSE detectors on the space observatory CGRO [17]. These short bursts are called terrestrial gamma-ray flashes (TGF) and it is noticed that the duration of TGF is about a few milliseconds and its energy is up to 20 - 40 MeV [18, 19, 20, 21].

Similar short gamma-ray bursts were also observed from the Earth's surface during natural lightning discharges [22, 23, 24, 25, 26] and rocket-triggered lightning discharges [27, 28, 29]. These short bursts last for a few milliseconds to a few hundred microseconds and seem to occur in association with lightning discharges.

On the other hand, a different type of radiation bursts which has relatively long duration have been observed by numerous experiments. Following the aircraft experiments [6, 7], an X-ray detector loaded on a balloon detected radiation enhancements lasting for approximately 1 minute [30]. These long duration bursts seem to occur in association with thunderclouds. Subsequently, long duration bursts were observed in the high-altitude mountaintop areas and the coastal area of Sea of Japan as described below.

1.2.2 Previous observation of long-duration bursts

Recently a number of radiation bursts related to thunderclouds were observed at high-altitude locations. At Gran Sasso (2,005 m above sea level), high energy gamma-ray bursts lasting for a few minutes which have energy of up to 10 MeV were observed with a NaI(TI) scintillator in perturbed weather [31]. On the other hand, X-ray bursts lasting for 1 - 5 minutes were observed during thunderstorms over a wide space region of about 0.5 km at Tien-Shan (3,340 m above sea level) [32].

Subsequently, several high-altitude experiments were performed at Baksan (1,700 m above sea level) [33], Mt. Norikura (2,770 m above sea level) [34, 35], Mt. Fuji (3,776 m above sea level) [36], Aragats (3,250 m above sea level) [37, 25, 38] and Yangbajing (4300 m above sea level) [39]. The experiment at Mt. Norikura performed by Tsuchiya *et al.* detected a gamma-ray burst which had an energy spectrum extending up to 10 MeV during thunderstorms [35]. At the top of Mt. Fuji, Torii *et al.* observed gradual increase of energetic radiation which seemed to be caused by a thunderstorm. It lasted for about 20 minutes and had a continuous energy spectrum extending up to 10MeV [36]. Furthermore, an especially prolonged intensive gamma-ray burst of up to 40 MeV lasting for about 40 minutes was observed in association with thunderclouds in Tibet [39].

Through these measurements at high altitudes, long bursts lasting for the order of a few seconds to tens of minutes are considered to be related to thunderclouds in contrast to the short bursts lasting for a few milliseconds such as TGFs which seem to be strongly related to lightning discharges. The mechanism of production of radiation bursts related to thunderclouds is being revealed gradually through these experiments.

In addition to observations at high-altitude mountaintops, several observation in the coastal area of the Sea of Japan have been performed. In this area, it is known that thunderclouds of tripole structure are formed at very low altitude in winter [40]. Radiation bursts in association with thunderclouds are considered to reach sea-level surface in this area as it happens at high-altitude locations.

In 2002, Torii *et al.* first reported that they analyzed the data of

monitoring posts of a nuclear facility and observed increases of environmental gamma-ray dose which seemed to be related to lightning activity [41, 42]. Subsequently, further experiments were carried out by Japanese groups [43, 44, 45, 46]. The observed radiation bursts accompanying thunderclouds lasted for more than a half minutes and the energy spectra extended up to 10 MeV, which are similar to the bursts observed at mountaintops and could be accounted for by RREA model [47].

Recently, a small antineutrino detector which we developed for reactor monitoring detected three gamma-ray bursts related to winter thunderclouds at the coast of the Sea of Japan. By taking advantage of its segmented structure, the antineutrino detector could successfully identify the arrival direction of the bursts [2] (described in 2.5).

1.3 Components of radiation bursts

Previous observations detected several kinds of particles such as electrons and neutrons along with X-rays/gamma-rays in radiation bursts coinciding with thunderclouds. The components of the radiation bursts are considered to be important in order to understand the mechanism of this thundercloud phenomenon.

1.3.1 Electron flux enhancement

As discussed above, radiation bursts are considered to be originated from accelerated runaway electrons in thunderclouds according to RREA model. Nevertheless, few observations could detect electron enhancements directly in association with thunderstorms due to relatively short range of electrons compared to gamma-rays in the air.

An irregular enhancement of cosmic ray secondaries including electrons was observed before lightning discharges by a large area air shower array situated in the high-altitude area of Baksan Valley in North Caucasus [33]. Subsequently, Tsuchiya *et al.* performed an experiment at Norikura Observatory using NaI and plastic scintillators. They detected electron signal enhancement accompanying a gamma-ray burst [35]. It was the first observation which detected both gamma-rays and electrons simultaneously by

8

anticoincidence of plastic scintillator. The source height of runaway electrons was estimated to be at 60 - 130 m (90 % confidence level) above ground level, and the primary runaway electrons accelerated in thunderclouds seemed to be dominant in number compared to the secondary electrons produced by bremsstrahlung photons.

Electron enhancements accompanying radiation bursts were also detected at the Aragats Space Environment Center [37]. Taking advantage of anticoincidence by multiple plastic scintillators, count rate enhancements of electrons of > 15 MeV were observed for a few minutes when thunderclouds were situated at approximately 100 - 200 m above the observatory. Relatively short distance of $\sim$100 m between the detector and the source of runaway electrons would be a key to detect electron components of radiation bursts directly.

1.3.2 Neutron generation in thunderclouds

Several experiments observed neutron flux enhancements in association with thundercloud activities since it was first reported in 1985 [48], where neutrons were observed by gas-discharge neutron counters installed at Gulmarg (altitude 2,743 m). Following this first detection of neutron flux enhancements, experiments at Mumbai [49], Mt. Norikura [34], Aragats [37, 25, 38], Tien-Shan [50], Yangbajing [39], Yakutsk [51] and other experiments also observed neutron enhancements related to thunderclouds.

Although neutron flux enhancements in association with thunderstorms have been observed by numerous experiments using neutron counters, the mechanism of neutron production in thunderclouds is still unclear. Neutron production in thunderclouds not only have important information on the mechanism of lightning discharges, but it might affect the reliability of ^{14}C dating significantly [52, 53].

Nuclear fusion reaction in the air ^{2}H(^{2}H, n)^{3}He had been thought to be responsible for observed neutron enhancements since decades ago [52], until it turned out to be unlikely to take place under the realistic physical conditions of observed thunderclouds. Instead, photonuclear reaction $(\gamma, \mathrm{X}n)$ such as $\gamma(^{14}$N, 1n)^{13}N or $\gamma(^{16}$O, 1n)^{15}O was stated as a convincing mecha-

nism of neutron production in thunderclouds [54]. The threshold of gamma-ray energy for the photonuclear reaction are 10.5 MeV for $\gamma(^{14}\text{N}, 1\text{n})^{13}\text{N}$ and 15.7 MeV for $\gamma(^{16}\text{O}, 1\text{n})^{15}\text{O}$ [55], which are relatively realistic energy in radiation bursts observed in association with thunderclouds. Although this model is still under debate [50, 56], further calculation have been performed recently that neutron generation in thunderclouds are primarily attributed to photonuclear reaction compared to other reactions such as nuclear fusion, electrodisintegration or inverse to beta decay reaction $e^-(p^+, n)\nu_e$ [57, 58].

In spite of the necessity of verification about these neutron production processes, most of previous observations of neutron enhancements related to thunderstorms are not sufficiently substantiated because they used gas-discharge neutron counters which would have sensitivity to high energy gamma-rays of the radiation bursts [38, 56, 59]. Thus neutron detection in a radiation burst by delayed coincidence method at Ohi Power Station was a remarkable result [2] (described in 2.5).

1.4 Mountaintop experiments using scintillation detectors

Here we refer to previous experiments which had common aspects with our experiment at Norikura Observatory. In these previous experiments, scintillation detectors were installed at the top of mountains in order to observe radiation bursts from thunderclouds.

The experiment performed at the top of Mt. Norikura [35] detected signal enhancement of both gamma-rays and electrons at the same time in association with thunderclouds. A spherical NaI scintillator with a diameter of 7.62 cm, which had the sensitivity between 10 keV and 12 MeV, was placed underneath a plastic scintillator of 45 cm × 40 cm × 0.5 cm, which had the sensitivity above 500 keV. Both scintillators were installed in an aluminum box outside the building. Since the thin plastic scintillator was mainly sensitive to charged particles, gamma-rays and electrons could be discriminated by anticoincidence of the NaI and plastic scintillators. A light sensor and a field mill were also installed outside the building.

This experiment was performed at Norikura Observatory for approxi-

mately one month in summer 2008. They observed one long-duration bursts related to thundercloud activity, which lasted for more than 90 seconds with the signal enhancements on both the NaI and plastic scintillators. It was suggested from anticoincidence analysis that the NaI scintillator detected gamma-ray components while the plastic scintillator detected electron components of the burst. Although the light sensor did not detect a lightning, the field mill showed a sudden and rapid change of the polarity from negative overflow (below -100 kV/m) to positive overflow (above 100 kV/m) during the signal enhancement. Thus, they concluded that no lightning occurred during the bursts and it was caused by thunderclouds. By utilizing the gamma-ray spectrum obtained from the NaI scintillator, the distance through which the bremsstrahlung photons emitted from a thundercloud propagated was estimated to be 90 m from the detectors. This result indicated that the plastic scintillator could detect runaway electrons accelerated in thunderclouds directly because thunderclouds passed through near the detector.

Another experiment was also performed in 2008 at the top of Mt. Fuji [36]. A cylindrical NaI scintillator with both a diameter and a width of 12.7 cm was used, whose sensitivity was set to 150 keV - 23 MeV. In this experiment, three thundercloud radiation bursts which had the maximum duration of about 20 minutes were reported.

In comparison with these previous experiments, our detector could take advantage of its larger volume of the scintillator. Our segmented plastic scintillator of 80 cm $\times$ 80 cm $\times$ 100 cm had wider energy range of sensitivity and was expected to reveal unknown aspects of thundercloud radiation bursts. Furthermore, detecting many radiation bursts as possible at Norikura Observatory would enable us to compare with the result of the previous experiment at Ohi Power Station [2] which was obtained from the former prototype of our antineutrino detector.

11

Chapter 2

PANDA project

2.1 Reactor monitoring using an antineutrino detector

International Atomic Energy Agency (IAEA) proposed a new reactor monitoring method based on antineutrino detection technique [60]. To prevent nuclear technology from being utilized for the purpose of developing nuclear weapons, IAEA operates inspection of nuclear facilities around the world. However, the inspection includes some intrusive techniques, such as reactor monitoring at very close distance from the reactor core, and is a burden to both the nuclear facilities and IAEA.

Neutrinos cannot be shielded because their interaction cross section with matters is quite small. Besides, deploying an intensive antineutrino source comparable to a reactor is almost impossible. It means that by monitoring antineutrinos emitted from the core during reactor operation, the status of the reactor and fuels could be monitored even from outside of the reactor building. Therefore, an antineutrino detector might become an epoch-making tool for IAEA's inspection in the near future. A number of antineutrino detectors has been developed by various groups for this new reactor monitoring method [61, 62].

2.2 Reactor antineutrino

Since F. Reines and C. Cowan *et al.* first discovered antineutrinos in 1950s [63], reactors have contributed to particle physics as important neutrino sources.

Antineutrinos are emitted from β decay process of neutron-rich nuclei which are produced by nuclear fission of uranium and plutonium contained in the reactor fuel.

$$^{235}\mathrm{U} + \mathrm{n} \rightarrow \mathrm{X}_1 + \mathrm{X}_2 + \cdots + \mathrm{n} + \mathrm{n} + \cdots \tag{2.1}$$

$$^{A}_{Z}\mathrm{X} \rightarrow ^{A}_{Z+1}\mathrm{X}' + \mathrm{e}^- + \bar{\nu}_\mathrm{e} \tag{2.2}$$

$$^{A}_{Z+1}\mathrm{X}' \rightarrow ^{A}_{Z+2}\mathrm{X}'' + \cdots \tag{2.3}$$
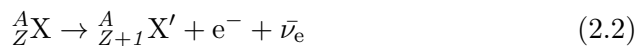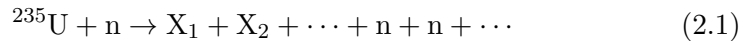
The flux of antineutrino from a reactor core is huge, e.g. 6×10^{20} antineutrinos are emitted every second from a regular size commercial reactor whose output energy is about 3 GW_{th}. The ability of reactor monitoring using an antineutrino detector was first shown by Klimov *et al.* in 1980s [64], which led to IAEA's proposition.

2.3 Plastic Anti-Neutrino Detector Array

2.3.1 Feature of PANDA

In order to develop a "non-intrusive" inspection tool using a small antineutrino detector, our group launched PANDA (Plastic Anti-Neutrino Detector Array) Project in 2008 (Figure 2.1). An important feature of PANDA is that liquid scintillator is not used as its target material. Liquid scintillator is flammable, so that it is difficult to be deployed in nuclear facilities for security reason. PANDA consists of less flammable plastic scintillator instead of liquid scintillator, which makes PANDA practical for deployment in nuclear facilities.

The segmented structure is another important feature of PANDA. We can know the position of energy deposits by taking advantage of the array structure of optically independent plastic scintillator bars. The geometric information gives PANDA an ability to reject background events effectively.

In addition, PANDA is designed to have high mobility. PANDA can be loaded on a 2 ton van or a 12 feet container along with data acquisition system and water shield. It enables us unmanned operation without deploying

13

the detector out of the vehicle. The high mobility allows easy and quick setup of the detector at nuclear facilities, which is also required for practical reactor monitoring.
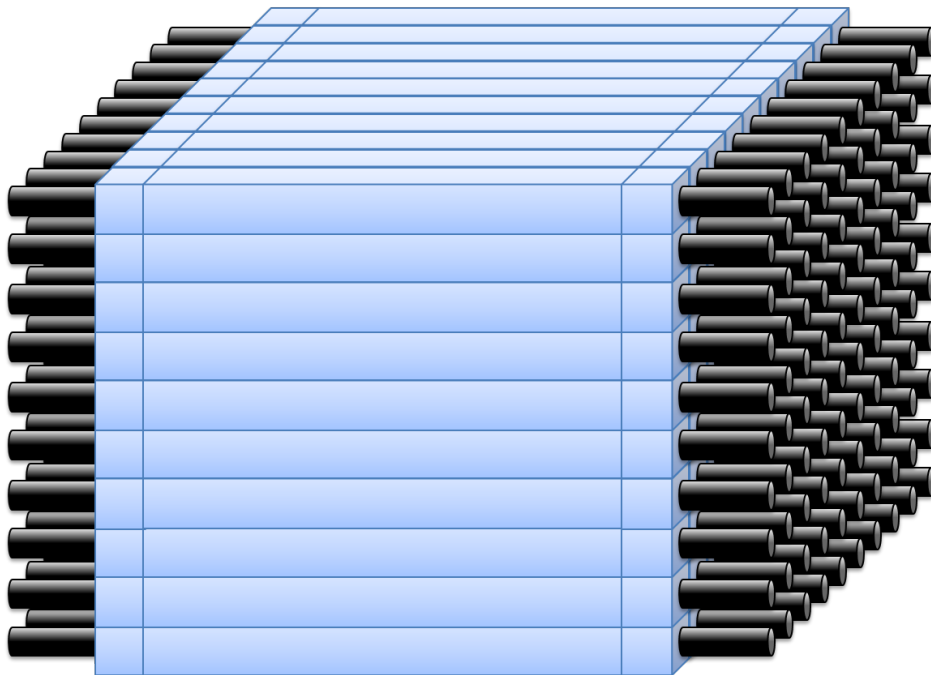
Figure 2.1: Plastic Anti-Neutrino Detector Array (PANDA) : PANDA consists of 10×10 optically independent plastic scintillator bars.

2.3.2 PANDA modules

PANDA consists of 100 plastic scintillator bars of 10 cm×10 cm×100 cm (ELJEN Technology EJ-200 or Rexon Technology RP-408) and the target mass is about 1 ton. Cubic acrylic light guides and 2-inch Hamamatsu H6410 (R329-02) PMTs are attached on both ends of each plastic scintillator, composing a PANDA module as shown in Figure 2.2.

PANDA module is wrapped with aluminized mylar film for reflection along with gadolinium containing PET film of Ask Sanshin Engineering (Figure 2.3). Optical cement (ELJEN Technology EJ-500) is used for gluing plastic scintillators, light guides and PMTs, which has enough strength for overland transportation. The components of the PANDA modules are shown

in Table 2.1.

Table 2.1: List of the components of PANDA modules

PANDA module components	Model
10 kg Plastic scintillator	ELJEN Technology EJ-200 or Rexon Technology RP-408
1 kg acrylic cubic light guide	custom-made
2-inch PMT	Hamamatsu Photonics H6410 (R329-02)
Optical cement	ELJEN Technology EJ-500
Gadolinium-oxide coated PET film	Ask Sanshin Engineering
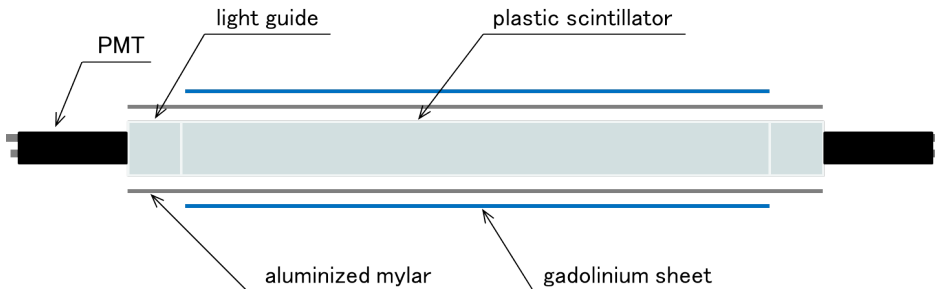
Figure 2.2: Structure of a PANDA module

2.3.3 Delayed coincidence

Antineutrinos emitted from reactors can be detected via inverse β decay interaction with protons in the plastic scintillator.

$$\bar{\nu}_e + p \rightarrow e^+ + n \tag{2.4}$$

The positron emitted by the inverse β decay causes ionization and annihilation immediately, both of which are detected as a prompt signal. A prompt signal is expected to include a pair of characteristic gamma-rays of 511 keV emitted by annihilation.

$$e^+ + e^- \rightarrow 2\gamma \tag{2.5}$$

15

Figure 2.3: Development of PANDA modules

16

On the other hand, the neutron produced by inverse β decay is thermalized gradually and finally captured by gadolinium surrounding plastic scintillators. Several gamma-rays with the total energy of approximately 8 MeV emitted by the neutron capture are detected as a delayed signal.

$$n +^{155} \text{Gd} \rightarrow^{156} \text{Gd}^* \rightarrow^{156} \text{Gd} + \gamma' \text{s} \qquad (2.6)$$

$$n +^{157} \text{Gd} \rightarrow^{158} \text{Gd}^* \rightarrow^{158} \text{Gd} + \gamma' \text{s} \qquad (2.7)$$

When an inverse β decay occurs in plastic scintillator, a pair of a prompt signal and a delayed signal is detected within a short time interval. This is called delayed coincidence technique. It rejects most background events such as environmental gamma-rays and enables effective antineutrino detection.

2.3.4   Neutron capture by gadolinium

The gadolinium sheet wrapped around plastic scintillators consists of two layers of 25 μm-thick gadolinium oxide applied on the both sides of 50 μm-thick PET film. The density of gadolinium included in the sheet was 4.9 mg/cm^2.

A Monte Carlo simulation of neutron capture showed that the performance of gadolinium sheet wrapped around plastic scintillator was comparable to gadolinium-doped plastic scintillator [65]. This simulation was performed by generating neutrons of 10 keV inside PANDA. The efficiency and the mean capture time of neutrons by gadolinium sheet wrapped around plastic scintillator were 76.0 % and 62.4 μs respectively, while they were 89.4 % and 28.4 μs for gadolinium-doped plastic scintillator.

2.3.5   Size and mobility

The size of PANDA detector is about 1.5 m×1.5 m×2.0 m and can be loaded on a 2 ton van directly. In case that 20 cm-thick water shield is required to suppress background events, a 12 feet container should be used for transportation. PANDA is wired before transportation and can start operation immediately after arrival at a nuclear facility.

2.4 Reactor monitoring using PANDA prototypes

Before developing the full-size PANDA which has 100 plastic scintillator bars, several prototypes have been developed using less number of modules in order to find out potential problems and improve the project.

2.4.1 Prototype I : LesserPANDA

The first prototype, LesserPANDA, was developed in 2010. It consisted of 16 (4×4) modules and the target mass was about 160 kg (Figure 2.4). LesserPANDA did not have active or passive shields for background rejection, therefore could be loaded on a 2 ton van easily as shown in Figure 2.5. The van was transported to Hamaoka Nuclear Power Plant of Chubu Electric Power Co., Inc. in March 2011. LesserPANDA started operation for antineutrino measurement by the reactor building of Unit 3 (3.3 GW$_{th}$) at the distance of 39.8 m from the reactor core (Figure 2.6).

Although we could not complete this plan because of the 2011 Tohoku earthquake off the Pacific coast of Japan, the background data could be taken for two months and the ability of unmanned operation outside of the reactor building was shown [65].

2.4.2 Prototype II : PANDA36

After the measurement at Hamaoka Nuclear Power Plant using Lesser-PANDA, we started development of the second prototype PANDA36. It consisted of 36 (6×6) plastic scintillator bars which weighed about 360 kg in total (Figure 2.7). PANDA36 was developed based on LesserPANDA with several improvements on both the hardware and the software. The improvements included development of FPGA for the data acquisition system, which enabled more complex trigger selection.

In November 2011, PANDA36 was loaded on a van and transported to Ohi Power Station of Kansai Electric Power Co., Inc (Figure 2.8). PANDA36 was deployed near the reactor building of Unit 2, which has 3.4 GW$_{th}$ output (Figure 2.9). The distance between PANDA36 and the reactor core was

Figure 2.4: The first prototype (LesserPANDA) : LesserPANDA consisted of 16 modules.

Figure 2.5: LesserPANDA being loaded on a van

Figure 2.6: LesserPANDA deployed at Hamaoka Nuclear Power Plant

35.9 m as shown in Figure 2.10, and the measurement had been operated for about two months till January 2012. Neutrino data were taken for 28 days until the shutdown of Unit 2 on December 16th, and then background data were taken for 33 days after the shutdown.

After subtraction of background period, the neutrino flux of 21.8 ± 11.4 events per day ($\approx 2\,\sigma$) was observed during the reactor operation period. It was the first result which succeeded in antineutrino detection using a small antineutrino detector from aboveground surface outside of reactor buildings [66].

Figure 2.7: The second prototype PANDA36 consisted of 36 modules.

2.5   Analysis of radiation bursts

Not only antineutrinos, PANDA36 detected some interesting flux enhancements during the measurement at Ohi Power Plant [2]. These enhancements seemed to be related to thunderclouds.

Figure 2.8: PANDA36 loaded on a 2 ton van before transportation to Ohi Power Station

2.5.1 Detection of radiation enhancements at Ohi

Three candidates of radiation bursts were found in the data taken at Ohi Power Station for two months from November 2011 to January 2012. Since these bursts were observed in coincidence with existence of thunderclouds, they were considered to be radiation bursts associated with winter thunderclouds. The duration of these bursts were 60 to 180 seconds and the energy spectra extended up to 15 MeV, which were in good agreement with the radiation bursts related to winter thunderclouds previously observed in the coastal area of the Sea of Japan [41, 42, 43, 44, 45, 46].

2.5.2 Source and arrival direction of bursts

Monte Carlo simulation was performed in order to determine the energy and height of possible monochromatic electron sources in thunderclouds which could well reproduce the observed energy spectra. The simulation result showed that the most likely monochromatic energy of runaway electrons at the source was 16 MeV and the height of the source were 400 to 1000 m

Figure 2.9: PANDA36 at Ohi Power Station
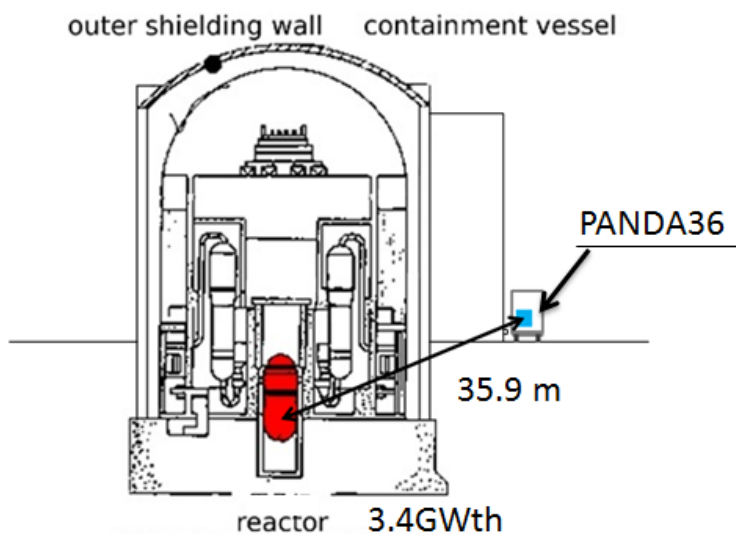
Figure 2.10: Distance between PANDA36 and the reactor core

for three observed bursts. The energy spectra reproduced by the simulation were in good agreement with the observed spectra.

In addition, the arrival direction of the bursts was analyzed. The comparison with the simulated spectra of gamma-rays isotropically shot to PANDA36 and the analysis of Compton scattering taking advantage of the geometric information of energy deposit indicated that the radiation bursts arrived from upward direction close to the zenith and the direction stayed constant during the burst period lasting for 60 - 180 minutes.

2.5.3   Neutron detection in bursts

In PANDA36, an incident neutron loses energy by multiple scattering with protons in the plastic scintillator and several gamma-rays of the total energy of approximately 8 MeV are emitted when captured by gadolinium after thermalization. Therefore, neutrons can be detected using the delayed coincidence method in the same way as the antineutrino detection described in 2.3.3.

As a result of the delayed coincidence analysis, a significant neutron flux of 14 ± 5 events per seconds were observed during one of three radiation bursts.

Chapter 3

Development of PANDA64

3.1 Detector of PANDA64

As the third prototype of PANDA project, PANDA64 was developed in 2012 (Figure 3.1). PANDA64 consists of 64 (8×8) modules and is the final prototype for development of the full-size detector PANDA100 (10×10 modules).

PANDA64 has some improvements compared to the former prototypes, LesserPANDA and PANDA36. The framework of the detector was designed based on the strength recalculation of each aluminum frames. In addition, 20 cm-thick water shield was installed on all sides of the detector in order to reduce the number of fast neutrons which were the primary background events of the measurement at Ohi Power Station. PANDA64 was designed to be loaded on a 12 feet container along with the water shield as shown in Figure 3.2.

3.2 Data acquisition system of PANDA64

The data acquisition system of PANDA64 was developed based on that of PANDA36. In order to take coincidence of trigger signals among 128 PMTs, two FPGA boards were developed using CAEN V1495. These newly developed FPGAs can take coincidence among up to 256 signals, therefore could be used for PANDA100 in the future without redesign.

The schematic view and the components of the data acquisition system are shown in Figure 3.3 and Table 3.1 respectively. The high voltage supplied

Figure 3.1: The third prototype PANDA64 consists of 64 modules. Red circle shows a slit for calibration sources.

Figure 3.2: PANDA64 and water shield loaded on a 12 feet container

to PMTs (Hamamatsu Photonics H6410) by Matsusada HARb-3*200 are divided by appropriate resistances to have similar gain values for each PMT. The signal obtained from a PMT is split into two signals (0.16:0.84) by a signal divider. The smaller signal (16% of the PMT output) is sent to 32ch charge ADC (CAEN V792) through a 30 m cable which enables 150 ns delay. The other larger signal (84% of the PMT output) is sent to 16ch discriminator (CAEN V895) through a 7 m cable, and then the signals higher than the threshold of discriminators are sent to two FPGA boards (CAEN V1495). The FPGAs take coincidence with the left and right PMTs of each module at first, and take coincidence again among all 64 modules to calculate the number of modules triggered at the same time. After applying the trigger condition, a gate signal of 400 ns width is generated in the FPGA and sent to ADCs before the delayed PMT signals arrive at ADC. ADCs convert analog PMT signals to digital outputs of 0 to 4095 channels and transfer them to the PC. Data are recorded as binary ROOT files.

The measurement program was also modified to deal with the high trigger rate due to the larger target size. The second prototype PANDA36 had a problem with the speed of data acquisition because of high trigger rate. Therefore the strict trigger condition was applied to PANDA36, which was

'gate signals are triggered when two or more modules of inner 16 modules have simultaneous signals'. However, PANDA64 cannot deal with the increasing trigger rate caused by the larger target size even if applying the same strict condition using inner 36 modules.

To reduce the size of the data transferred between ADC and PC, zero suppression was applied to the output of ADC. Zero suppression ignores signals with the energy deposit smaller than a constant threshold to enable fast transfer speed. By using water shield (described in 3.1) and ADC zero suppression simultaneously, data can be taken with the most relaxed trigger condition, which is 'gate signals are triggered when one or more modules of all 64 modules have energy deposits'.
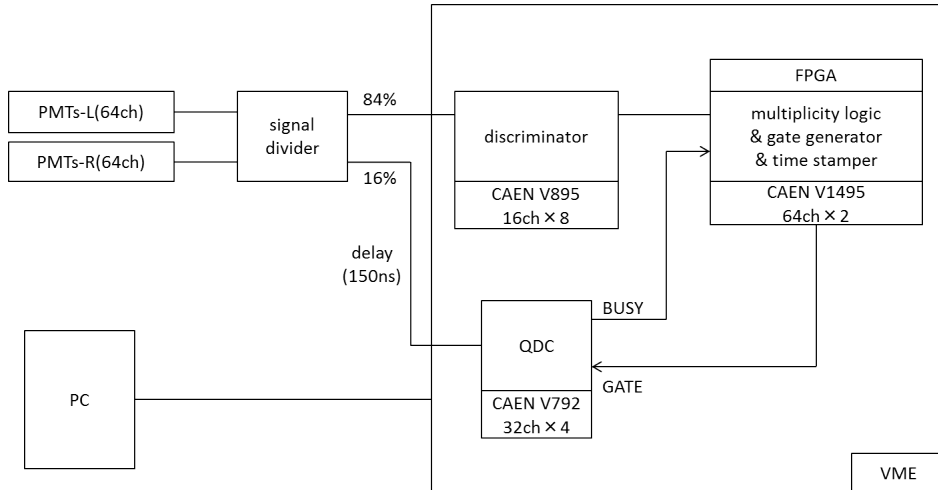
Figure 3.3: Schematic view of data acquisition system for PANDA64

3.3 Performance of PANDA64 and prospects of reactor monitoring

The performance of antineutrino detection by PANDA64 is expected to become remarkably better than PANDA36 due to installation of the water shield and ADC zero suppression. The detection efficiency of inverse β de-

Table 3.1: List of the components of PANDA64 data acquisition system

DAQ components	Model
3 kV high voltage power supply	Matsusada Precision HARb-3*200
General purpose VME board FPGA	CAEN V1495
-Piggyback of V1495	CAEN A395A, A395C
16ch leading edge discriminator	CAEN V895
32ch multievent QDC	CAEN V792
24ch delay cable box (150ns)	custom-made
	by REPIC CORPORATION

cay was 3.15 % for PANDA36, which will improve up to 9.11 % for PANDA64 when the most relaxed trigger condition is applied (Table 3.2). The most relaxed trigger condition means that a gate signal from the FPGA is generated when one or more modules of all 64 modules are triggered.

Assuming the condition of the measurement at Ohi Power Station in 2011, i.e. deployed at the surface outside the building at 35.9 m away from the reactor core whose thermal output is 3.4 GW_{th}, PANDA64 is expected to be capable of detecting the change in antineutrino flux between reactor operation period and shutdown period with the significance of 3 σ in less than respectively 5 days of both periods.

The development of PANDA64 has already been completed and we are ready for the next antineutrino measurement in order to proceed to the next step of reactor monitoring.

Table 3.2: Efficiency corresponding to each prototype and trigger condition

Prototype	Trigger condition	Efficiency
PANDA36	2 or more of inner 16 modules (strict)	3.15 %
PANDA64	2 or more of inner 36 modules (strict)	6.21 %
PANDA64	1 or more of all 64 modules (relaxed)	9.11 %

Chapter 4

Measurement at Norikura Observatory

Although PANDA prototypes have been developed for the purpose of reactor monitoring, PANDA also have sufficient ability to observe radiation bursts associated with thunderclouds as described in 2.5. In order to carry out further observational study of thundercloud radiation bursts, the third prototype PANDA64 was deployed at Norikura Observatory of the Institute for Cosmic Ray Research, the University of Tokyo in 2014.

4.1 Setup for mountaintop experiment

4.1.1 Detector settings

The water shield should not be installed around the detector for observation of radiation bursts related to thunderclouds at the mountaintop. It is because neutrons could be also an important target of the measurement, although they are considered to be the primary background events for reactor monitoring. Without 20 cm-thick water shield, PANDA64 can be loaded on a 2 ton van (Figure 4.1) and transported easily to the mountaintop observatory.

4.1.2 Electric field sensor

Some previous observations showed that the radiation bursts associated with thunderclouds are related to sudden fluctuation of electric field in the atmosphere from negative to positive or reverse direction. To investigate the

Figure 4.1: PANDA64 loaded on a van without water shield

correlation of radiation bursts and electric field, the electric field around the detector was recorded using a field mill (BOLTEK EFM-100). Negative electric field means the field where negatively charged particles are accelerated downward from thunderclouds to ground surface.

The measurement range of the field mill was set from -100 kV/m to 100 kV/m with the resolution of 50 V/m. Data were taken every second by a data logger (HIOKI E.E. CORPORATION LR8401) with output voltage between -20 V and 20 V.

4.1.3 Light sensor for lightning detection

It is also useful to investigate the correlation between lightning discharges and radiation bursts. A light sensor was developed using Si PIN photodiodes (Hamamatsu Photonics S1722-02) for lightning detection, which can extend the pulse signal of lightning to more than one second. It was connected to the data logger and the output voltage was monitored every second simultaneously with the electric field.

4.2 Configuration of data acquisition system

Water shields were not installed for the experiment at Norikura Observatory in order to detect as many neutron events as possible, which resulted in quite high trigger rate. On the other hand, charged particles such as electrons were expected to deposit most of their energy at outer modules where they pass first. It means that the strict trigger condition, e.g. 'two or more of inner modules have energy deposit simultaneously' applied to PANDA36, is not appropriate for electron detection.

Although the speed of the data acquisition drastically improved compared to PANDA36, we still had to maintain the trigger rate without water shield because the maximal trigger rate of PANDA64 for stable data acquisition with less than 10 % of dead time is approximately 13 kHz. Otherwise, the trigger rate increases up to 30 kHz without the water shield when the most relaxed trigger condition 'one or more modules have energy deposit' is applied.

Therefore, the threshold of discriminators (CAEN V895) was raised in order to deal with such high trigger rate. A signal from a PMT is split into two (0.16:0.84) by a signal divider and the smaller signal is sent to a discriminator which have a configurable threshold value. Because it was the catalogue value of the minimum threshold, 15mV was used for antineutrino measurement by PANDA36 to detect as lower energy deposit as possible. By raising this threshold, the trigger rate can be suppressed to a stable level even if the most relaxed trigger condition is applied.

Consequently, the threshold of discriminators was set to 150 mV for the measurement at Norikura Observatory taking the possibility into account that the trigger rate would increase during the burst period. This threshold could suppress the trigger rate to less than 7 kHz at the mountaintop and thus enabled the stable data acquisition. This threshold corresponded to the energy deposit of about 900 keV gamma-rays which hit on the far edge of the plastic scintillator. It means that an event which one or more modules had energy deposit of more than 1 MeV could trigger a gate signal without being ignored by discriminators.

4.3 Installation of PANDA64 at Norikura Observatory

4.3.1 Norikura Observatory

Norikura Observatory located in Gifu Prefecture in Japan is an experimental facility belonging to the Institute for Cosmic Ray Research (ICRR), the University of Tokyo. It stands at the top of Mt. Norikura (36'06 N, 137'33 E) and the altitude is 2,770 m above sea level (Figure 4.2). The observatory is open only in summer from July till the end of September. Radiation bursts related to thunderclouds were previously observed at this observatory by several Japanese groups in 2000s as described in 1.2.2.

PANDA64 loaded on a van was transported to Norikura Observatory on 7 July 2014 and deployed at approximately 20 m away from the building (Figure 4.3). The AC power supply and the network were provided by Norikura Observatory via the cables buried under the ground.

Figure 4.2: Norikura Observatory located at Mt. Norikura (2,770 m above sea level)

Figure 4.3: Deployment of PANDA64 and the field mill

4.3.2 Setup for measurement

Immediately after PANDA64 arrived at Norikura Observatory, the setup for measurement was carried out. The power supply cable and the network cable were laid under the ground between the van and the building, the field mill was installed at approximately 10 m away from the detector, while the light sensor was put on the roof of the driver's seat of the van (Figure 4.4). All the preparation for the measurement were completed in 5 hours even though it was windy and rainy.

The observation period was 30 days from July 7th to August 5th, 23 days from August 20th to September 11th and 12 days from September 16th to 27th. The total measurement period except for some test periods was 54 days. Two-week suspension of the measurement from August 6th was the closure period of the observatory, and 4 days suspension from September 12th was due to the scheduled periodic inspection of the van. Except for several visits to the observatory about once a week to change the HDD for data collection, the observation was done under unmanned operation.

Figure 4.4: Field mill (left) and light sensor (right)

4.4 Detector monitoring

During the unmanned operation at Norikura Observatory, the status of the surroundings and a part of the output data were sent to Tokyo and monitored all the time.

4.4.1 Monitoring of temperature and humidity

Several thermometers and a hygrometer were set around the detector to know the surrounding environment of the detector and the data acquisition system. Four thermometers were attached in the van (near the rear door, near the front door, front and back side of VME crate), and one thermometer was attached out of the van (under the body). The hygrometer was set near the rear door in the van.

They were connected to the data logger, and temperature and humidity taken around PANDA64 were recorded every 10 seconds (Figure 4.5).
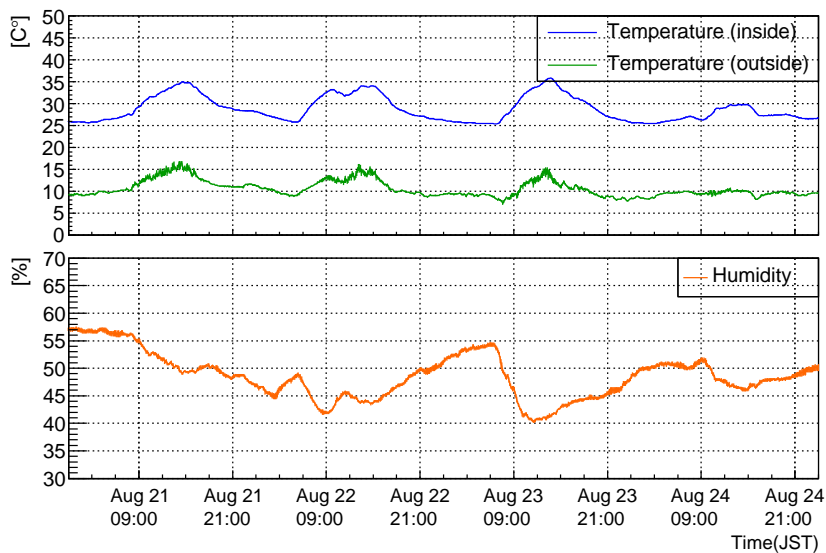
Figure 4.5: Monitoring of temperature and humidity around PANDA64

4.4.2 Monitoring of high voltage power supply

Output signals of a PMT fluctuates corresponding to slight variation of the supplied high voltage. The high voltage power supply (Matsusada Precision HARb-3*200) is equipped with output terminals to monitor its voltage and current. Temporal variation of the voltage and current were monitored every 10 seconds through the data logger (Figure 4.6).
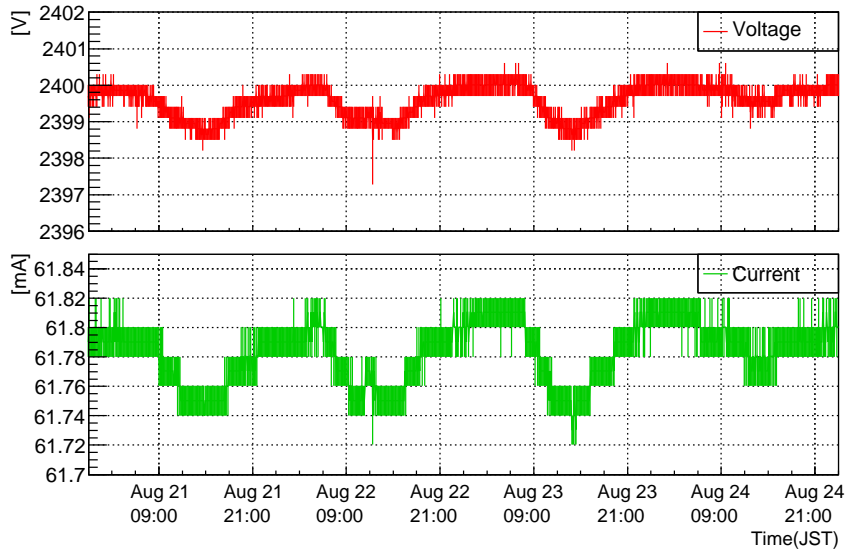
Figure 4.6: Monitoring of high voltage power supply

4.4.3 ADC output

Stability of the output from ADC was also monitored. In PANDA64's data acquisition system, the pedestal values of 128 PMTs are measured every time before taking each data file. The pedestal values (the peak position and the width) were monitored for each file which is usually created every 2 or 3 minutes. The output signals of ADCs were also monitored after pedestals were subtracted. An example of ADC monitoring is shown in Figure 4.7.
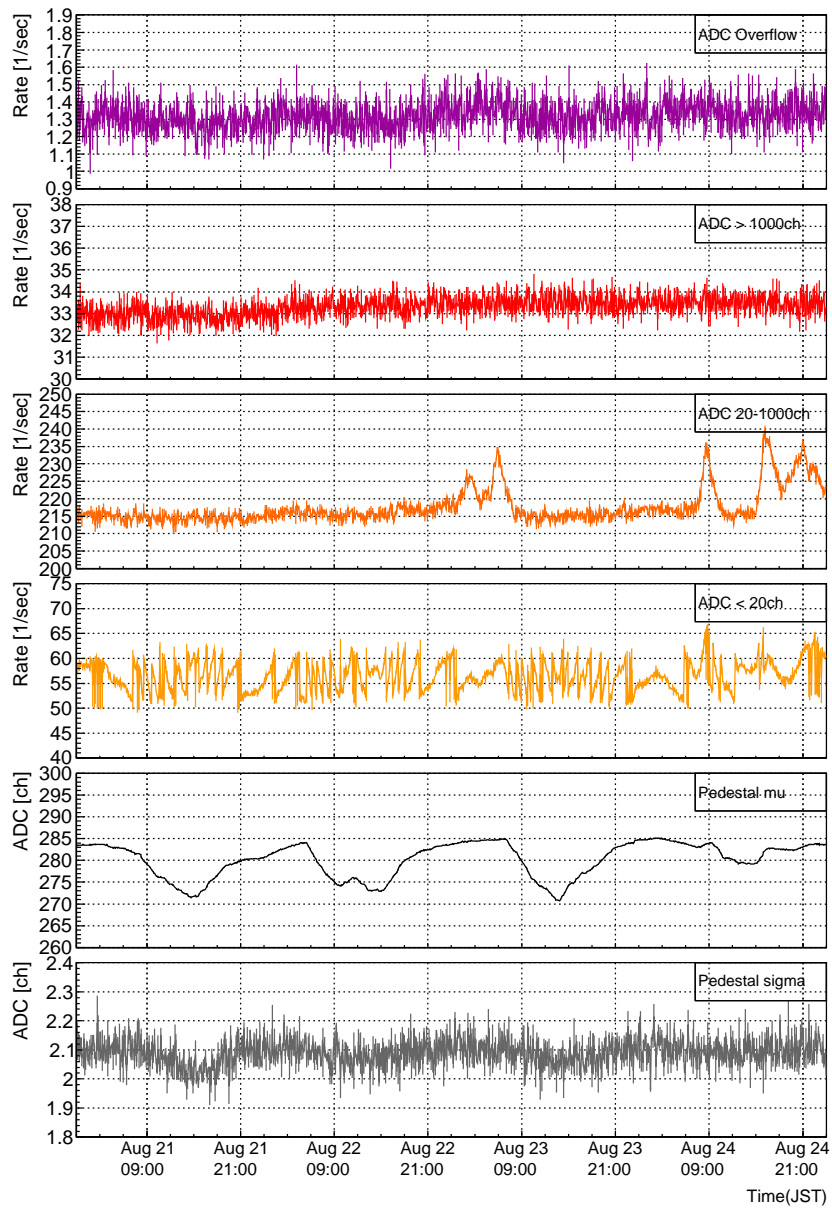
Figure 4.7: Monitoring of pedestal and output of ADC (PMT-01L)

Chapter 5

Preparation for data analysis

Before analyzing data taken at Norikura Observatory, calibration and gain correction were performed for each PMT and module. Furthermore, various threshold values of ADC zero suppression and discriminators were unified among all PMTs in order to apply common threshold values to each PMT. A common constant value was also determined for the high energy threshold which causes overflow of ADCs.

5.1   Calibration

5.1.1   Light propagation model

The scintillation light on plastic scintillator is considered to consist of two components based on a simple light propagation model. In this model, one of the components of the scintillation light repeats total reflection on the surface of the plastic scintillator and reaches a PMT without attenuation. The other component reflects on the aluminized mylar film and loses energy at every reflection. This light propagation model can be described as the equation 5.1 using two parameters, the ratio of attenuation component d and the attenuation length of scintillation light l [mm].

$$L_{\mathrm{PMT}} = L_{\mathrm{emitted}}((1 - d) + d \exp\left(-x/l\right)) \tag{5.1}$$

In this equation, L_{PMT} is the light intensity observed on a PMT, L_{emitted} is the original light intensity at the point of scintillation, and x [mm] is the

distance between the point of scintillation and the PMT.

In addition, two parameters a and b were assumed to describe the resolution σ of each PMT signal. The equation of evaluating σ is:

$$\sigma = \sqrt{a^2 L_{\mathrm{PMT}} + b^2} \qquad (5.2)$$

, where a $[\sqrt{\mathrm{keV}}]$ is the parameter corresponding to the statistical error of the number of photoelectrons, and b [keV] is the parameter corresponding to all other systematic errors such as the electric noise on the PMT.

A signal reaching PMT is converted to a digital signal by ADC. When converting ADC signal [ch] to energy [keV], the parameter $width$ [keV/ch] of each PMT is applied. Calibration was performed to determine these parameters using ^{60}Co source.

5.1.2 Calibration using ^{60}Co source

PANDA64 has slits of 1 cm width at three positions on every 2 layers of modules (Figure 3.1) so that ^{60}Co source can be set neighboring all 64 modules. The three positions of each layer are the center of the plastic scintillator (C) and 5 cm from the both ends of plastic scintillator (L and R). The fit range was adjusted for each three positions of the source (L/C/R) to include the position of the Compton edge of gamma-rays of 1.17 MeV and 1.33 MeV emitted by ^{60}Co. The calibration data were taken at the parking near Hongo Campus of the University of Tokyo on July 2nd before transportation to Norikura Observatory.

The procedure of the calibration was as follows. Firstly, the Gaussian function was fitted to the data taken by random timing gate signals by the least chi-square method and the b parameter of each ADC channel was estimated by the fit result. Then the simulated ADC values of each PMT for three different ^{60}Co source positions (L/C/R) were fitted to the measured calibration data in order to determine the parameters l and d of the module. Simultaneously, the parameter a, b and $width$ are fitted in the fitting process. An example of the calibration fitting results are shown in Figure 5.1.

module-1 : chi2/dof:0.924412

width$_l$eft:4.59278 ,a$_l$eft:3.02529 ,b$_l$eft:11.4291 : width$_r$ight:4.40957 ,a$_r$ight:3.06285 ,b$_r$ight:8.10224 : d:0.695578 l:589.274

heights(source:L):5.52887 ,heights(source:C):5.63373 ,heights(source:R):5.52083
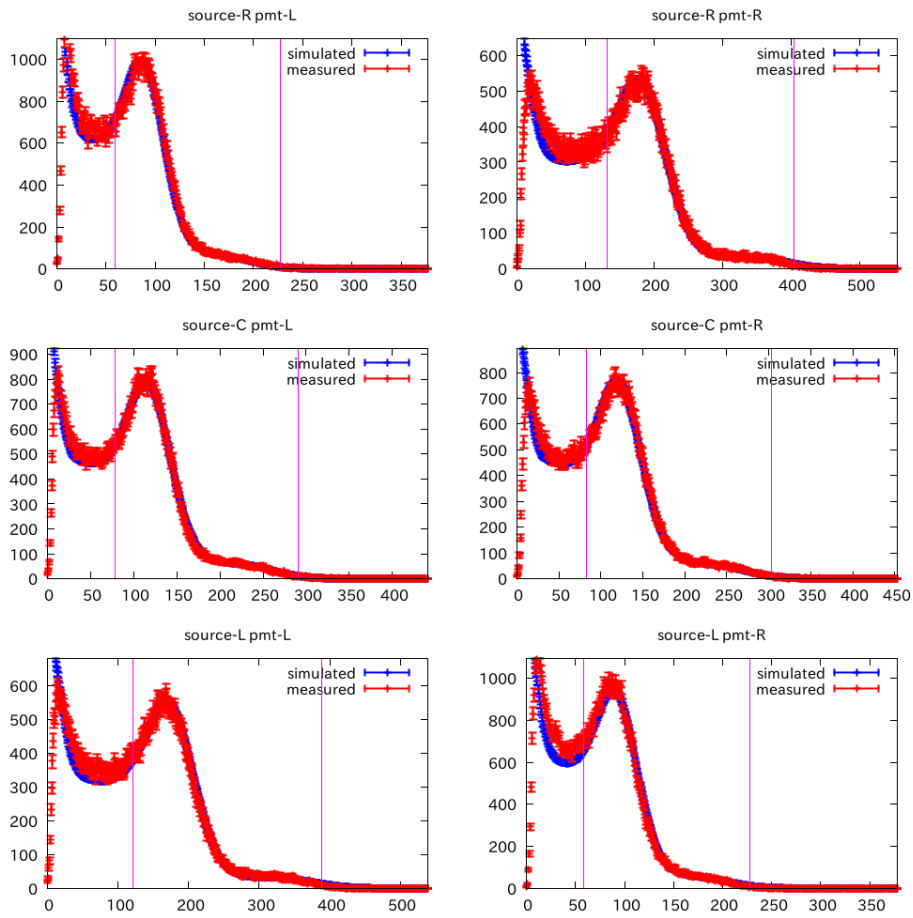
Figure 5.1: An example of calibration results (PMT-01L and PMT-01R)

5.2 Gain stability

The parameter *width* determined by calibration was not always constant, varying slightly in association with several factors (Figure 5.2). To correct the temporal variation of *width*, cosmic muons penetrating through the detector were utilized.

When the cosmic muon events penetrating through PANDA64 were collected, a bump appears on the spectrum at the high energy range of ADC output. The peak position of muon bumps are determined every hour by the least chi-square method and compared with the reference data. The reference was taken at the same time when the calibration data of ^{60}Co were taken near Hongo Campus to gain the relative values. The relative gain fit values were then applied to the parameter *width* when it was used for calculation of ADC output.
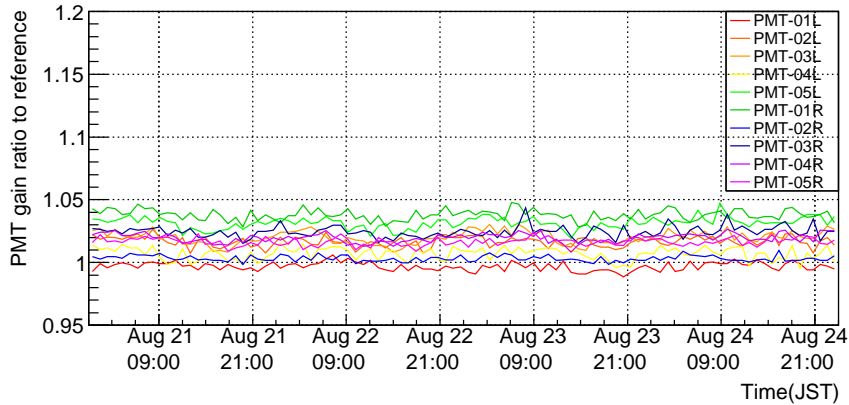
Figure 5.2: An example of relative gain values (PMT-01L - PMT-05R)

5.3 Software cuts

5.3.1 Cut-off energy of ADC zero suppression

As described in 3.2, zero suppression of ADC was applied to this measurement in order to reduce the size of the data transferred from the ADCs to the PC. The threshold of zero suppression was set to the value corresponding

to 3 σ from the peak of the pedestal. If ADC output is below this threshold, the energy deposit is regarded as zero.

The cut-off energy of a PMT suppressed to zero varies among 128 PMTs because it depends on the parameter *width* and the σ of the pedestal fitting. To set the common threshold value for all the PMTs, the highest cut-off energy was used as the standard value and the common threshold was fixed to 60 keV.

This value was used as the software cut of the analysis and used for both the measurement and the simulation data. If the left and/or right PMT signals (E_l, E_r) of a module are below 60 keV, the energy deposit of the module is calculated as zero.

5.3.2 Threshold of discriminators

Eight 16ch discriminators (CAEN V895) are used for the data acquisition of PANDA64. The discriminators send trigger signals if the input signal exceeds a threshold voltage. The threshold value can be changed by users and was set to 150 mV for the mountaintop experiment at Norikura Observatory as described in 4.2.

The energy corresponding to the discriminator threshold of 150 mV differs among each PMT. Therefore the common threshold 400keV was used for the software cut selection. The value 400 keV was determined based on the highest cut-off energy among 128 PMTs and corresponds to the energy deposit of approximately 900 keV on the far end of the module. When both E_l and E_r of a module exceed this threshold energy, the trigger signal is turned on and a gate signal is sent to ADC for data acquisition.

5.3.3 Overflow value of ADC

Finally the software cut for overflow energy of ADCs was determined. The ADCs (CAEN V792) record the output signals of PMTs as channels of 0 to 4095, and the lowest energy which cause an overflow (> 4095 [ch]) of ADC differs depending mainly on the parameter *width*. Therefore, the common overflow energy was set to 12 MeV for all PMTs. This energy corresponds to the energy of 20MeV incident around the center of the module. If E_l

and/or E_r of a module are higher than 12 MeV, it is regarded as an overflow module even if they are not actually overflow. The events which include one or more overflow modules are usually ignored in following analysis because the correct energy cannot be calculated.

All software cuts described above are shown in Table 5.1.

Table 5.1: Software cuts applied to the data

Cut name	Software cut	Response of the cut
ADC zero suppression	E_l or $E_r < 60$ keV	Calculated as $E = 0$
Discriminator threshold	E_l and $E_r \geq 400$ keV	Trigger signal ON
ADC overflow	E_l or $E_r > 12$ MeV	Overflow signal ON

Chapter 6

Detection of radiation bursts

6.1 Search for burst candidates

All data taken at Norikura Observatory during measurement period were converted to event files for analysis after the software cuts shown in Table 5.1 were applied. Each event data consisted of energy, position of energy deposits on each module and time of the event. The total energy deposit of all modules was hereafter called E_{tot}, as well as the energy deposit by the most energetic module was called E_{1st} and the second was called E_{2nd}. Events which included one or more overflow modules were excluded from the analysis because accurate E_{tot} could not be calculated.

6.1.1 Count rate enhancements

In order to search for signal enhancements related to thunderclouds, all data taken during measurement period were divided into 30-second time blocks at first, and the time blocks whose count rate exceeded a reference level significantly by more than 5 σ were collected. The energy range of the count rate was set to 3 - 100 MeV in order to reject the effect of rain fallout of radon and its daughter ions (^{218}Po, ^{214}Pb and ^{214}Bi) which emit gamma-rays of < 2.5 MeV [67]. The lower threshold of 3 MeV also improved S/N ratio by rejecting environmental gamma-rays up to 2.6 MeV emitted from ^{208}Tl.

The reference count rate was defined as the mean count rate of 120 minutes, 20 - 80 minutes prior and posterior to each 30-second block. Then

the signal enhancements of 5 σ significance continuing for more than one minute, which was equivalent to two or more consecutive 30-second blocks, were collected as radiation burst candidates.

Under this condition, 12 significant signal enhancements were found (Table 6.1). Each burst was named such as "burst20140708-1". Figure 6.1 - 6.4 show the count rate of some 30-second time blocks exceeded 5 σ range in each burst period. In order to pick up shorter radiation bursts which lasted for less than one minute, signal enhancements which had three or more consecutive 10-second time blocks of more than 3 σ significance were also searched, but no candidate was found under this condition except for the burst candidates found above.

The burst period of each candidate was defined based on 30-second time blocks exceeding the reference count rate significantly by 3 σ. At first, consecutive 30-second time blocks exceeding 3 σ significance around the peak of the count rate enhancement were preset as a burst period. If other consecutive time blocks exceeding 3 σ significance came within 5 minutes before or after the predefined burst period, they were also regarded as the same burst period. In case that multiple peaks of 5 σ came within a short time interval which could not be divided easily, e.g. burst20140823-1, a burst period which included all the containing peaks was applied to the burst.

The background period of each burst was defined as half an hour between 5 - 35 minutes either prior or posterior to the burst period, which was chosen based on stability of the baseline. The background periods are also shown in Figure 6.1 - 6.4.

Some bursts had relatively symmetric peaks, while other bursts were asymmetric. The difference of burst shapes might be attributed to the distribution of electric charges inside thunderclouds or stability of the acceleration region, although the actual factor could not be identified by this experiment.

6.1.2 Temporal variation of multiple energy ranges

Temporal variation of the count rate of 12 burst candidates are plotted in Figure 6.5 - 6.16. Each figure consists of several energy ranges of 3 -

46
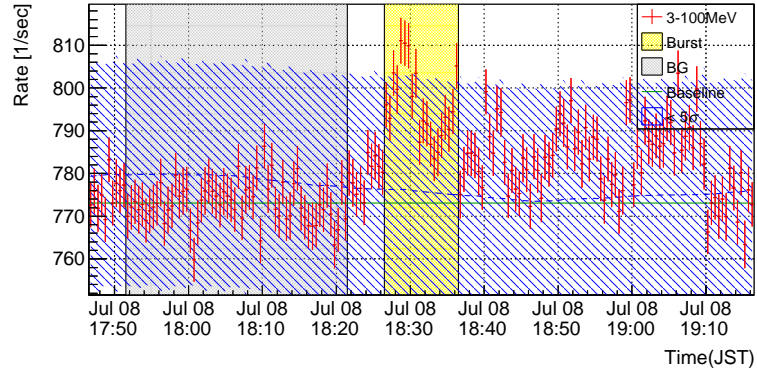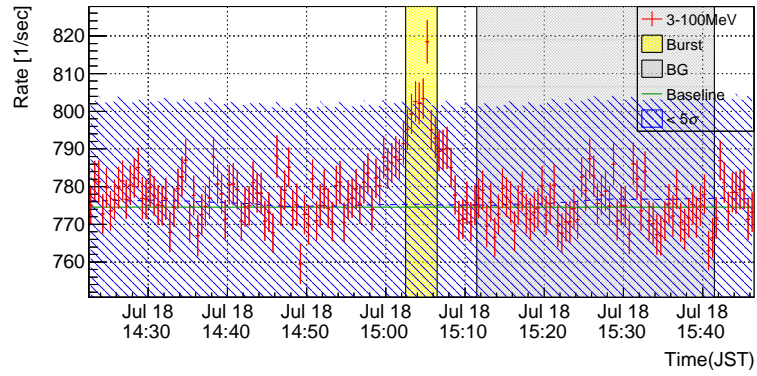
(a) burst20140708-1
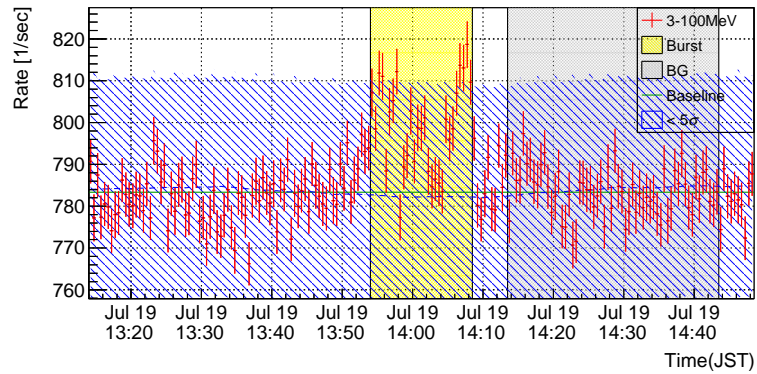
(b) burst20140718-1

(c) burst20140719-1

Figure 6.1: Definition of burst20140708-1, burst20140718-1 and burst20140719-1; 30-second temporal variation of count rate of 3 - 100 MeV (red markers with 1 σ statistical error bars); burst (yellow) and background (gray) periods; 5 σ range against reference count rate (blue shadow zone); mean count rate of background period (green solid line)

47
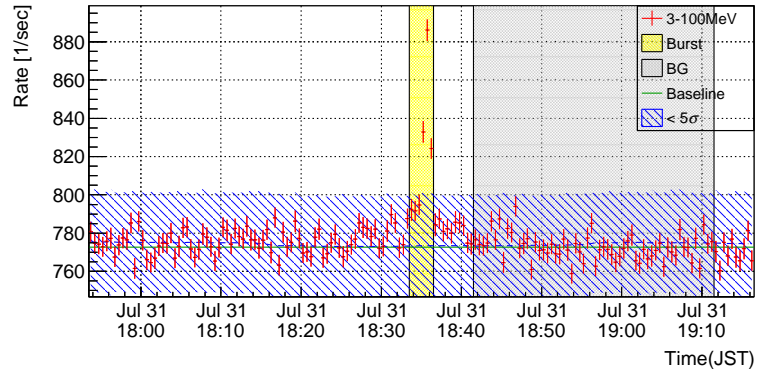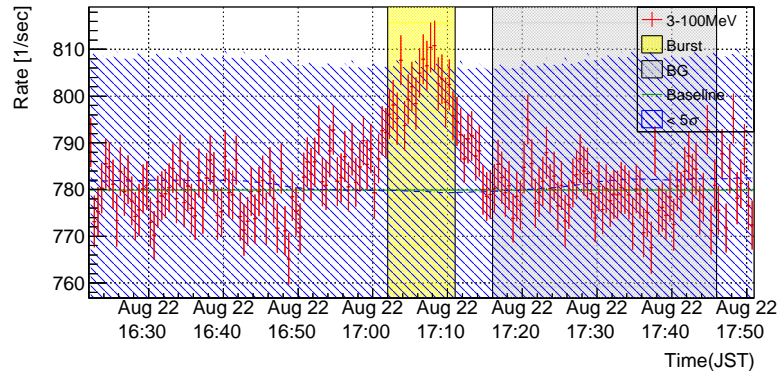
(a) burst20140731-1
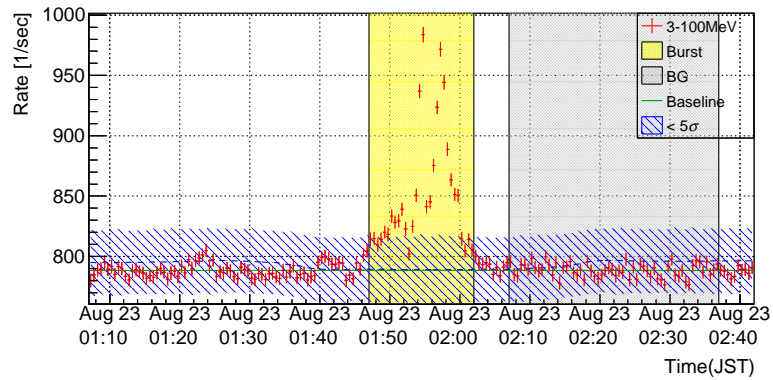
(b) burst20140822-1

(c) burst20140823-1

Figure 6.2: Same as Figure 6.1 but for burst20140731-1, burst20140822-1 and burst20140823-1

48
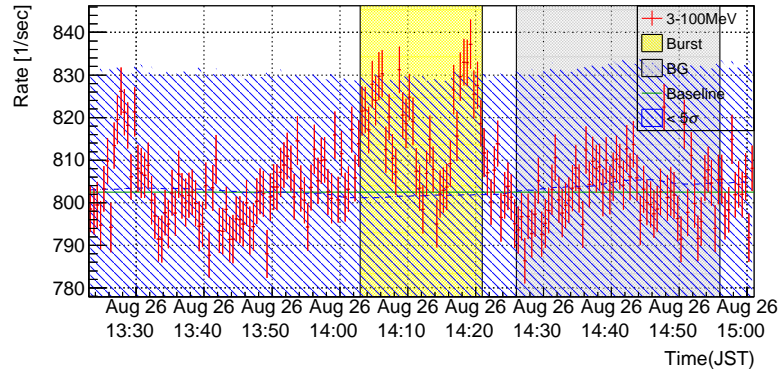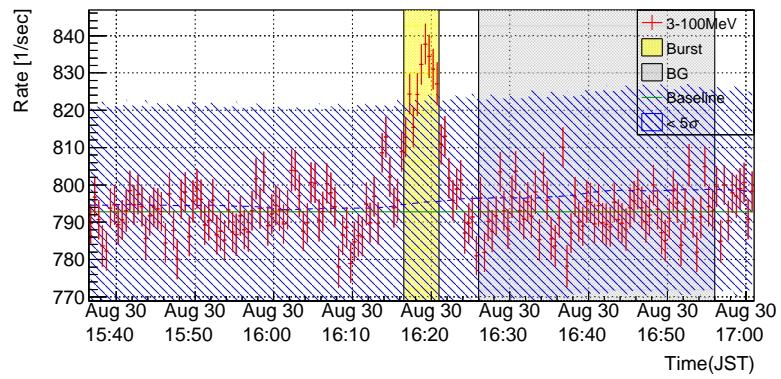
(a) burst20140826-1
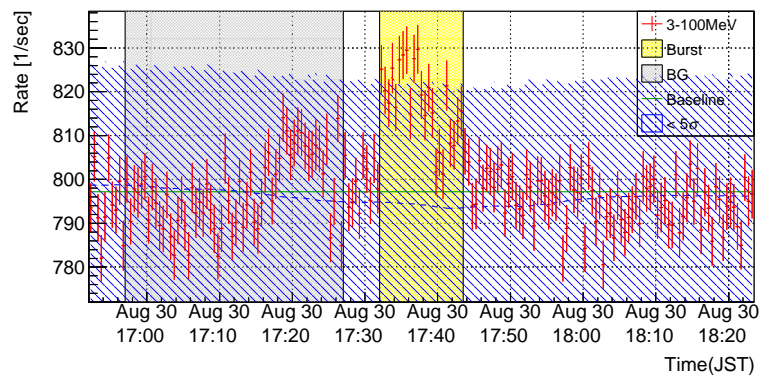
(b) burst20140830-1

(c) burst20140830-2

Figure 6.3: Same as Figure 6.1 but for burst20140826-1, burst20140830-1 and burst20140830-2
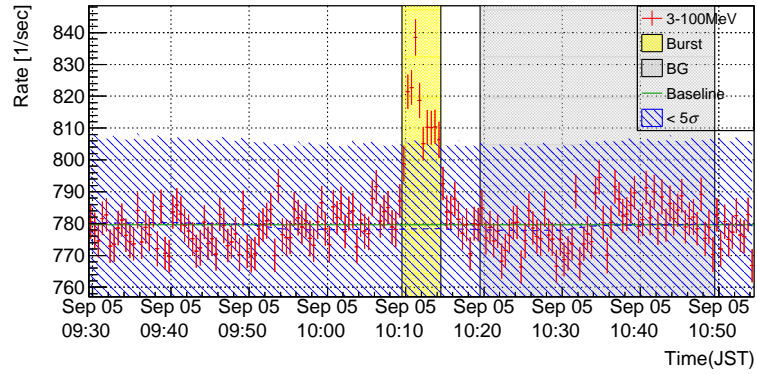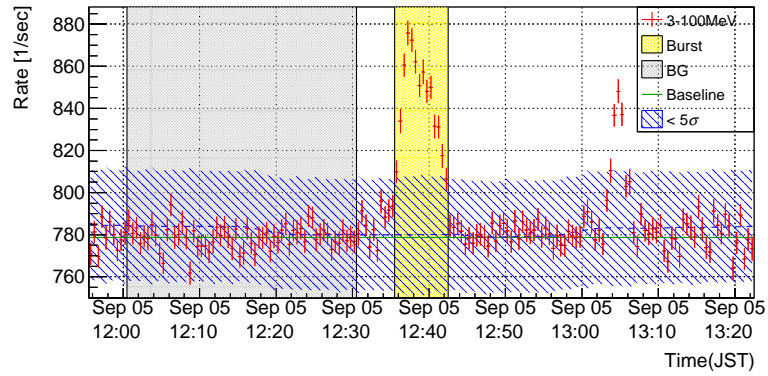
(a) burst20140905-1
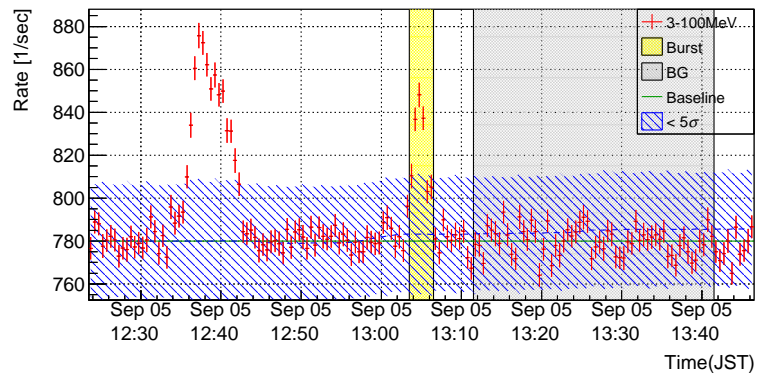
(b) burst20140905-2

(c) burst20140905-3

Figure 6.4: Same as Figure 6.1 but for burst20140905-1, burst20140905-2 and burst20140905-3

50

Table 6.1: Candidates of radiation bursts and the duration of signal enhancements

Name	Date	Burst start	Burst end	Duration
burst20140708-1	2014-07-08	18:26:30 JST	18:36:30 JST	10.0 min
burst20140718-1	2014-07-18	15:02:30 JST	15:06:30 JST	4.0 min
burst20140719-1	2014-07-19	13:54:00 JST	14:08:30 JST	14.5 min
burst20140731-1	2014-07-31	18:33:30 JST	18:36:30 JST	3.0 min
burst20140822-1	2014-08-22	17:02:00 JST	17:11:00 JST	9.0 min
burst20140823-1	2014-08-23	01:47:00 JST	02:02:00 JST	15.0 min
burst20140826-1	2014-08-26	14:03:00 JST	14:21:00 JST	18.0 min
burst20140830-1	2014-08-30	16:16:30 JST	16:21:00 JST	4.5 min
burst20140830-2	2014-08-30	17:32:00 JST	17:43:30 JST	11.5 min
burst20140905-1	2014-09-05	10:09:30 JST	10:14:30 JST	5.0 min
burst20140905-2	2014-09-05	12:35:30 JST	12:42:30 JST	7.0 min
burst20140905-3	2014-09-05	13:03:30 JST	13:06:30 JST	3.0 min

100 MeV, 3 - 5 MeV, 5 - 10 MeV, 10 - 20 MeV, 20 - 40 MeV, 40 - 100 MeV, as well as the total count rate of all energy ranges below 100 MeV (0 - 100 MeV). The 0 - 100 MeV count rate of 12 burst candidates showed typical gradual increase (or sometimes decrease) caused by rain fallout of radon and its daughter nuclei.

On the other hand, the count rates of above 3 MeV range (3 - 100 MeV) showed different kind of short term enhancements which lasted for a few to ten minutes. Since the baseline of this range did not show clear temporal variation coinciding with the 0 - 100 MeV range, enhancements of the 3 - 100 MeV range did not seem to be caused by rain fallout. In addition, some burst candidates such as burst20140823-1 showed clear enhancements in the 10 - 20 MeV or higher energy ranges. Such enhancements in high energy ranges strongly suggest that they were radiation bursts related to thundercloud activities as observed by several previous experiments at the top of mountains or in coastal areas of the Sea of Japan.

The mean count rate enhancement and the maximal enhancement of 30-second count rate during burst periods (background subtracted) are shown in Table 6.2 along with the total count and its statistical significance. The most statistically significant burst was burst20140823-1, the second was

burst20140905-2 and the third was burst20140731-1.

Table 6.2: Peak and mean 3 - 100 MeV count rate, total count and statistical significance of the total count (background subtracted) of 12 burst candidates

Burst name	Peak rate [/sec]	Mean rate [/sec]	Total count ($\times 10^3$)	Significance [σ]
burst20140708-1	38.0 ± 5.4	23.1 ± 1.4	12.95 ± 0.77	16.8
burst20140718-1	43.9 ± 5.8	26.3 ± 2.0	5.79 ± 0.45	13.0
burst20140719-1	35.3 ± 5.6	15.8 ± 1.2	12.42 ± 0.96	12.9
burst20140731-1	113.4 ± 5.6	48.0 ± 2.3	7.94 ± 0.39	20.6
burst20140822-1	31.0 ± 5.4	22.1 ± 1.4	11.10 ± 0.72	15.4
burst20140823-1	195.3 ± 6.3	62.2 ± 1.2	51.65 ± 1.02	50.8
burst20140826-1	34.8 ± 5.8	15.2 ± 1.2	14.54 ± 1.12	13.0
burst20140830-1	45.0 ± 5.5	33.7 ± 2.0	8.22 ± 0.48	17.1
burst20140830-2	32.5 ± 5.6	20.6 ± 1.4	12.65 ± 0.83	15.2
burst20140905-1	58.9 ± 5.6	34.7 ± 1.9	9.49 ± 0.51	18.7
burst20140905-2	97.0 ± 5.9	64.8 ± 1.6	24.70 ± 0.62	39.6
burst20140905-3	68.2 ± 5.7	43.9 ± 2.4	7.02 ± 0.38	18.5

6.2 Correlation with thunder information

To investigate the correlation between observed radiation bursts and thunderclouds, thunder information were utilized.

6.2.1 Thunder Nowcast (Japan Meteorological Agency)

Thunder Nowcast is an online service provided by Japan Meteorological Agency [1]. It updates information of thunder activities in and around Japan every 10 minutes on its website. The data of Thunder Nowcast are provided based on analysis of lightning detection by their thunder monitoring systems and cloud observation by their meteorological radars. Levels corresponding to the intensity of thunder activities and the possibility of lightning strikes are shown in each grid of 1 km on the map.

The levels of thunder activities used in Thunder Nowcast are shown in Table 6.3. Level 1 corresponds to the status that there is a possibility of a lightning strike although it is not currently occurring. In Level 2, a lightning
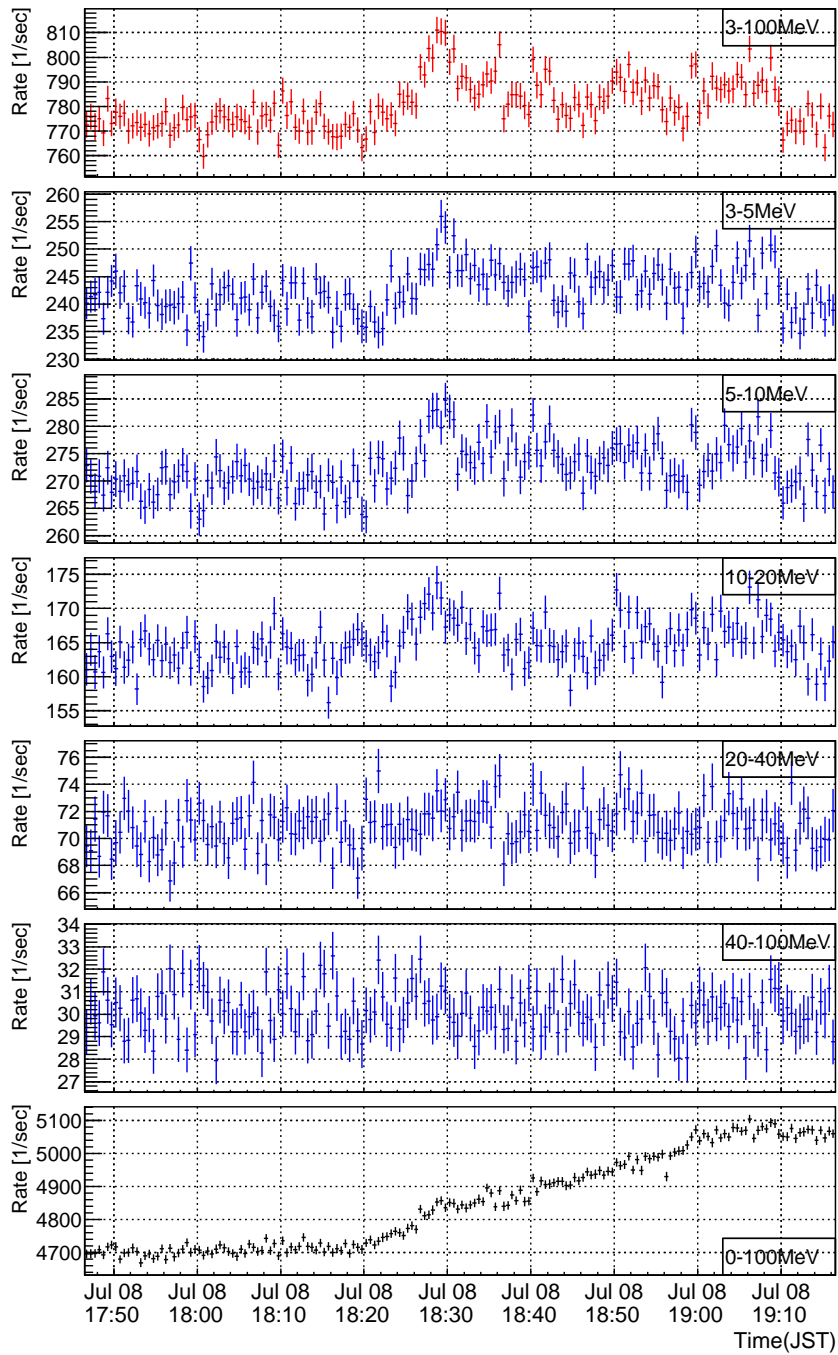
Figure 6.5: 30-second temporal variation of count rates in multiple energy ranges (burst20140708-1)
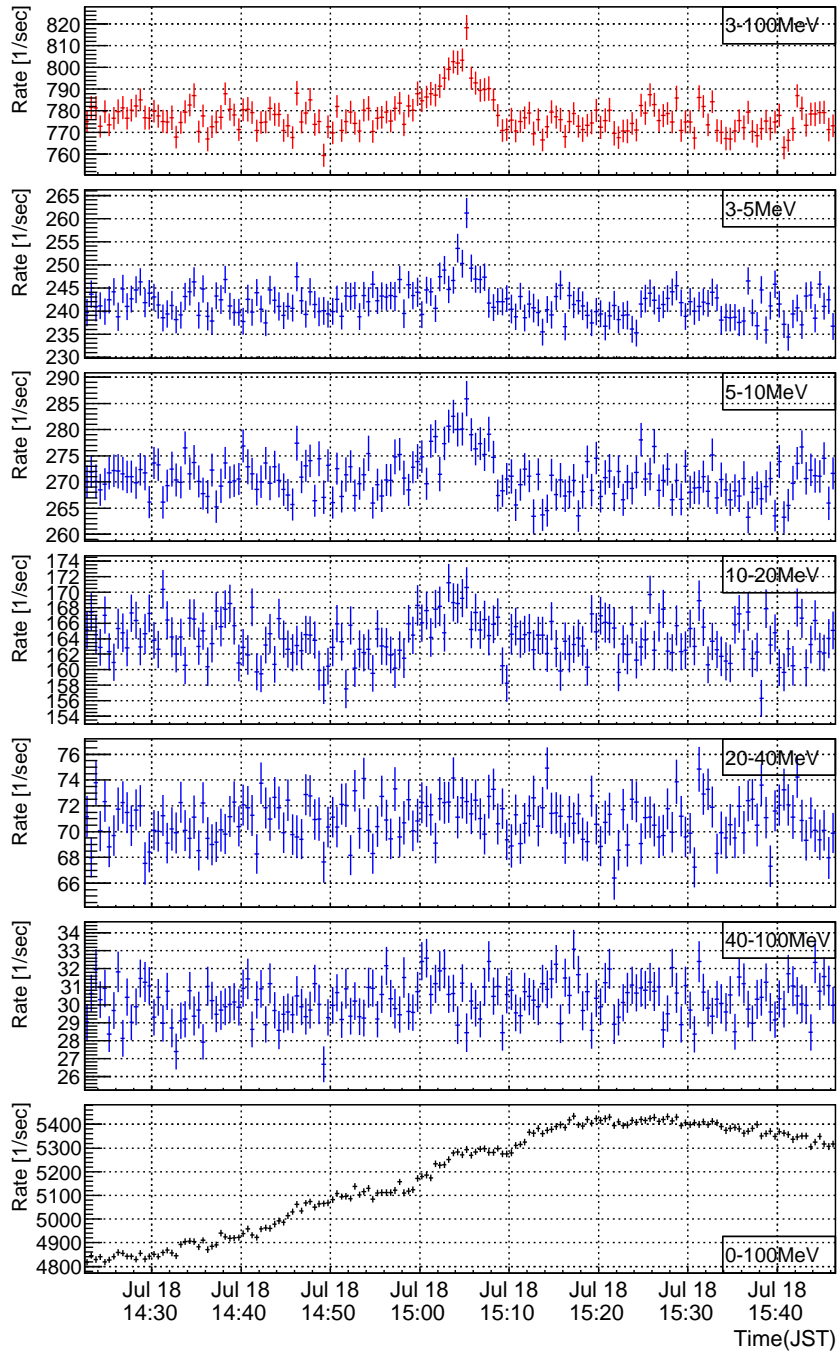
Figure 6.6: Same as Figure 6.5 but for burst20140718-1

54
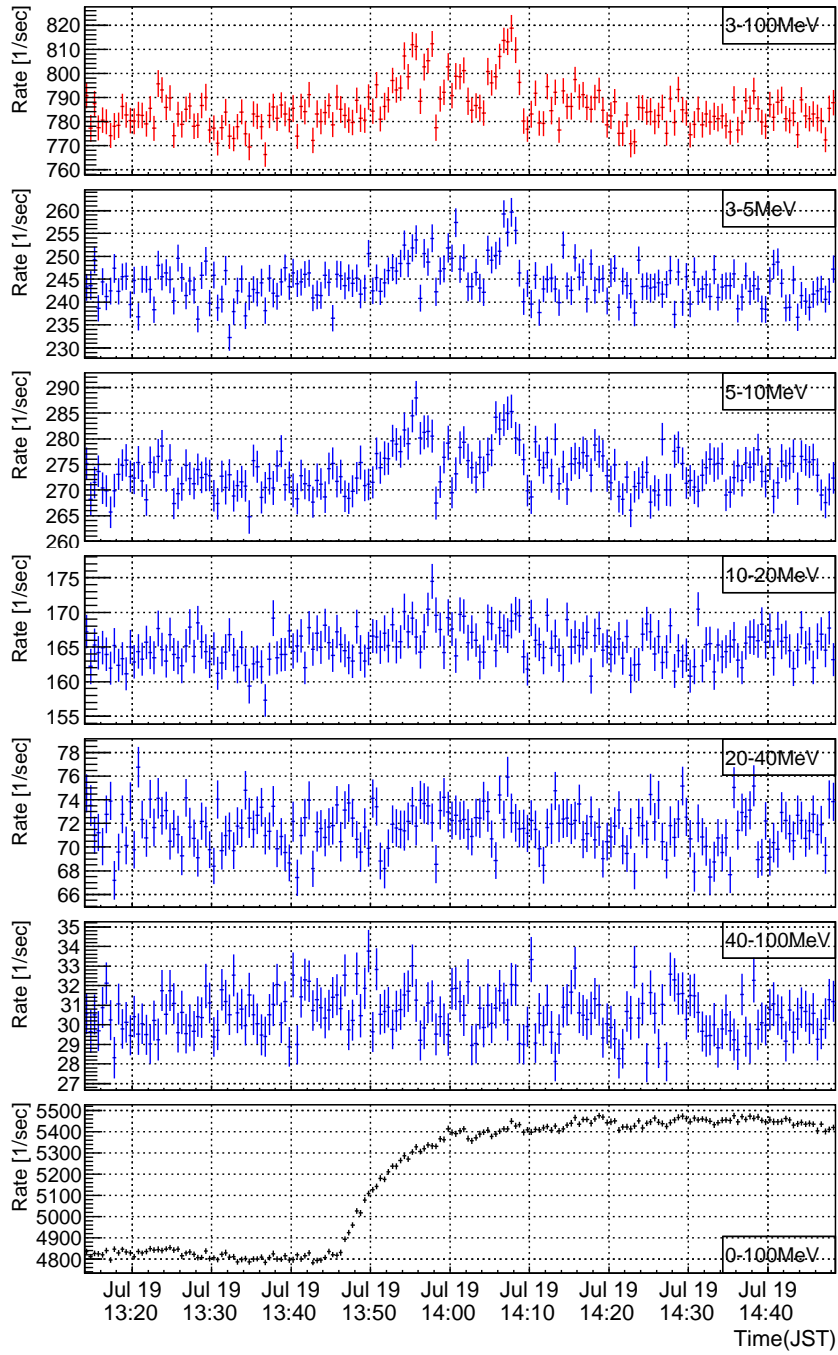
Figure 6.7: Same as Figure 6.5 but for burst20140719-1

55
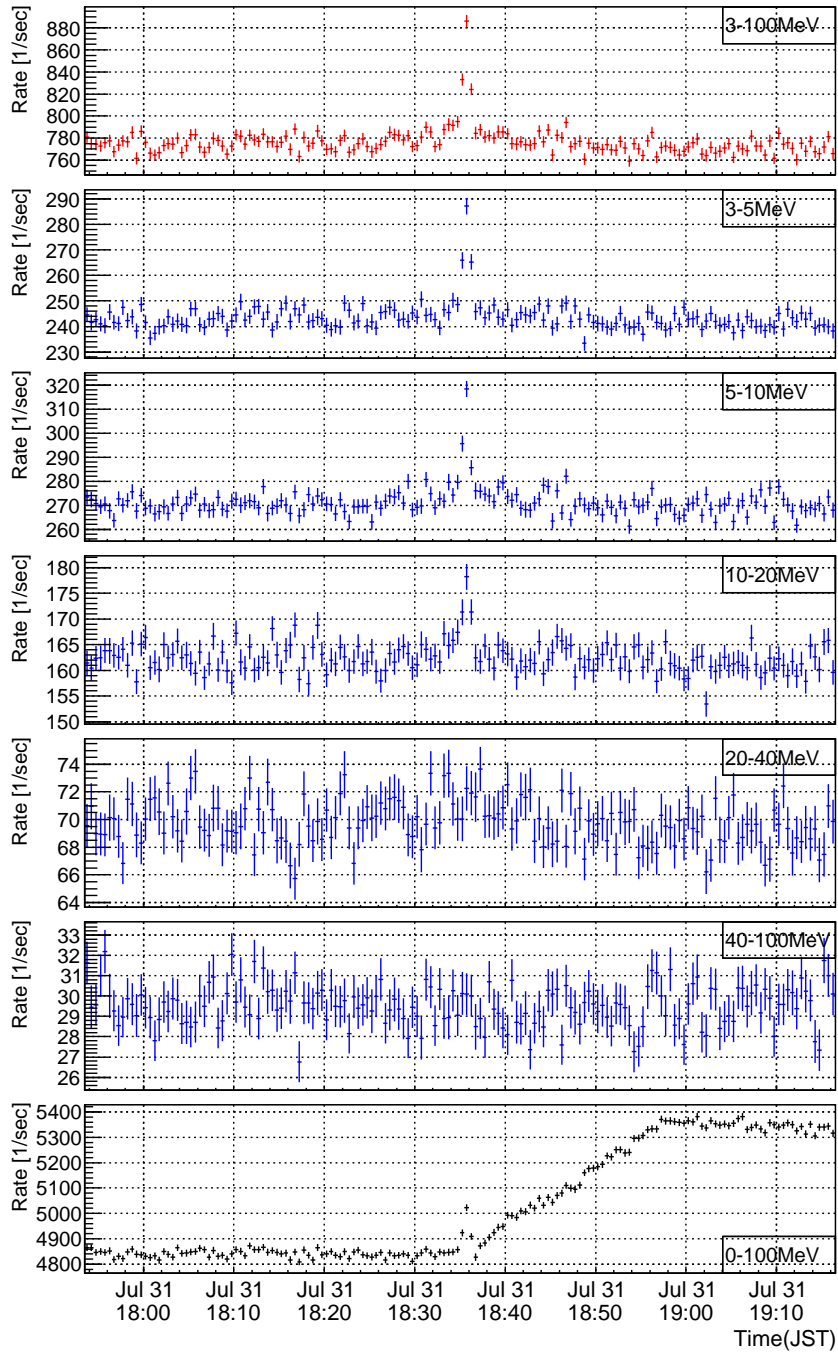
Figure 6.8: Same as Figure 6.5 but for burst20140731-1
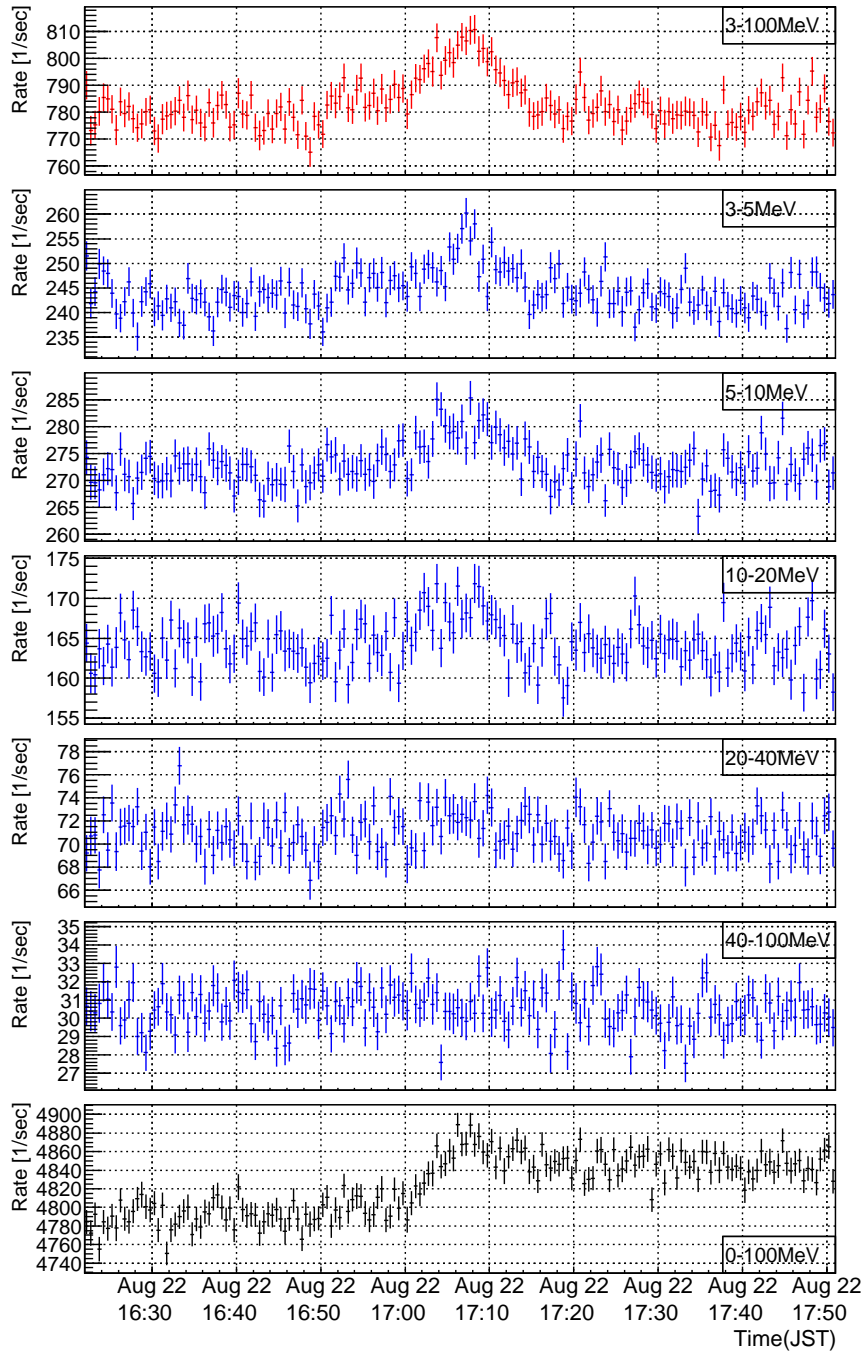
Figure 6.9: Same as Figure 6.5 but for burst20140822-1
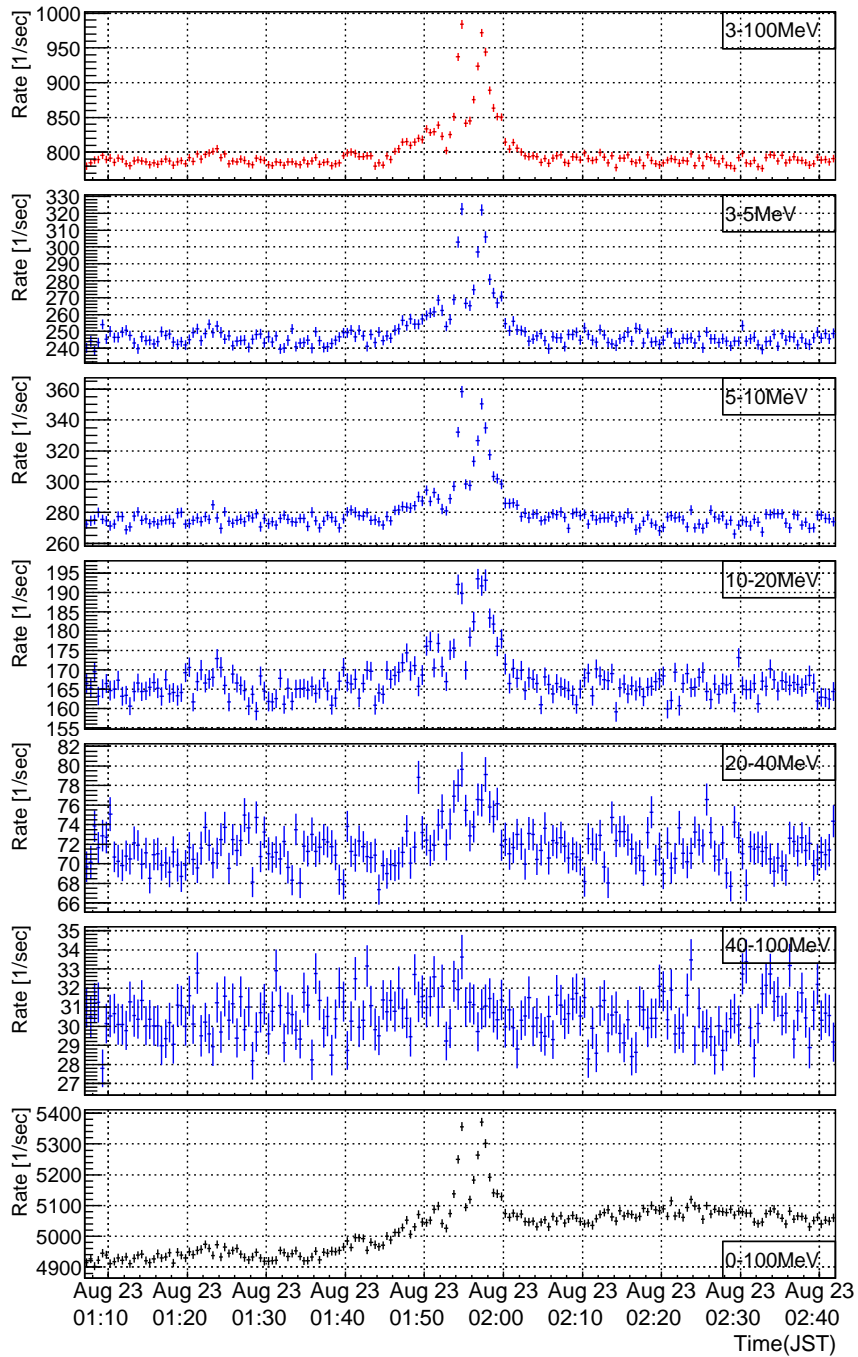
Figure 6.10: Same as Figure 6.5 but for burst20140823-1
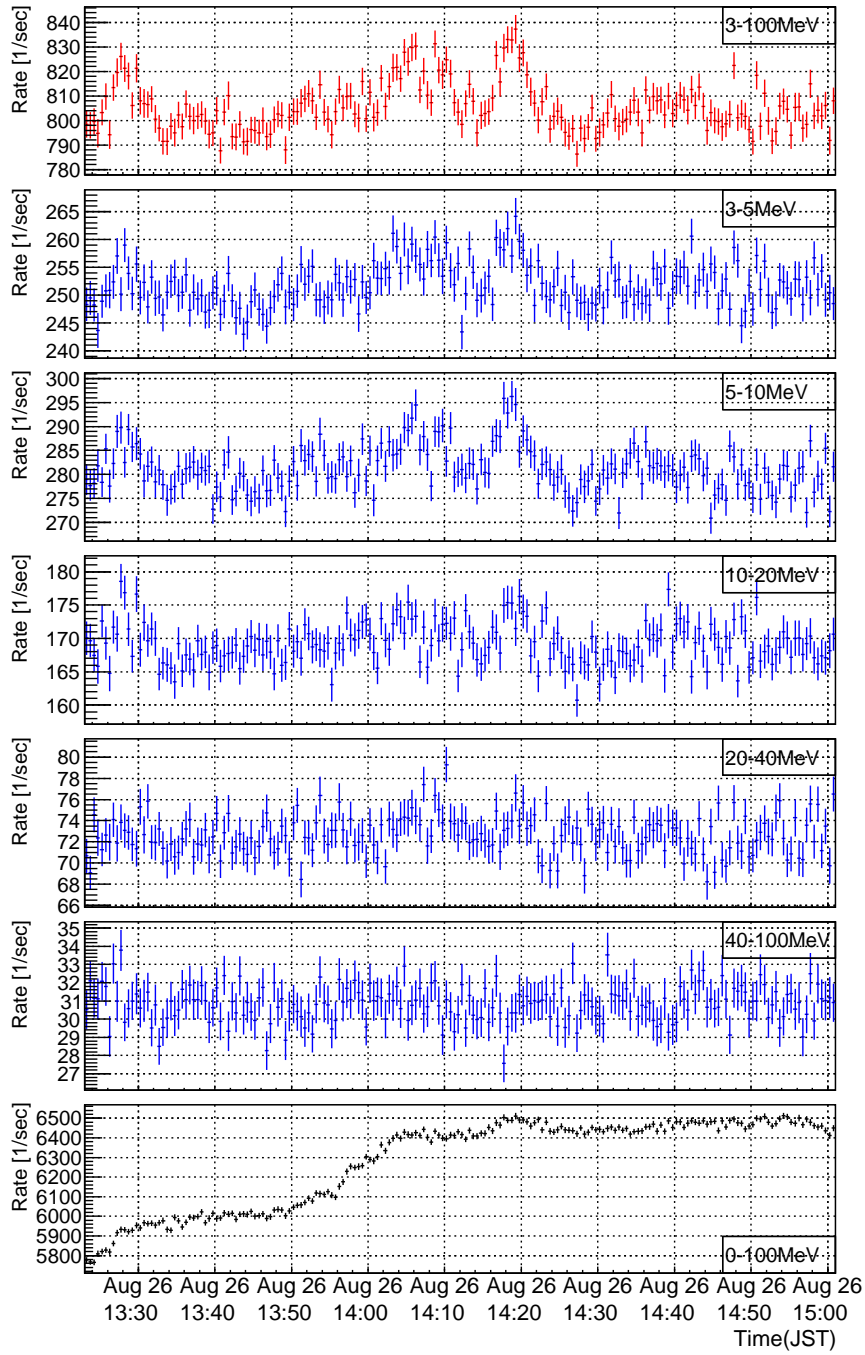
Figure 6.11: Same as Figure 6.5 but for burst20140826-1

59
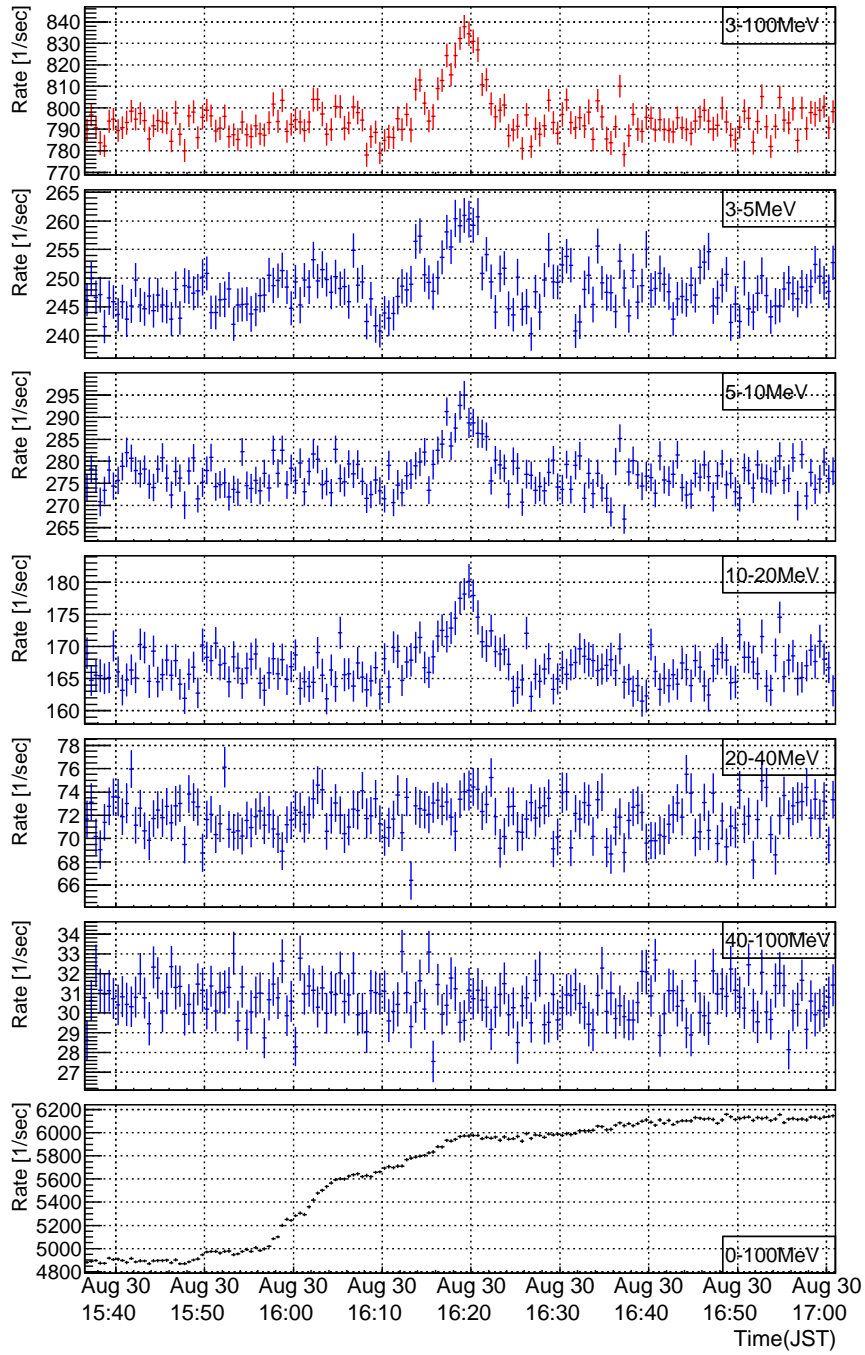
Figure 6.12: Same as Figure 6.5 but for burst20140830-1
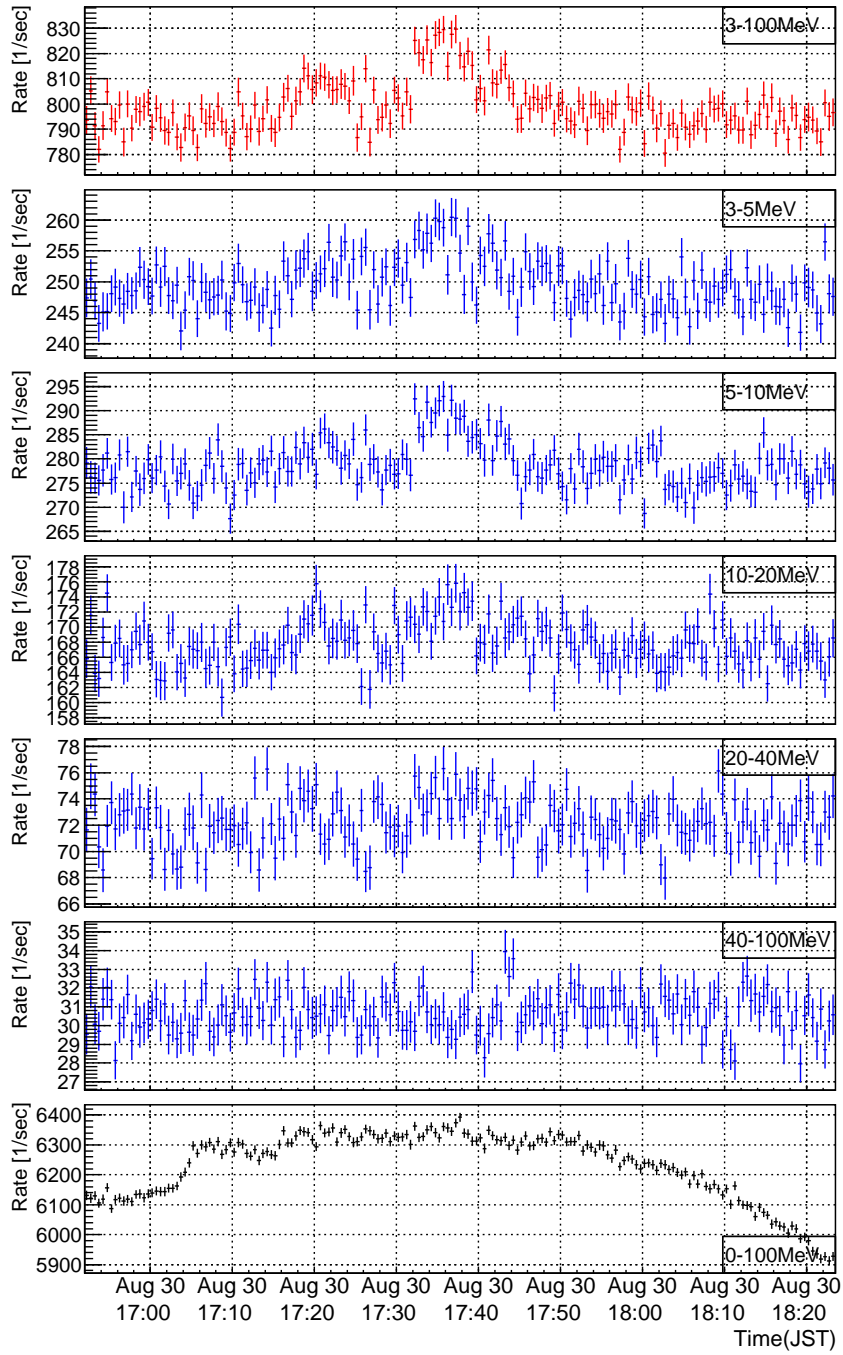
Figure 6.13: Same as Figure 6.5 but for burst20140830-2
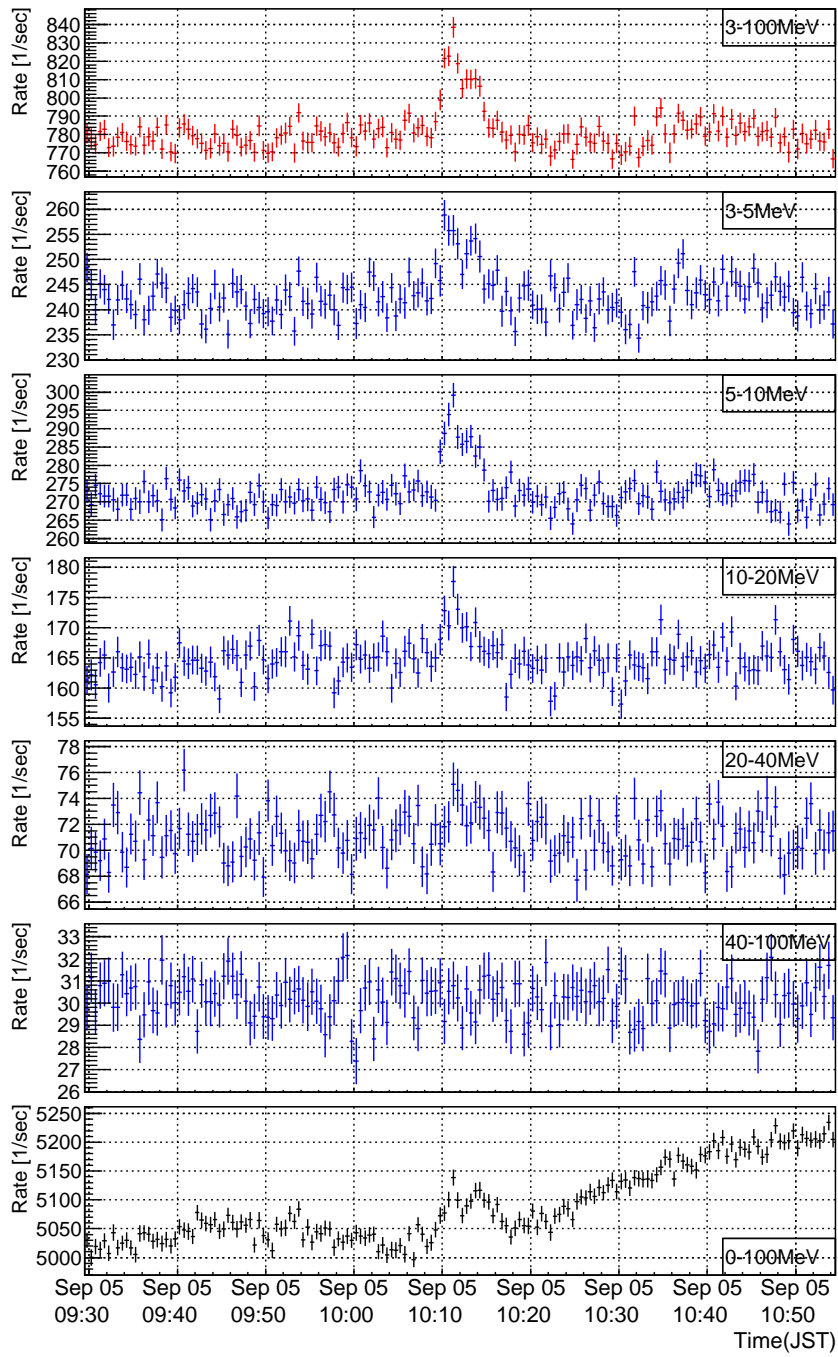
Figure 6.14: Same as Figure 6.5 but for burst20140905-1
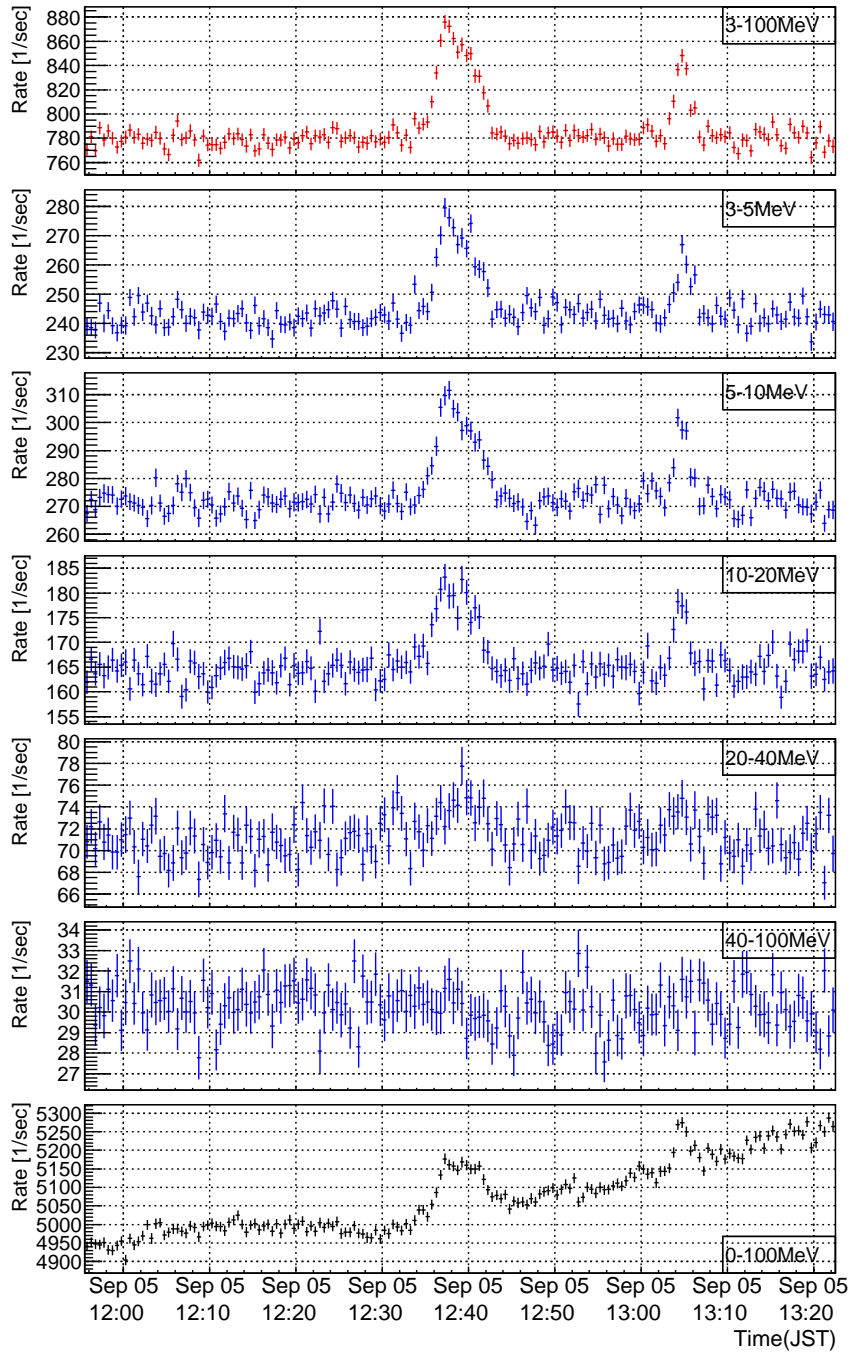
Figure 6.15: Same as Figure 6.5 but for burst20140905-2
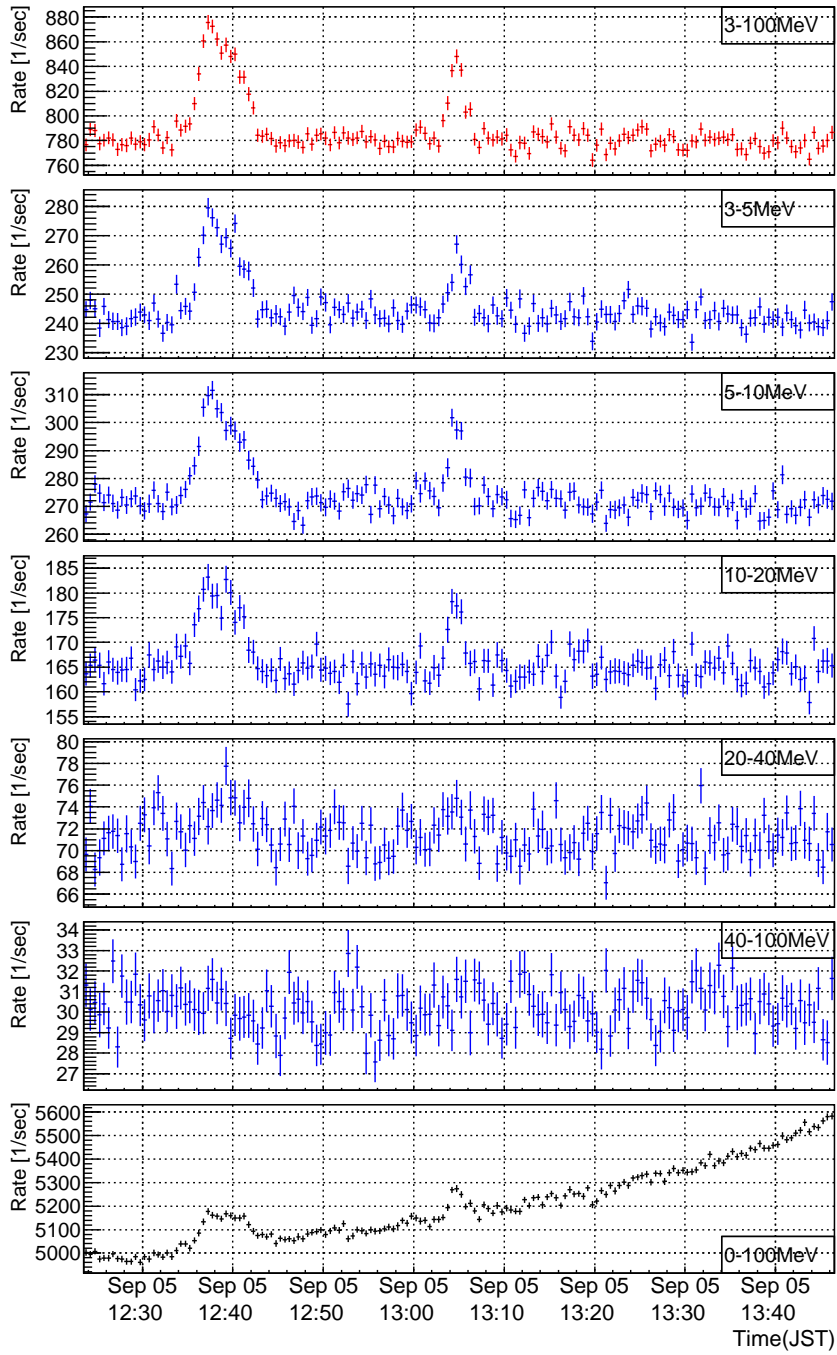
Figure 6.16: Same as Figure 6.5 but for burst20140905-3

64

is being seen or heard and/or there is a high possibility of a lightning strike. Level 3 and 4 mean that there is a lightning strike. Level 2 - 4 are decided by the thunder monitoring systems, while Level 1 and 2 are decided by the meteorological radars. Level 0 was defined by us in order to represent the status that no thunder activity level was shown, which would mean that thundercloud activity is not being observed.

The highest level of Thunder Nowcast in 5 km × 5 km grids surrounding Norikura Observatory (36'06 N, 137'33 E) recorded in less than 20 minutes from each burst period is shown in Table 6.4. Figure 6.17 - 6.18 are the images of Thunder Nowcast corresponding to 12 bursts. These images were obtained from Thunder Nowcast [1] and edited properly.

We defined a continuous period in which one or more grids in 5 km × 5 km around Norikura Observatory showed levels of ≥ Level X (X=1,2,3,4) as a "thunderstorm (≥ Level X)". Under this definition, "thunderstorms (≥ Level 1)" were recorded 121 times in 54 days of the measurement period at Norikura Observatory. The total number of Thunder Nowcast data which recorded Level 1 or higher around Norikura Observatory every 10 minutes was 859. Thus, the mean duration of "thunderstorms (≥ Level 1)" was 71 minutes. All 12 bursts were observed during these "thunderstorms (≥ Level 1)", which strongly suggested that they were radiation bursts related to thunderclouds.

On the other hand, "thunderstorms (≥ Level 2)" were recorded only 8 times in 54 days. The total number of Thunder Nowcast data which recorded Level 2 or higher was 28 during the measurement period and the mean duration of "thunderstorms (≥ Level 2)" was 35 minutes. Interestingly, 8 of 12 bursts were observed within 20 minutes from these "thunderstorm (≥ Level 2)" periods. Thus, all of 8 "thunderstorms (≥ Level 2)" might be correlated to radiation bursts.

6.2.2 Thunder Information (Chubu Electric Power Co., Inc.)

In addition to Thunder Nowcast, "Thunder Information" provided by Chubu Electric Power Co., Inc. was also investigated for reference [3]. It provides

Table 6.3: Thunder activity levels of Thunder Nowcast [1]

Level	Color	Status
(0)	Gray	(Thundercloud activity is not being observed.)
1	Yellow	There is a possibility of a lightning strike although it is not currently occurring.
2	Orange	A lightning is being seen or heard. There is a high possibility of a lightning strike.
3	Red	There is a lightning strike.
4	Purple	A large number of lightning strikes are occurring.

Table 6.4: Highest levels of Thunder Nowcast by Japan Meteorological Agency recorded in 5 km × 5 km grids within 20 minutes from burst periods and highest levels of Thunder Information by Chubu Electric Power Co., Inc. recorded in 15 km × 15 km grids within 10 minutes from burst periods

Burst	Thunder Nowcast	Thunder Information
burst20140708-1	Level 3	Level 3
burst20140718-1	Level 1	Level 0
burst20140719-1	Level 2	Level 2
burst20140731-1	Level 3	Level 3
burst20140822-1	Level 1	Level 0
burst20140823-1	Level 2	Level 2
burst20140826-1	Level 2	Level 0
burst20140830-1	Level 3	Level 2
burst20140830-2	Level 1	Level 0
burst20140905-1	Level 1	Level 0
burst20140905-2	Level 2	Level 1
burst20140905-3	Level 2	Level 2

(a) 2014/07/08 18:40 JST

(b) 2014/07/18 15:10 JST

(c) 2014/07/19 13:50 JST

(d) 2014/07/31 18:40 JST

(e) 2014/08/22 17:00 JST

(f) 2014/08/23 02:00 JST
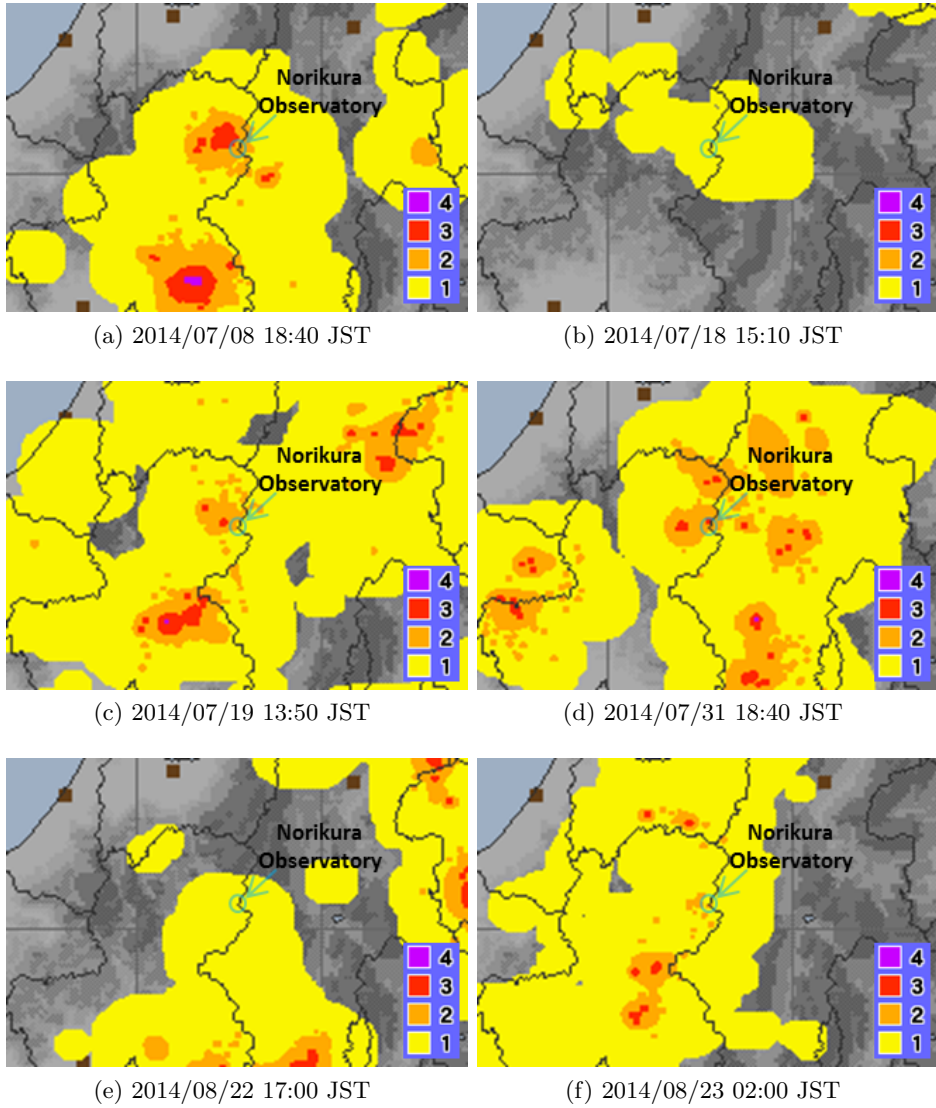
Figure 6.17:   Images of Thunder Nowcast recorded around 6 bursts (burst20140708-1 to burst20140823-1); These figures were obtained from [1] and edited properly.

(a) 2014/08/26 14:10 JST

(b) 2014/08/30 16:30 JST

(c) 2014/08/30 17:40 JST

(d) 2014/09/05 10:10 JST

(e) 2014/09/05 12:40 JST

(f) 2014/09/05 13:00 JST
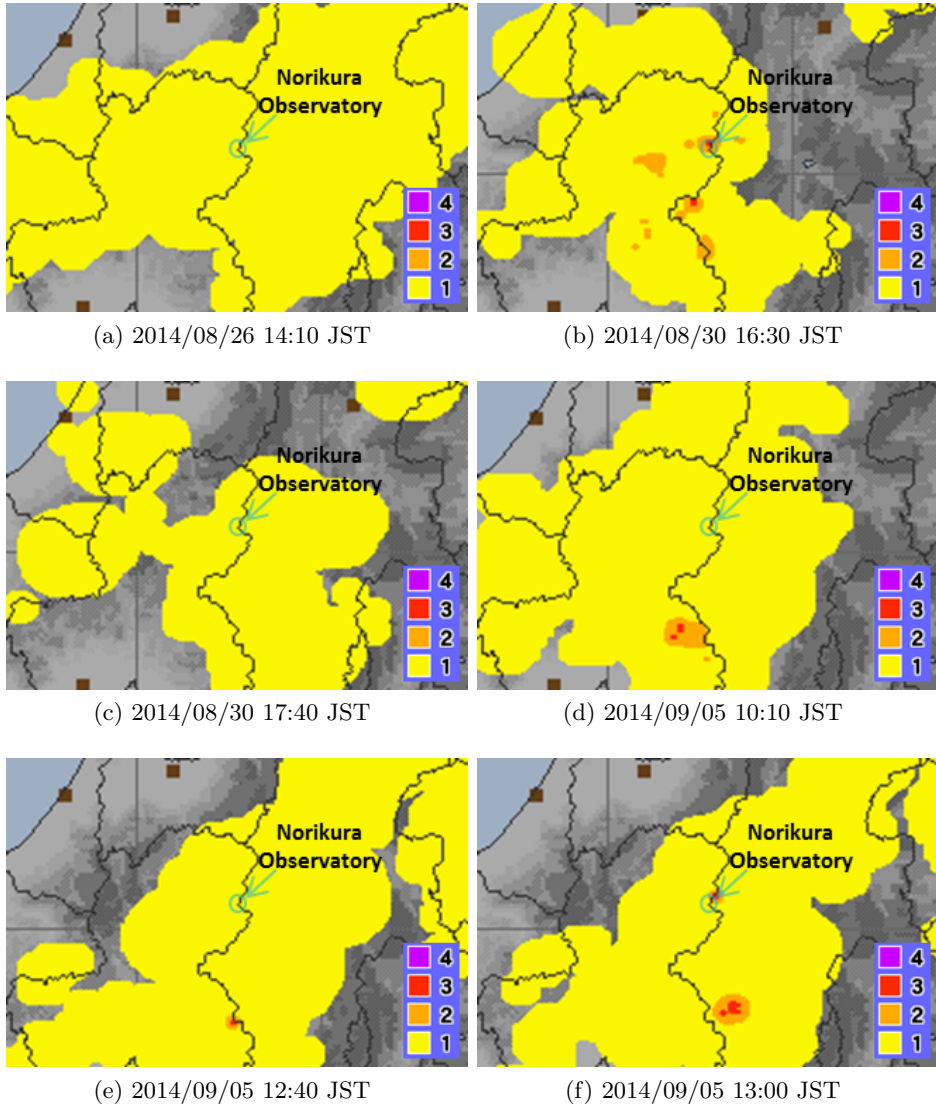
Figure 6.18: Images of Thunder Nowcast recorded around 6 bursts (burst20140826-1 to burst20140905-3); These figures were obtained from [1] and edited properly.

the status of thundercloud activity of each grid of 5 km × 5 km in 3 levels every 3 minutes.

As shown in Table 6.5, Level 1 to 3 corresponds to thundercloud activity of weak, medium and strong status respectively. The level of Thunder Information is decided by analyzing thundercloud status observed by meteorological radars. However, it is noted that the level of thunder activity does not necessarily match the actual occurrence of lightning discharges. In the same manner as Thunder Nowcast, Level 0 was defined in order to represent the status that no thunder activity level was shown.

Considering the grid scale and update frequency, the highest level of Thunder Information in 3 × 3 grids which corresponded to 15 km × 15 km around Norikura Observatory recorded within 10 minutes from burst periods were investigated. The results are shown in Table 6.4 along with the highest levels of Thunder Nowcast.

Level 1 - 3 in one or more grids was recorded 51 times in 54 days of the measurement period. "Thunderstorms ≥ Level 1" were observed 15 times if it was defined in the same manner as Thunder Nowcast. Six of them were recorded within 10 minutes from burst periods of 7 bursts. All of these 7 bursts corresponded to Level 2 or higher of Thunder Nowcast.

Other 5 bursts were not in coincidence with Level 1 - 3 of Thunder Information. The thundercloud activity was not observed by Thunder Information in those burst periods probably due to relatively small scale of thunderclouds. Those 5 bursts corresponded to Level 1 or 2 of Thunder Nowcast as shown in Table 6.4. However, the result of Thunder Information was basically complementary to the information obtained from Thunder Nowcast.

Table 6.5: Thunder activity levels of Thunder Information [3]

Level	Status
(0)	(Thundercloud activity is not being observed.)
1	Thundercloud activity of weak status is being observed.
2	Thundercloud activity of medium status is being observed.
3	Thundercloud activity of strong status is being observed.

6.3 Electric field and lightning flashes

During the measurement at Norikura Observatory, a field mill and a light sensor had been installed around PANDA64 in order to measure electric field strength and detect lightning flashes respectively. The correlation between thundercloud activity and radiation bursts were investigated by utilizing these data.

6.3.1 Measurement period of field mill and light sensor

The field mill was installed at approximately 10 m from the van and measured electric field strength every second as described in 4.1.2. The field mill took data successfully after August 20th 2014, whereas data could not be taken during the first half of the measurement period probably due to poor connection of a cable. The electric field strength was measured during 8 burst periods observed after August 20th 2014.

On the other hand, the light sensor was attached on the roof of the driver's seat of the van and the output signal was recorded every second by the data logger. The pulse signal of a lightning was extended to more than one second and thus could be detected with the frequency of 1 Hz as described in 4.1.3. However, the light sensor could not be operated in most part of the measurement period due to frequent troubles caused by strong rain storms. The light sensor could take data successfully only during burst20140708-1 and burst20140830-1 in 12 burst periods.

Temporal variation of the light intensity and/or the electric field are plotted in Figure 6.19 - 6.21 along with 30-second temporal variation of 3 - 100 MeV count rate. Burst20140830-1 was the only burst which could be observed along with both the light sensor and the field mill data.

6.3.2 Electric field and lightning flashes during bursts

Around the burst period of burst20140708-1, several lightning flashes were repeatedly detected for more than 30 minutes with intervals of a few minutes (Fugure 6.19a). Besides, a lightning flash was also detected during the burst period of burst20140830-1 as shown in Fugure 6.20b.
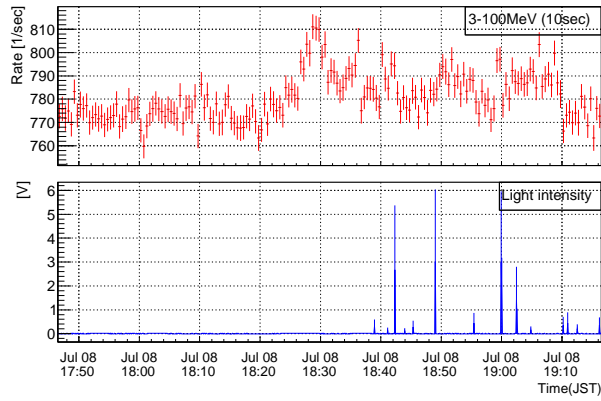
(a) burst20140708-1
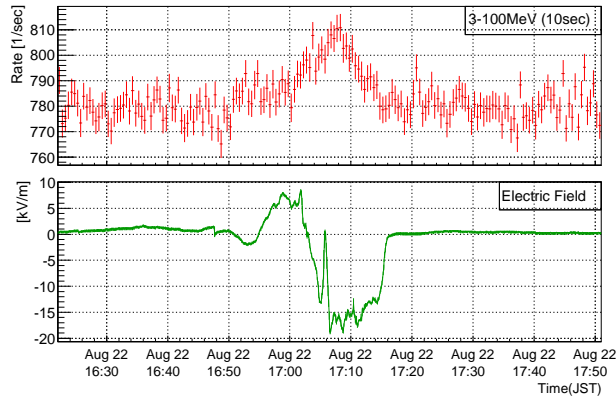
(b) burst20140822-1
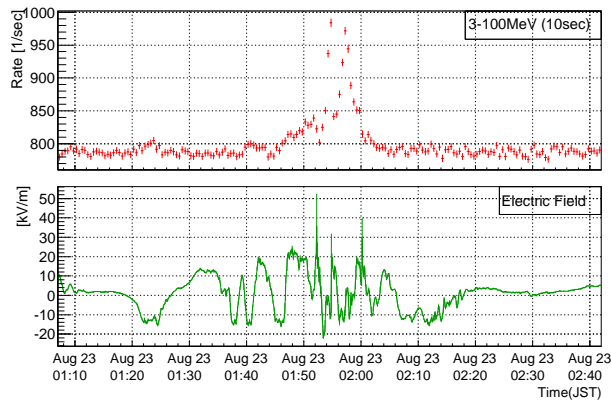
(c) burst20140823-1

Figure 6.19: 30-second temporal variation of 3-100 MeV count rate (red), light intensity (blue) and electric field (green) around burst20140708-1, burst20140822-1 and burst20140823-1
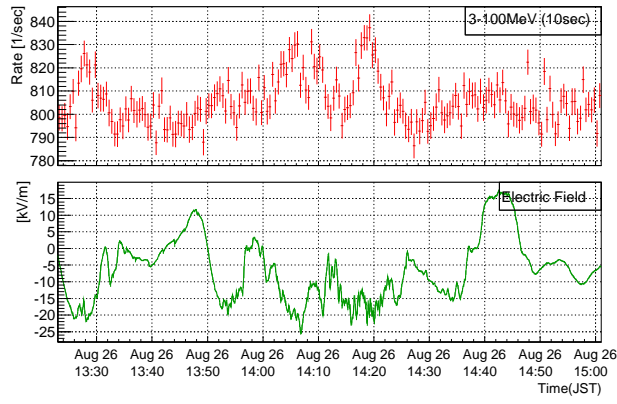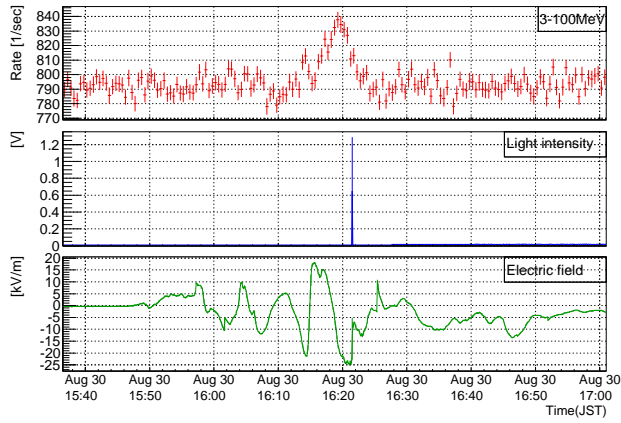
(a) burst20140826-1
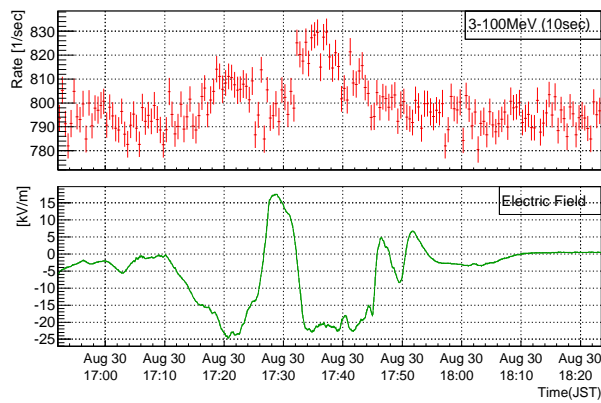
(b) burst20140830-1

(c) burst20140830-2

Figure 6.20: Same as Figure 6.19 but for burst20140826-1, burst20140830-1 and burst20140830-2
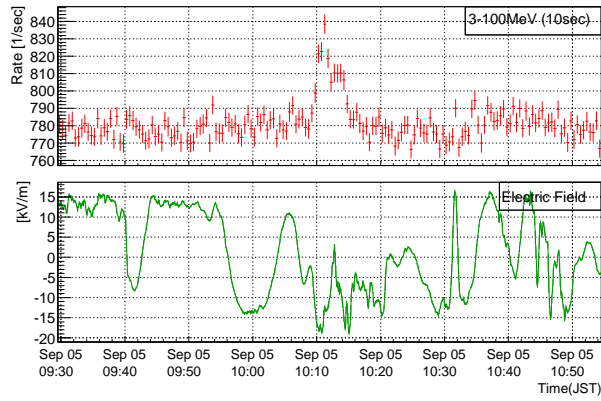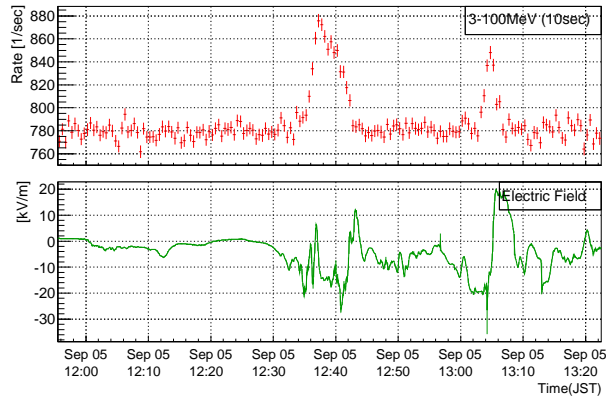
(a) burst20140905-1
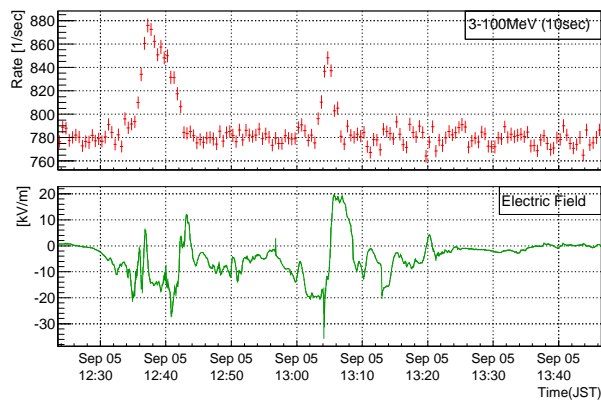
(b) burst20140905-2

(c) burst20140905-3

Figure 6.21: Same as Figure 6.19 but for burst20140905-1, burst20140905-2 and burst20140905-3

The electric field on the ground is stable around 0 kV/m while thunderclouds are not approaching. When dipole thunderclouds which have negative charges in the bottom layer and positive charges in the upper layer come close, the field mill is expected to show positive value at first in response to the upper positive layer of the thundercloud. Then it is expected to turn to negative value beneath the thunderclouds because of negative charges just above the field mill. When it come out of thunderclouds, the field mill will again turn to positive value temporarily before going back to the background level of approximately 0 kV/m.

The electric field was very unstable around the burst periods as shown in the figures, which showed large fluctuation from -36 kV/m (recorded in burst20140905-2) to $+53$ kV/m (recorded in burst20140823-1). This result strongly indicated that thunderclouds existed around the detector during the burst periods. Negative electric fields lower than -10 kV/m were recorded near the peaks of the burst periods, which might indicate that the lower negative layer of thunderclouds existed above the detector.

When a lightning flash was observed during burst20140830-1, the electric field suddenly fluctuated to positive direction in one second. It was suggested that a lightning discharge occurred at that moment. The sudden fluctuations of electric field observed in other bursts also seemed to be due to lightning discharges although the light sensor data could not be taken.

6.4 Energy spectra of radiation bursts

6.4.1 Spectra observed at Norikura

Energy spectra of 12 bursts observed at Norikura Observatory were obtained from subtraction of the burst period (defined in Table 6.1) and the corresponding background period. The energy spectra are shown in Figure 6.22 - 6.25 along with spectra of both burst and background periods before subtraction. In the figures, arrows are drawn as the upper limits of 95 % confidence level when data points are below the graph region. It should be noted that the energy spectrum of > 3 MeV range was drawn in the figures because the reliability of the energy spectrum below 3 MeV was

low due to rain fallout.

These energy spectra indicated that they decayed exponentially toward high energy range. The energy spectra extend up to high energy especially in burst20140823-1 and burst20140905-2, whose highest energy bins of 3 σ significance in logarithmic scale were 30 MeV.

6.4.2   Comparison with Ohi's energy spectra

We compared the energy spectra of 12 bursts observed at Norikura Observatory by PANDA64 and 3 bursts observed at Ohi Power Station by PANDA36. The energy spectra of three bursts observed at Ohi extended up to 15 MeV, 20 MeV and 20 MeV respectively [2] when plotted with energy bins of 5 MeV width. With the same bin width, the energy spectra obtained at Norikura had the maximum energies of 10 - 25 MeV. The highest energy bin of 5 MeV width which had 5 σ significance is shown in Table 6.6 for each burst observed at Norikura and Ohi. While the energy spectra of burst20140823-1 and burst20140905-2 extended up to 25 MeV, some Norikura's bursts extended up to 10 MeV probably due to low statistics.

We also compared the shape of the energy spectra. Each spectrum was fitted to an exponential function with the range of 3 - 15 MeV although this was a rough assumption. The fitted function was Rate[/sec/MeV] = $\exp(c + s \times \text{Energy[MeV]})$, where c was the constant and s was the slope of exponential function.

The fitting results of Norikura's and Ohi's bursts are shown in Figure 6.26 - 6.27 and listed in Table 6.6. The mean value of slope s, which was corresponding to the intensity of high energy range, was -0.224 among 12 bursts observed at Norikura Observatory, whereas it was -0.325 among 3 bursts observed at Ohi Power Station. The steepest slope of Norikura's bursts ($s = -0.263$ for burst20140719-1 and burst20140731-1) was gentler than the slopes of three Ohi's bursts. Assuming that the count rate of 3 MeV is 1, the count rate at 15 MeV becomes 0.068 with Norikura's slope ($s = -0.224$) and 0.020 with Ohi's slope ($s = -0.325$).

Since PANDA36 deployed at Ohi Power Station and PANDA64 deployed
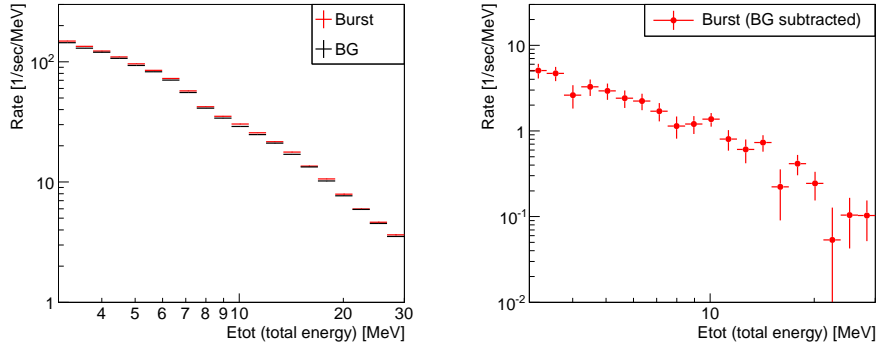
(a) burst20140708-1
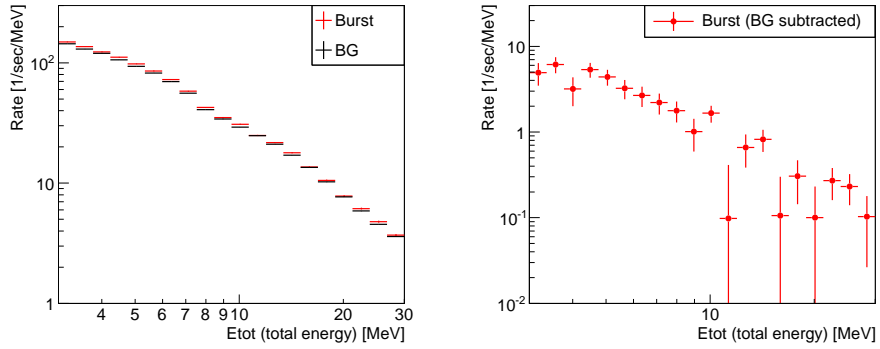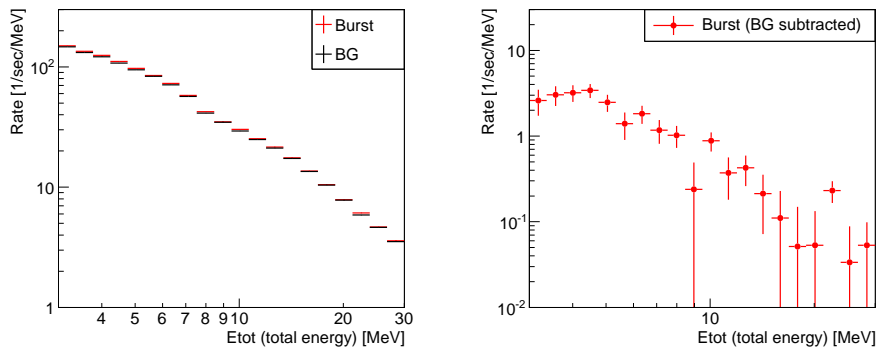
(b) burst20140718-1

(c) burst20140719-1

Figure 6.22: Energy spectrum of burst20140708-1, burst20140718-1 and burst20140719-1; (left) burst and background period; (right) burst period (background subtracted); Error bars are statistical 1 σ.
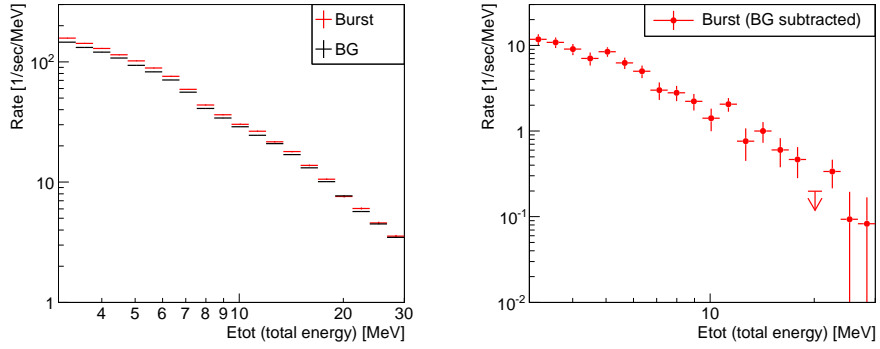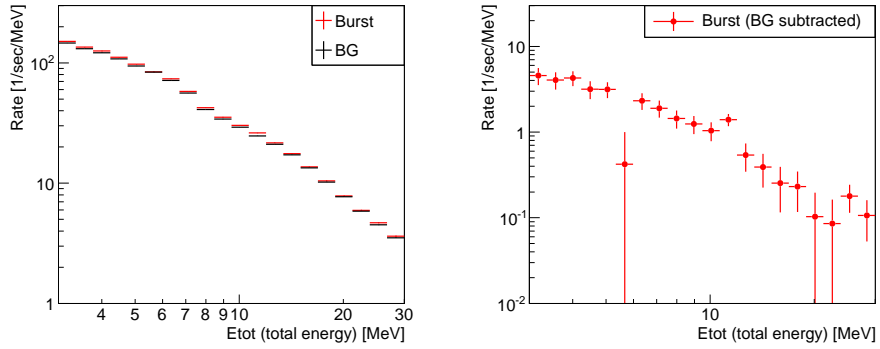
(a) burst20140731-1
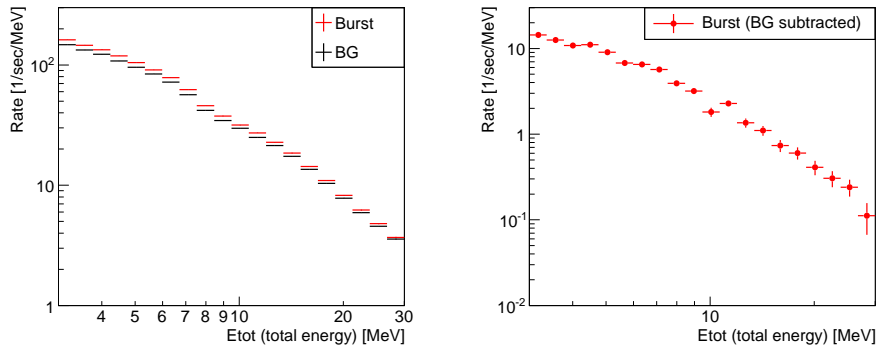
(b) burst20140822-1

(c) burst20140823-1

Figure 6.23: Same as Figure 6.22 but for burst20140731-1, burst20140822-1 and burst20140823-1
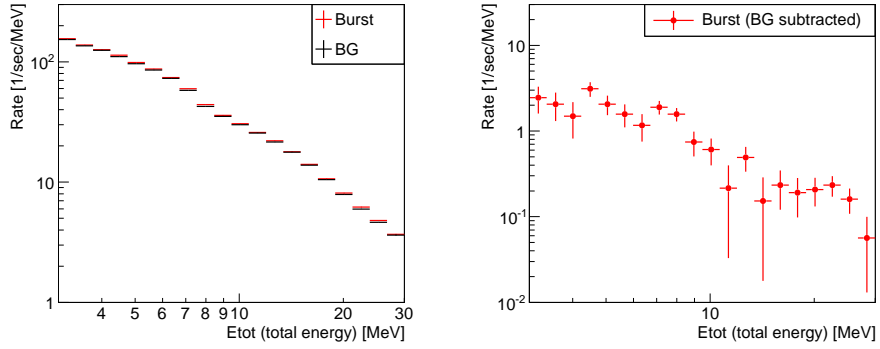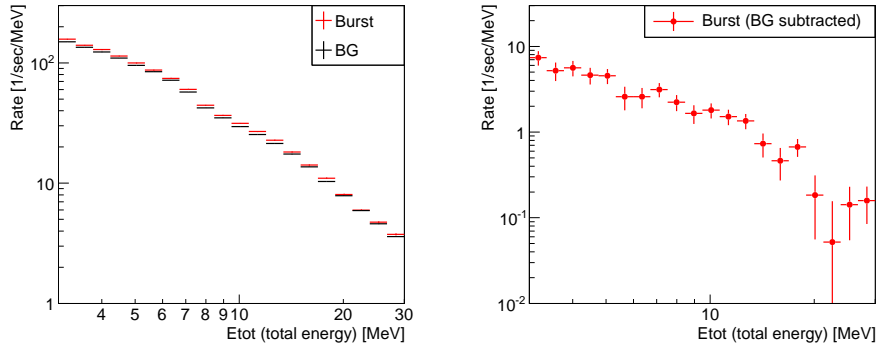
(a) burst20140826-1
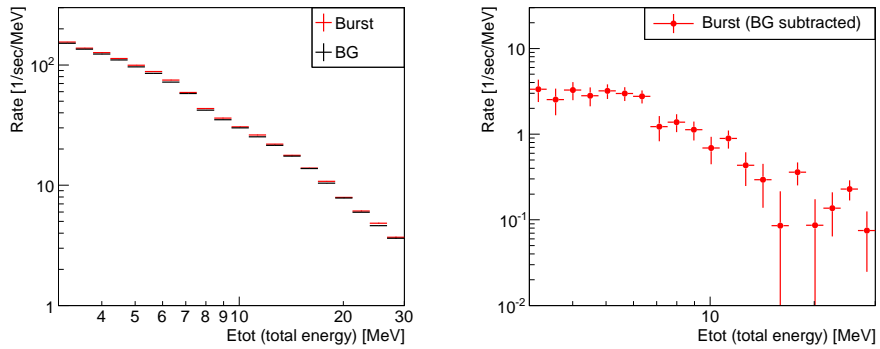
(b) burst20140830-1

(c) burst20140830-2

Figure 6.24: Same as Figure 6.22 but for burst20140826-1, burst20140830-1 and burst20140830-2
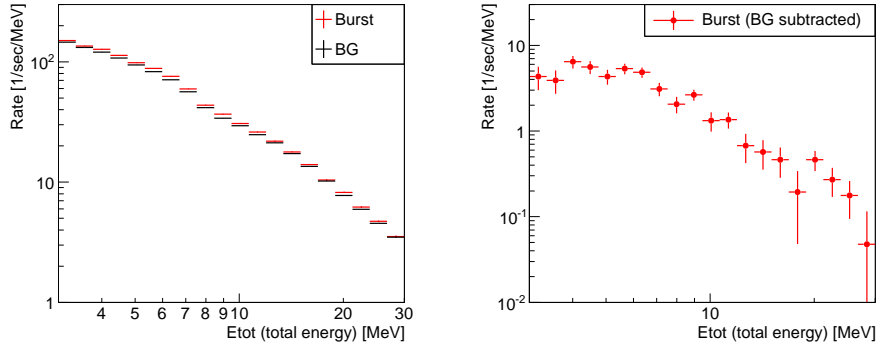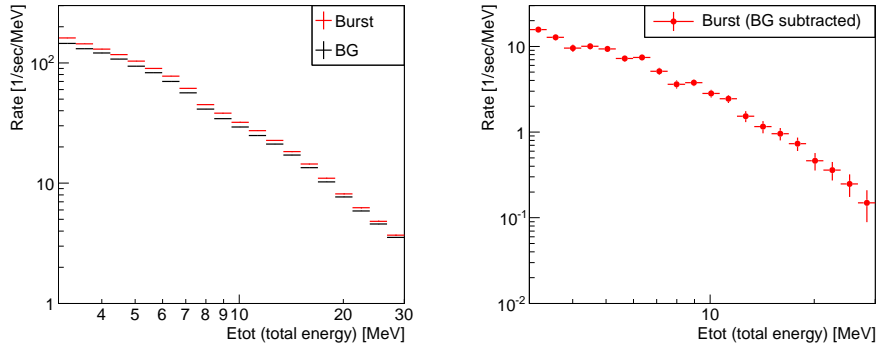
(a) burst20140905-1
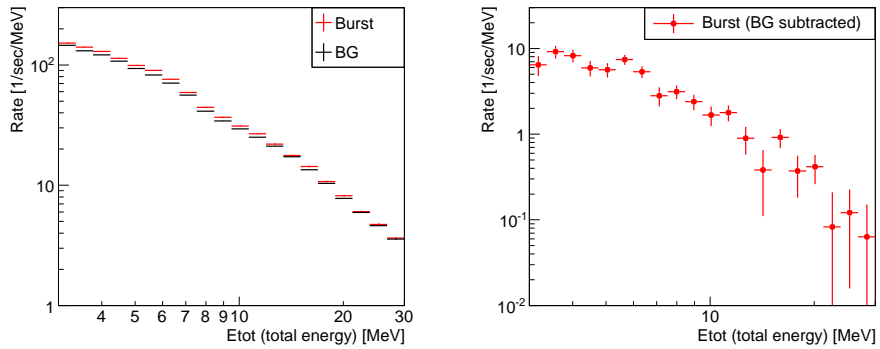
(b) burst20140905-2

(c) burst20140905-3

Figure 6.25: Same as Figure 6.22 but for burst20140905-1, burst20140905-2 and burst20140905-3

at Norikura Observatory were basically identical detectors except for the number of modules, they were considered not to have big difference between their detector response. Therefore, the difference in the slopes of exponential fitting might indicate that the ratio of high energy component included in radiation bursts would differ between two locations. In order to take the detector response into account, a further investigation using Monte Carlo simulation was performed in the next chapter to figure out the difference of the bursts.

Table 6.6: The highest energy of 5 MeV bin width with 5σ significance and the result of exponential fitting (Rate[/sec/MeV] $= \exp(c + s \times$ Energy[MeV])) of the energy spectra observed at Norikura Observatory and Ohi Power Station

Location	Burst	Energy	c	s	χ^2/dof
Norikura	20140708-1	15 MeV	2.00 ± 0.17	-0.189 ± 0.022	8.5/10
Norikura	20140718-1	10 MeV	2.53 ± 0.20	-0.242 ± 0.030	7.6/10
Norikura	20140719-1	10 MeV	2.10 ± 0.21	-0.263 ± 0.033	14.0/10
Norikura	20140731-1	15 MeV	3.26 ± 0.13	-0.263 ± 0.020	7.4/10
Norikura	20140822-1	15 MeV	2.01 ± 0.18	-0.194 ± 0.023	18.1/10
Norikura	20140823-1	25 MeV	3.44 ± 0.05	-0.250 ± 0.008	18.0/10
Norikura	20140826-1	10 MeV	1.75 ± 0.19	-0.215 ± 0.026	13.8/10
Norikura	20140830-1	20 MeV	2.31 ± 0.16	-0.178 ± 0.020	10.0/10
Norikura	20140830-2	15 MeV	2.05 ± 0.17	-0.215 ± 0.023	15.1/10
Norikura	20140905-1	15 MeV	2.57 ± 0.13	-0.207 ± 0.017	17.7/10
Norikura	20140905-2	25 MeV	3.35 ± 0.07	-0.231 ± 0.009	11.9/10
Norikura	20140905-3	15 MeV	3.03 ± 0.14	-0.243 ± 0.020	12.3/10
Ohi	20111225	15 MeV	3.74 ± 0.04	-0.305 ± 0.007	11.8/10
Ohi	20120102	20 MeV	4.82 ± 0.03	-0.306 ± 0.005	15.4/10
Ohi	20120105	20 MeV	4.59 ± 0.03	-0.365 ± 0.004	6.9/10
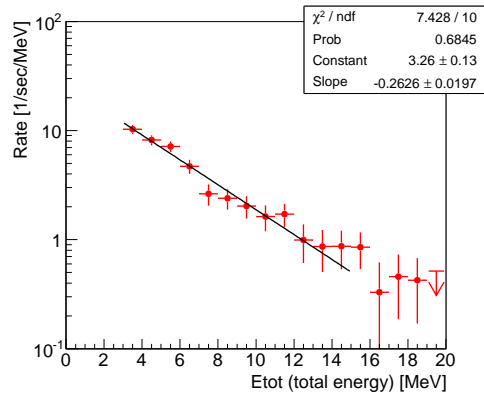
(a) burst20140731-1
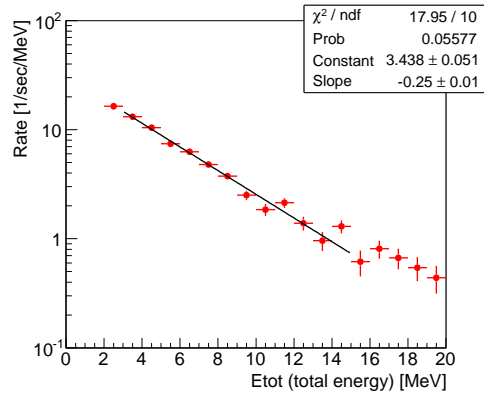
(b) burst20140823-1
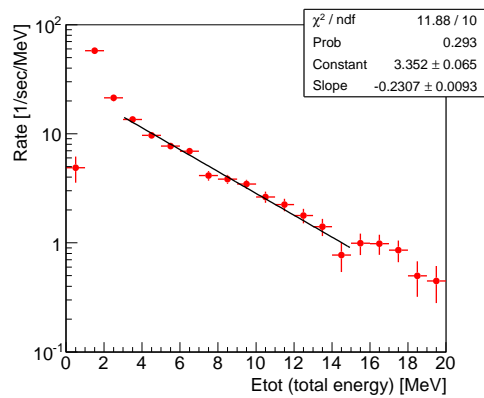
(c) burst20140905-2

Figure 6.26: Examples of exponential fitting of energy spectra observed at Norikura Observatory
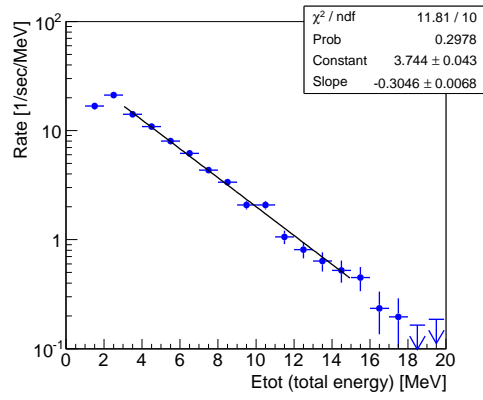
(a) burst20111225
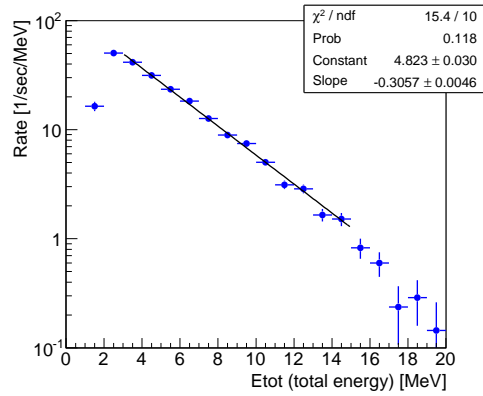
(b) burst20120102
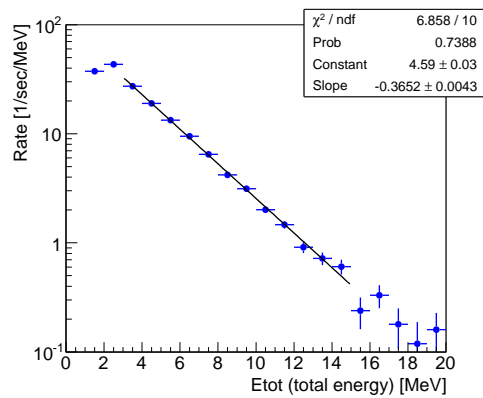
(c) burst20120105

Figure 6.27: Exponential fitting of energy spectra observed at Ohi Power Station: These spectra were obtained from [2] and the bin width was changed properly.

Chapter 7

Runaway electron source estimation

The radiation bursts observed at Norikura Observatory seemed to be caused by an avalanche-type multiplication process of runaway electrons. Runaway electron sources lying in thunderclouds were investigated in order to understand the generation process of radiation bursts. A Monte Carlo simulation was performed using Geant4 simulation toolkit [68] to estimate the position and energy of runaway electrons in the air which were the most likely to cause the observed bursts.

7.1 Monte Carlo simulation of electron acceleration in electric field

7.1.1 Simulation setup of electron acceleration

To investigate the angular distribution of runaway electrons at the end of acceleration region, a Monte Carlo simulation of electron acceleration was performed using Geant4 toolkit. In the simulation, seed electrons of 1 MeV were injected vertically downward from the upper end of the uniform acceleration region which had appropriate electric field. In the electric field, a part of the seed electrons were accelerated downward producing a large number of knock-on electrons and bremsstrahlung photons. Figure 7.1 shows an example of the simulation.

At the lower end of the acceleration region, the zenith angular distribution of runaway electrons was obtained. The electric field was set to

320 kV/m and 500 kV/m with vertical length of 500 - 2000 m and 50 - 200 m respectively. The atmospheric density was set to the value at sea level.
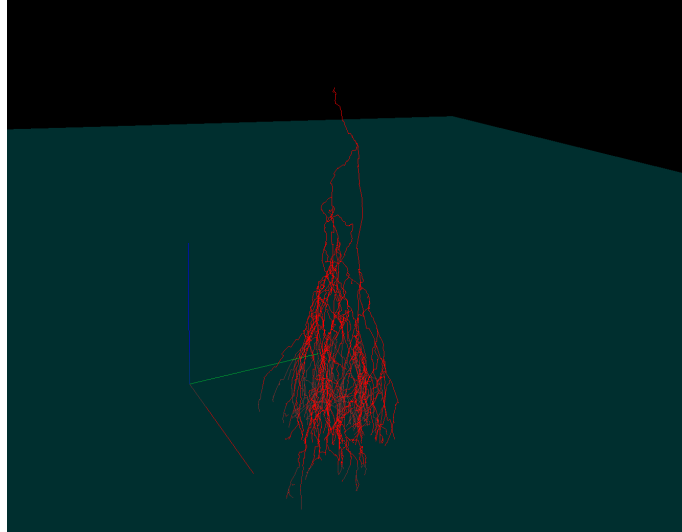
Figure 7.1: Monte Carlo simulation of electron acceleration in electric field; An electron was accelerated downward in 200 m electric field of 500 kV/m; Trajectories of only electrons (red) are shown. Each axis corresponds to 100 m.

7.1.2 Simulated angular distribution of runaway electrons

The zenith angular distribution of runaway electrons with the energy of > 10 MeV are shown in Figure 7.2 for each electric field and acceleration length. Although the angular distribution differed depending on the electric field and the length of acceleration region, 90 - 95 % of runaway electrons with energy of > 10 MeV were within $\theta < 30°$.

Since the angular distribution was also expected to depend on runaway electron energy, we decided to simply assume runaway electrons as vertically downward at the next step of Monte Carlo simulation. As a conservative assumption, another angular distribution proportional to $\cos\theta$ was also tested at the next step in order to estimate systematic error of the vertical assumption.
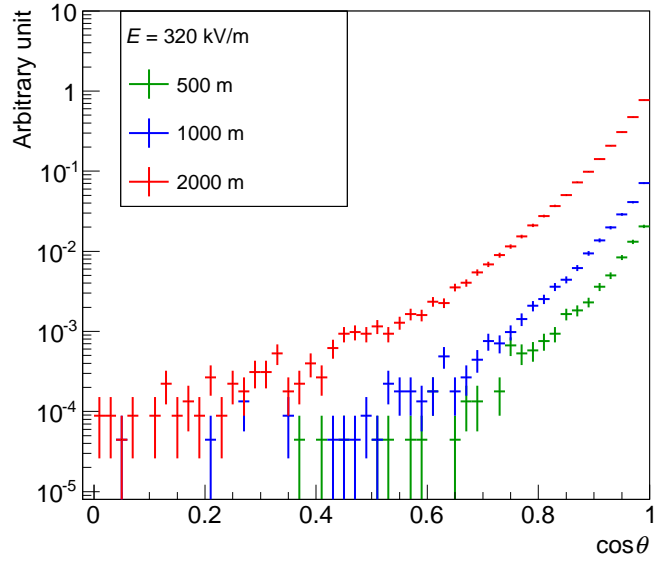
(a) 320 kV/m
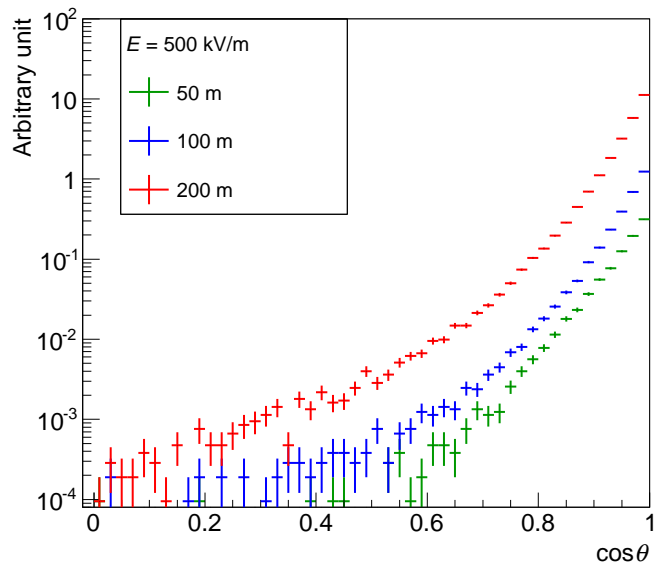
(b) 500 kV/m

Figure 7.2: Simulated distribution of zenith angle cosθ of runaway electrons of > 10 MeV at the end of the acceleration region

7.2 Monte Carlo simulation of electron propagation in the air

7.2.1 Simulation setup of electron propagation

As described in 1.1, electrons which are more energetic than threshold energy are accelerated to relativistic energy by electric fields in thunderclouds and expected to approach monochromatic energy as they go through electric fields. Here for simplicity, runaway electrons of monochromatic energy emitted vertically downward in the air were assumed in order to estimate the most likely energy and height of runaway electron sources.

Figure 7.3 shows the schematic view of the simulation. In a space of 4 km × 4 km × 2 km filled with air molecules, electrons of E_e [MeV] were shot vertically downward from the central point at the height of h [m] above the ground. The energy spectra of gamma-rays and electrons which reached the ground surface were obtained respectively for each combination of E_e and h.

The height h of runaway electrons was set to 20 steps of 100 m width from 100 m to 2000 m, while the energy E_e was set to 19 steps of 5 MeV width from 10 MeV to 100 MeV. All 20 × 19 combinations of height and energy were simulated and gamma-rays and electrons were collected individually at the ground. Since Norikura Observatory is located at high altitude, the air pressure at the bottom of the simulation space was set to 720 hPa corresponding to 2,770 m above sea level and it got 10 hPa lower per 100 m altitude. Figure 7.4 is an example of the simulation.

7.2.2 Simulated particle components at ground surface

Incident electrons propagated toward the ground surface through various processes such as bremsstrahlung or ionization. The components of particles incident on the ground were mostly photons and electrons. Positrons were slightly mixed to the incident particles in less than 2 %.

The number of photons and electrons of > 3 MeV incident on the ground per a runaway electron ("arrival rate") were counted and shown in Figure 7.5. The arrival rate of incident particles was rather smaller (< 0.01)
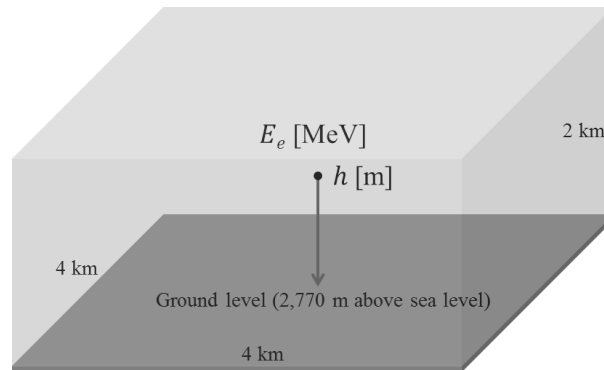
Figure 7.3: Schematic view of Monte Carlo simulation of electron propagation in the air : Electrons of E_e [MeV] were shot from the height of h [m] vertically downward to the ground surface at 2,770 m altitude.
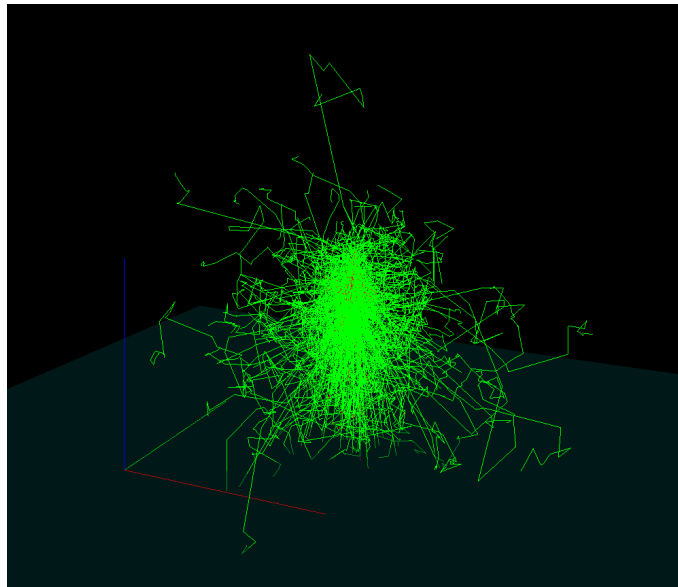
Figure 7.4: Monte Carlo simulation of electron propagation; 100 electrons of 50 MeV were shot downward from $h = 1000$ m; Trajectories of gamma-rays (green) and electrons (red) are shown. Each axis corresponds to 1 km.

when h is high and E_e is low. On the other hand, the arrival rate exceeded 1 in some cases with the height $h \leq 700$ m and the energy $E_e \geq 30$ MeV because of the multiplication process by energetic particles. The minimum arrival rate was 0.000504 at (2000 m, 10 MeV) and the maximum was 2.29 at (200 m, 100 MeV).

In addition, the ratio of electrons to all particles (gamma-rays and electrons) on the ground of each source height and energy was calculated and shown in Figure 7.6. Gamma-rays were dominant in most heights and energies, while electrons were dominant with 25 - 100 MeV at the height of 100 m. In the high energy range, the electron ratio at each height tended to change gradually compared to lower energy range. The maximum and the minimum of electron ratio on the ground were 0.72 at (100 m, 30 MeV) and 0.006 at (500 m, 10 MeV) respectively.
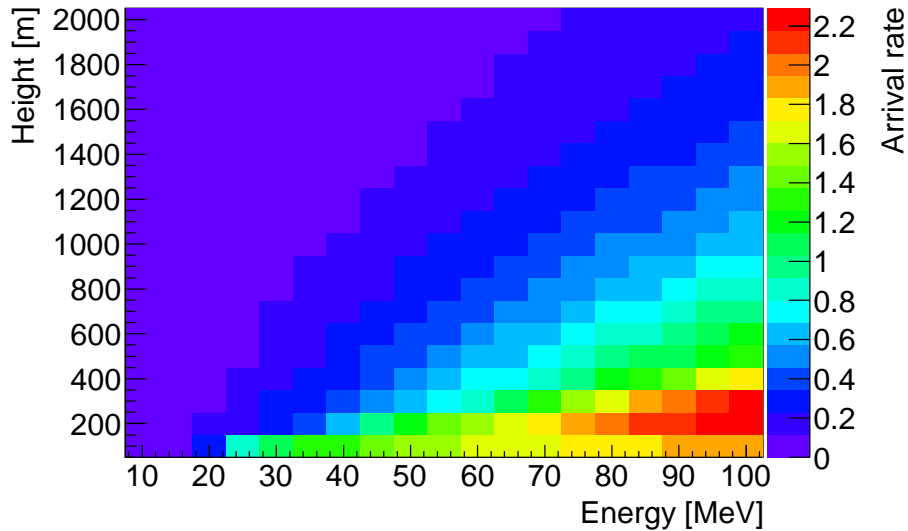
Figure 7.5: Simulated arrival rate of photons and electrons (> 3MeV) at the ground surface (2,770 m) per an incident electron injected from the air

7.2.3 Simulated energy spectrum at the ground surface

The energy spectra of gamma-rays and electrons incident on the ground surface corresponding to $h = 200$ m, 500 m, 1000 m, 2000 m and $E_e =$
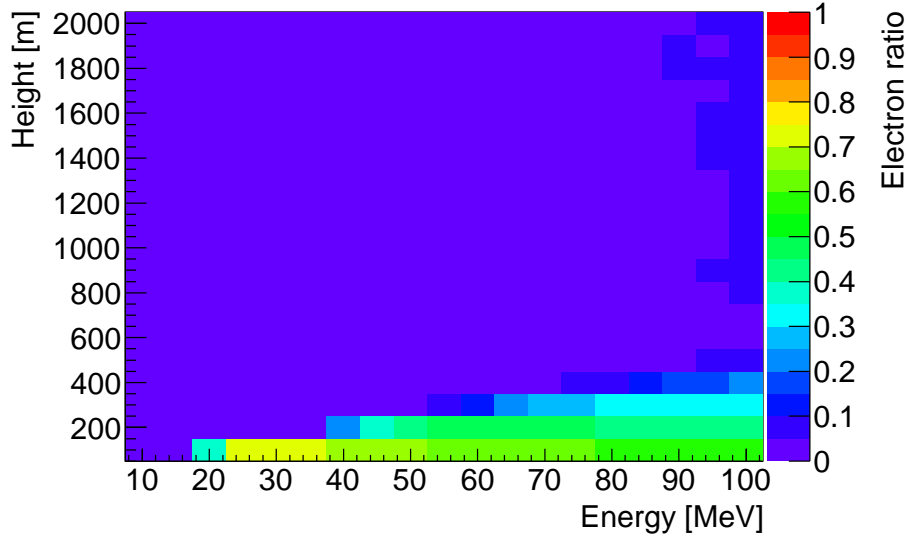
Figure 7.6: Simulated electron ratio to all particles (gamma-rays + electrons) at the ground surface

20 MeV, 50 MeV, 100 MeV are shown in Figure 7.7. In the figure, the spectra of electrons at (200 m, 50 MeV) and (200 m, 100 MeV) had characteristic flat shapes with cut-off energy. Other spectra of electrons and gamma-rays had relatively similar shapes which decreased toward high energy, although the slope and the cut-off energy were different among each spectrum. For example, the slope of the gamma-ray spectrum at (200 m, 20 MeV) was steeper than (2000 m, 20 MeV). These simulated spectra were utilized for the next step of Monte Carlo simulation in the following section.

7.3 Monte Carlo simulation of detector response

7.3.1 Simulation setup of detector response

As the final step of Monte Carlo simulation for estimating the most likely runaway electron sources, the detector response of PANDA64 was simulated. In this simulation, energy spectra and angular distribution of gamma-rays and electrons obtained from the simulation described in the previous section were utilized. Gamma-rays and electrons of > 3 MeV were shot toward
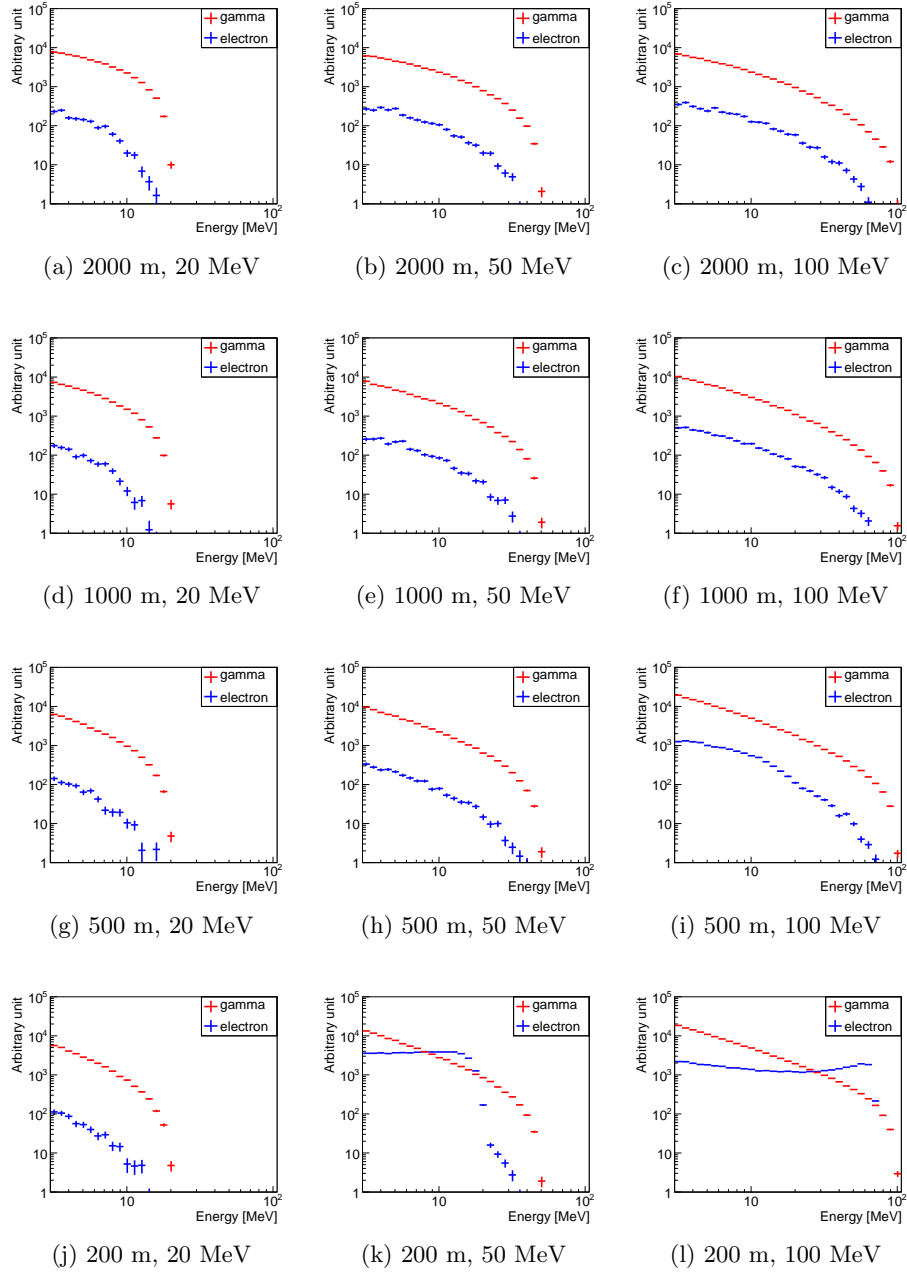
Figure 7.7: Simulated energy spectra of gamma-rays (red) and electrons (blue) at the ground surface generated by monochromatic electrons of 20, 50, 100 MeV incident from 200, 500, 1000, 2000 m

PANDA64 in order to simulate its detector response.

The schematic view of the simulation is shown in Figure 7.8. The structure of PANDA64 was constructed including all module components such as plastic scintillators, light guides, PMTs and gadolinium sheets along with aluminum frames and plates covering the detector. At 90 cm above the detector, a 2 mm-thick aluminum plate of 2 m × 3 m was placed corresponding to the ceiling of the van. Gamma-rays and electrons were projected downward from 2 m × 3 m horizontal plane 20 cm above the aluminum ceiling. The energy and zenith angle of injection particles were obtained from the simulation of electron propagation in the atmosphere, while the shot points on the projection plane were chosen randomly. An example of the simulation is shown in Figure 7.9.
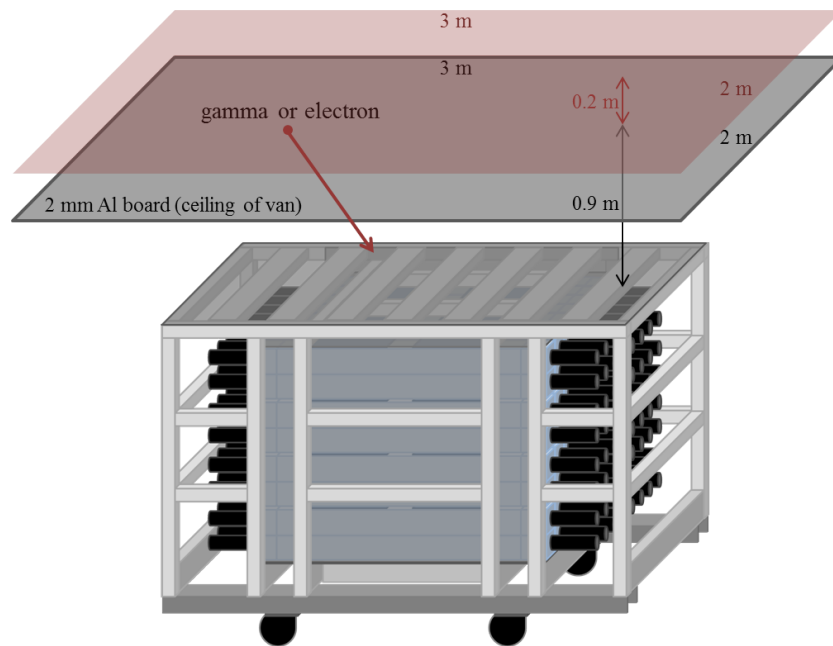
Figure 7.8: Schematic view of Monte Carlo simulation of detector response: Gamma-rays and electrons were shot downward from random points on the horizontal plane 1.1 m above the detector through a 2 mm-thick aluminum plate.
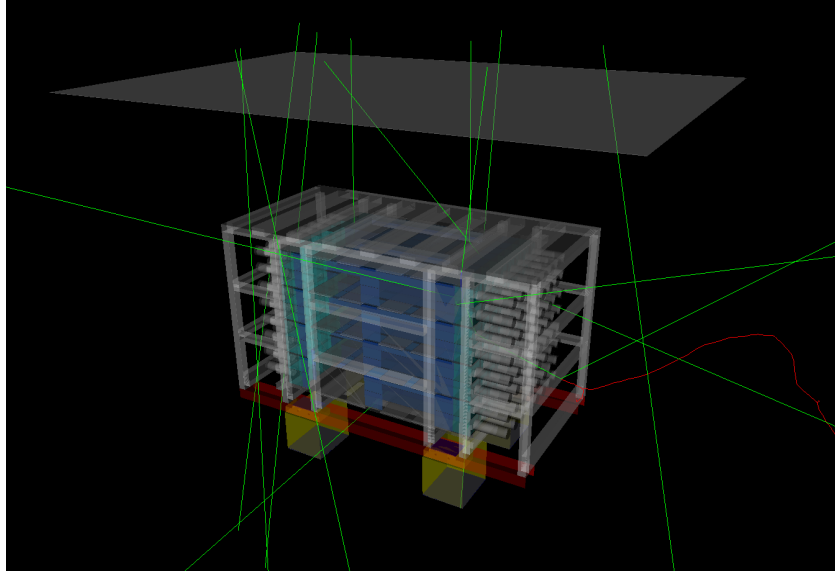
Figure 7.9: Monte Carlo simulation of detector response; 10 gamma-rays were shot toward PANDA64; Trajectories of gamma-rays (green) and electrons (red) are shown.

7.3.2   Simulated detector response of PANDA64

The energy spectra of PANDA64 obtained from incident gamma-rays and electrons corresponding to each runaway electron source at height h and energy E_e were summed up respectively in order to be fitted to the spectra of radiation bursts observed at Norikura Observatory. Each energy deposit on plastic scintillators were smeared and applied to the software cuts described in 5.3.

The energy spectra collected for fitting through this Monte Carlo simulation were:

- E_{tot} spectrum of all events detected by PANDA64 ("total-E_{1st}")

- E_{tot} spectrum of which E_{1st} was situated in upper modules of PANDA64 ("upper-E_{1st}")

- E_{tot} spectrum of which E_{1st} was situated in inner modules of PANDA64 ("inner-E_{1st}").

for all combinations of h and E_e. The "upper" modules corresponded to 6 modules on the top stage of 8×8 modules except for 2 edge modules, and the "inner" modules corresponded to inner 36 (6×6) modules of PANDA64 as shown in Figure 7.10. The upper-E_{1st} and inner-E_{1st} spectra were utilized to investigate the particle components of observed bursts by E_{1st} distribution, which will be discussed in the following chapter.

The simulated energy spectra of total-E_{1st}, upper-E_{1st} and inner-E_{1st} corresponding to h = 200 m, 500 m, 1000 m, 2000 m and E_e = 20 MeV, 50 MeV, 100 MeV are shown in Figure 7.11. The energy spectra of 3 - 30 MeV are plotted in the figure. These spectra slightly differs among each combination of h and E_e.

Figure 7.10: Schematic view of "upper modules" (red) and "inner modules" (black) of PANDA64
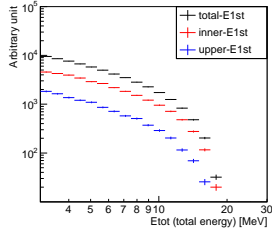
(a) 2000 m, 20 MeV
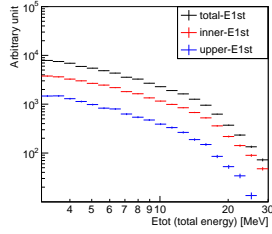
(b) 2000 m, 50 MeV
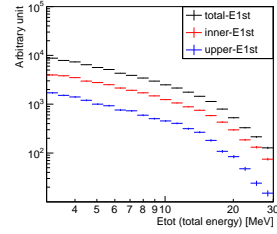
(c) 2000 m, 100 MeV
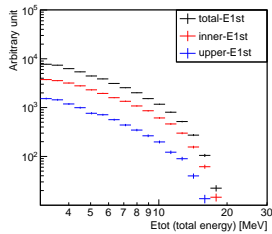
(d) 1000 m, 20 MeV
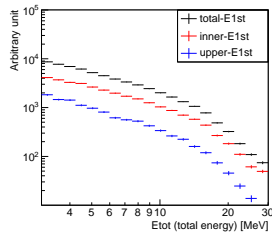
(e) 1000 m, 50 MeV
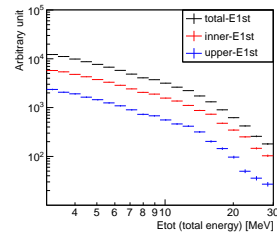
(f) 1000 m, 100 MeV
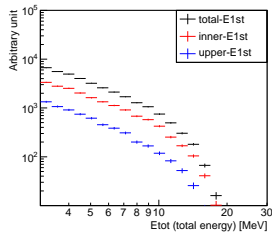
(g) 500 m, 20 MeV
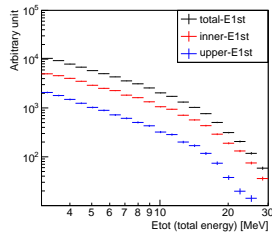
(h) 500 m, 50 MeV
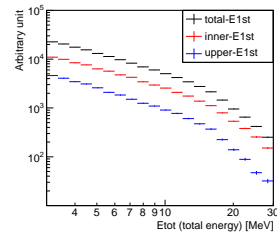
(i) 500 m, 100 MeV
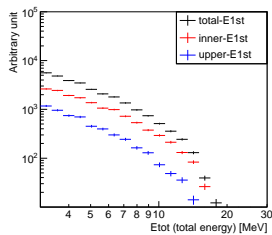
(j) 200 m, 20 MeV
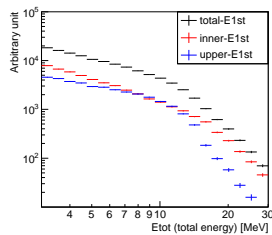
(k) 200 m, 50 MeV
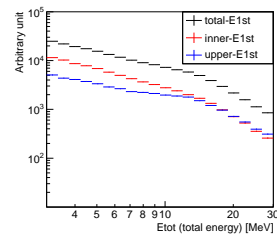
(l) 200 m, 100 MeV

Figure 7.11: Simulated energy spectra of detector response generated by monochromatic electrons of 20, 50, 100 MeV incident from 200, 500, 1000, 2000 m above the ground

7.4 Estimation of runaway electron source in thunderclouds

7.4.1 Fitting of energy spectrum by minimum χ^2 method

Using the energy spectra collected by Monte Carlo simulation of detector response, height and energy of runaway electron sources in thunderclouds were estimated. Three different energy spectra of total-E_{1st}, upper-E_{1st} and inner-E_{1st} obtained from simulated radiation bursts were fitted simultaneously to those of measured bursts by minimum χ^2 method. The only fitting parameter, which was common to all three spectra, corresponded to the height of those histograms. 20 bins of logarithmic scale between 3 MeV and 30 MeV were fitted for each spectrum. The fitting was performed for 12 bursts observed at Norikura Observatory with all combinations of height and energy of runaway electron sources.

7.4.2 Estimated height and energy of runaway electron source

The most likely sources of runaway electrons were estimated for 12 radiation bursts observed at Norikura Observatory. The fitting results are shown in Figure 7.12 - 7.23.

χ^2 values of fitting results were drawn as 2D plot of height and energy in the figures. The red grid in the 2D plot corresponds to the most likely runaway electron source which has the minimum χ^2 value, while the blue grids are out of 99 % confidence region of two parameters. Strong bursts with large significance of statistics (shown in Table 6.2), e.g. burst20140823-1, had narrow confidence regions, while weak bursts had wide confidence regions.

The minimum χ^2 value of each height (or energy) was projected onto the "Height" axis (or "Energy" axis) and also shown in the figures. Three horizontal lines drawn in the plots correspond to 90 %, 95 % and 99 % confidence level of one parameter respectively from bottom to top. For example, burst20140823-1 had the minimum χ^2 at the runaway electron source of (500 m, 40 MeV) and the 90 % confidence interval of the height was

300-500 m. The most likely runaway electron sources and 90 % confidence intervals obtained from these plots are listed in Table 7.1.

Additionally, the measured spectra of total-E_{1st}, upper-E_{1st} and inner-E_{1st} fitted with the simulated spectra of the most likely runaway electron source are shown for each bursts. The simulated energy spectra well described the measured spectra in the fitting region (3 - 30 MeV).

Table 7.1: The most likely height and energy (and the 90 % confidence intervals) of runaway electron sources

Burst	Best fit height (90 % C.L.) [m]	Best fit energy (90 % C.L.) [MeV]	$\chi^2/$dof
20140708-1	1100 (400-1100,1300-1400)	65 (55-)	45.3/59
20140718-1	400 (200-500)	50 (45-95)	79.9/59
20140719-1	300 (200-700)	55 (35-65)	58.3/59
20140731-1	300 (200-500,800)	35 (25-40)	58.0/59
20140822-1	900 (400-1000,1300-1400)	55 (40-70)	52.6/59
20140823-1	500 (300-500)	40 (40)	109.7/59
20140826-1	1600 (800-900,1100-1900)	95 (60-)	99.7/59
20140830-1	500 (500-1000,1300)	80 (60-95)	50.8/59
20140830-2	700 (300-1400,1600)	65 (45,55-)	73.5/59
20140905-1	1700 (1100-1200,1600-1900)	50 (40-70,90)	82.7/59
20140905-2	300 (300)	65 (65)	60.4/59
20140905-3	500 (500,1000)	40 (35-40)	75.1/59

7.4.3 Comparison with Ohi's runaway electron sources

Runaway electron sources of three bursts observed at Ohi Power Station were estimated by a similar simulation method [2]. The result are shown in Table 7.2.

The estimation method for Ohi's bursts was not completely same as Norikura's in some points, such as the fitting procedure utilizing only total-E_{1st} spectrum and the fitting range decided by using statistical significance. However, those results could be comparable with each other because the important feature of the methods was same, i.e. the two-stage Monte Carlo simulation of runaway electron propagation in the air and detector response. The assumption that runaway electrons were monochromatic and vertically

(a)

(b)

(c)

(d)

(e)

(f)
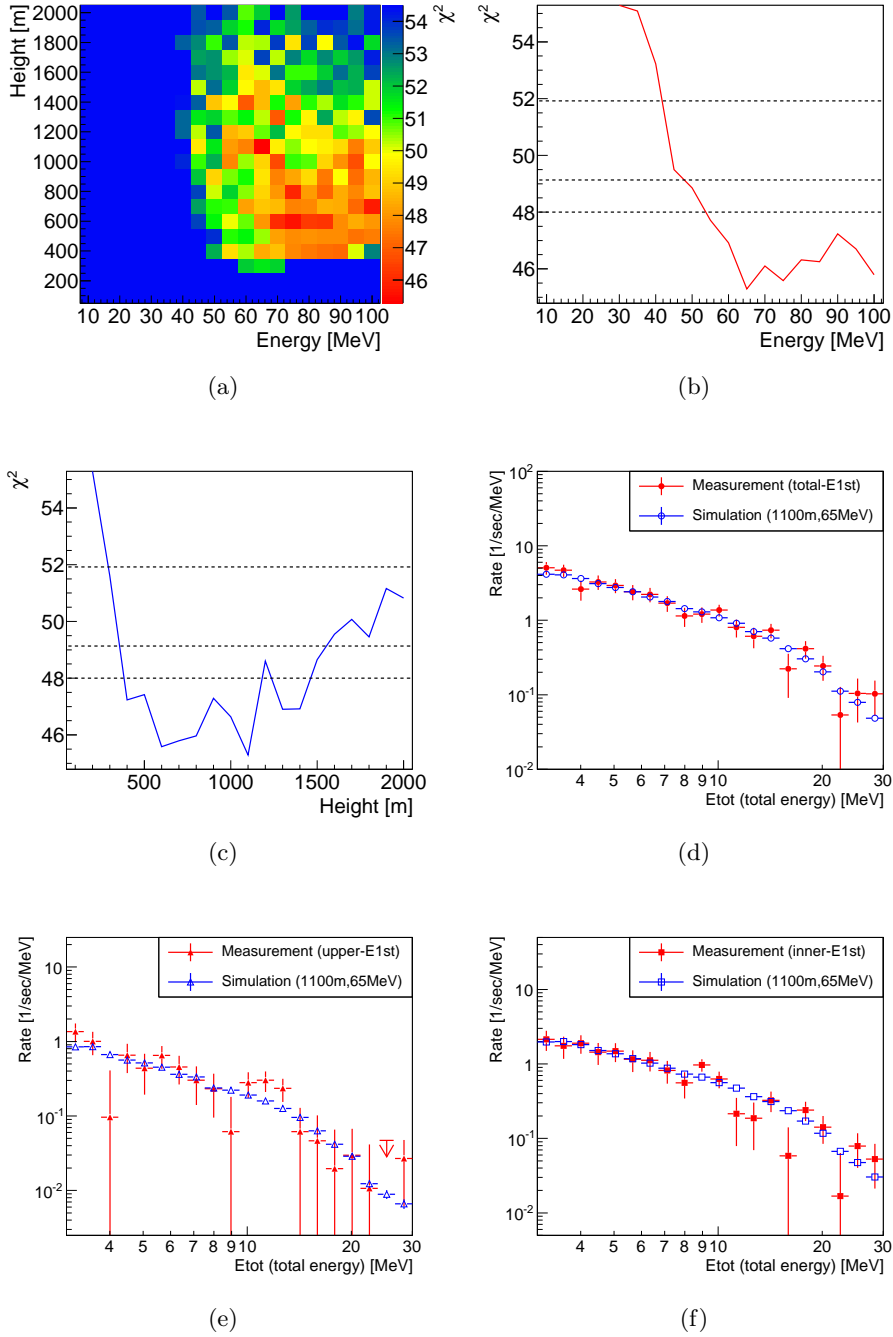
Figure 7.12: Fitting of burst20140708-1 to the simulated data obtained from multiple runaway electron sources; (a) χ^2 value of fitting; (b) χ^2 value projected onto "Height" axis; (c) χ^2 value projected onto "Energy" axis; (d) Measured E_{tot} spectrum and fitted simulation spectrum; (e) E_{tot} spectrum of upper E_{1st}; (f) E_{tot} spectrum of inner E_{1st}
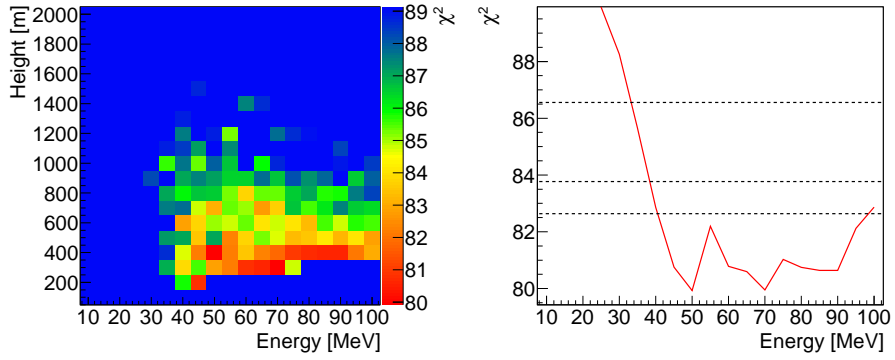
(a)

(b)
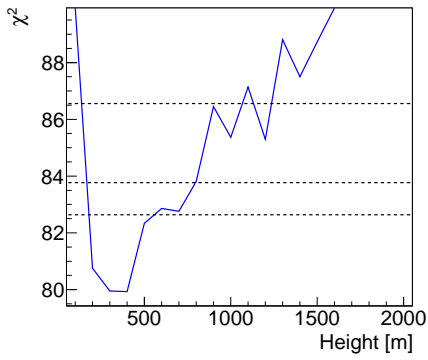
(c)
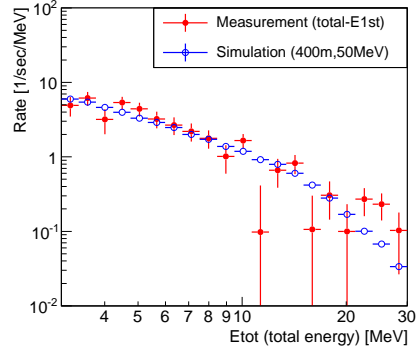
(d)
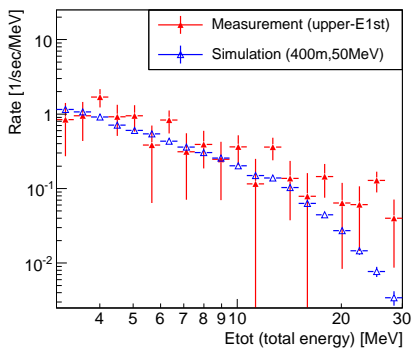
(e)
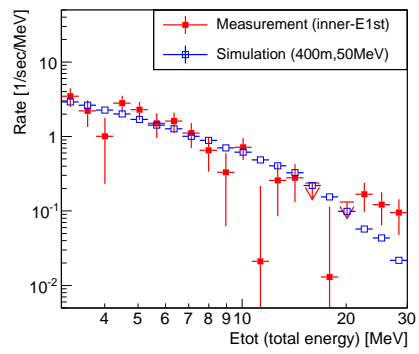
(f)

Figure 7.13: Same as Figure 7.12 but for burst20140718-1
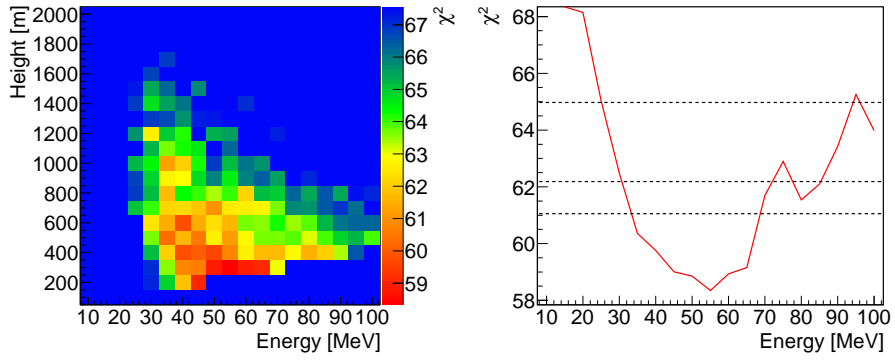
(a)

(b)
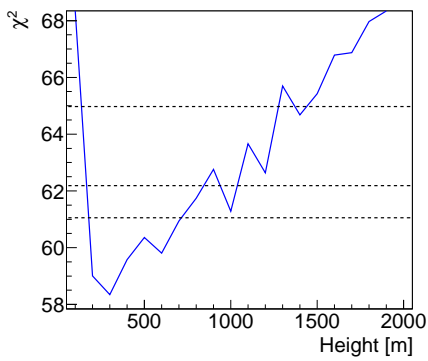
(c)
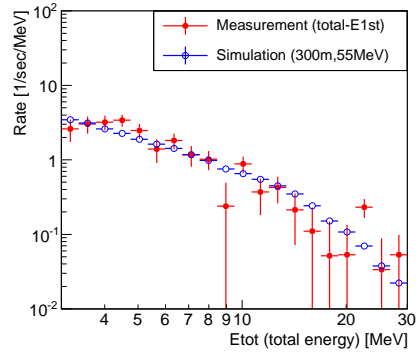
(d)
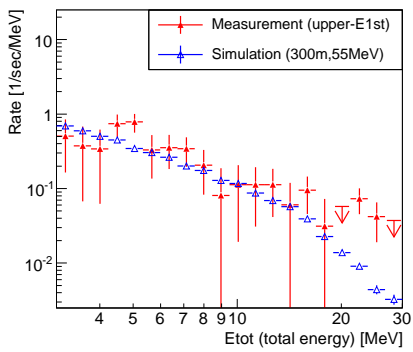
(e)
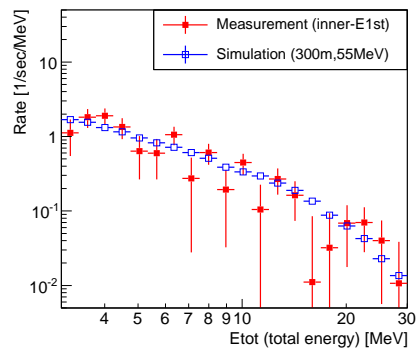
(f)

Figure 7.14: Same as Figure 7.12 but for burst20140719-1

99
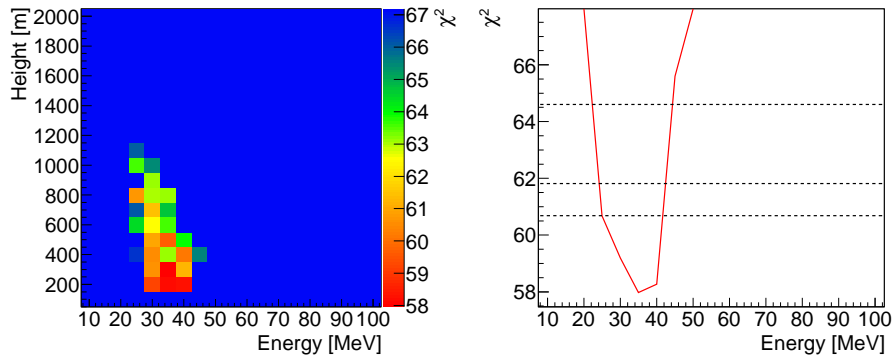
(a)

(b)
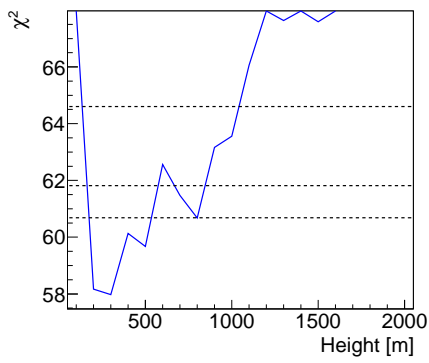
(c)
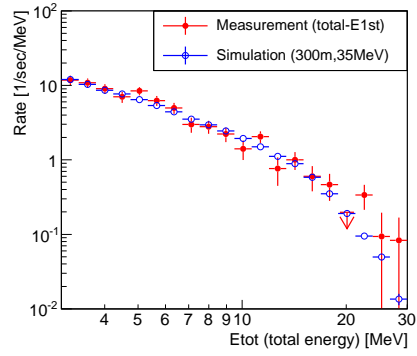
(d)
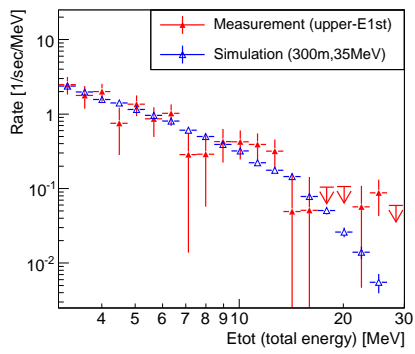
(e)
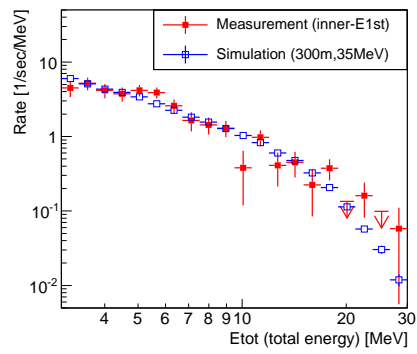
(f)

Figure 7.15: Same as Figure 7.12 but for burst20140731-1
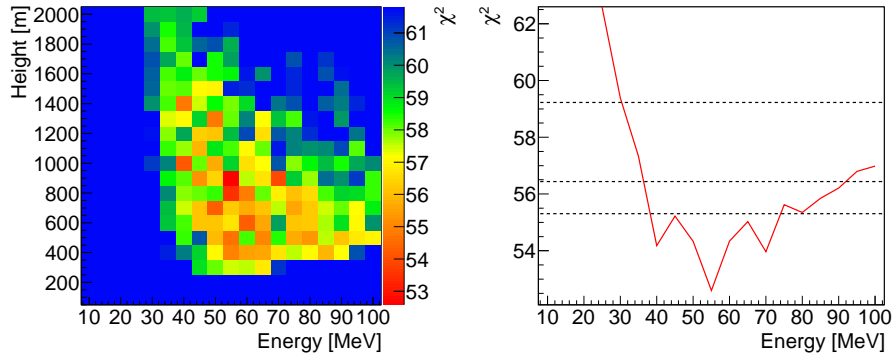
(a)

(b)
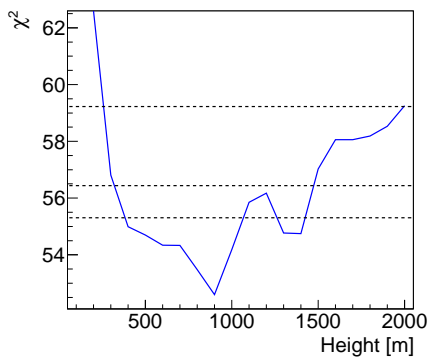
(c)
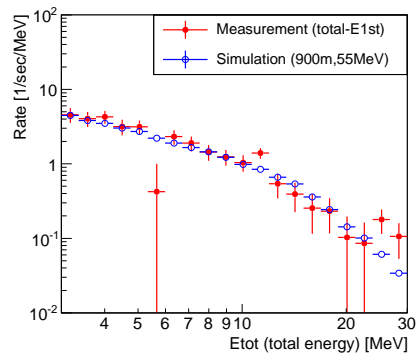
(d)
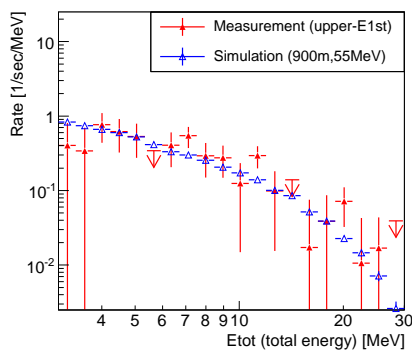
(e)
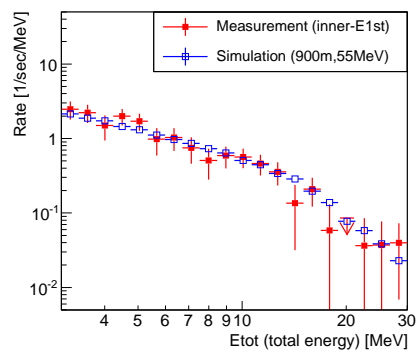
(f)

Figure 7.16: Same as Figure 7.12 but for burst20140822-1

101
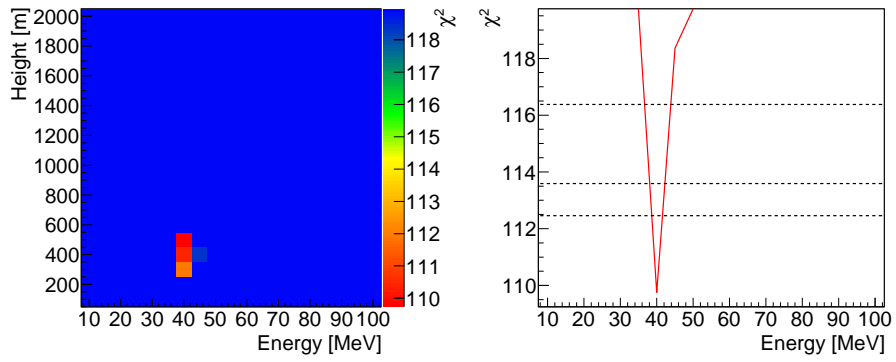
(a)

(b)
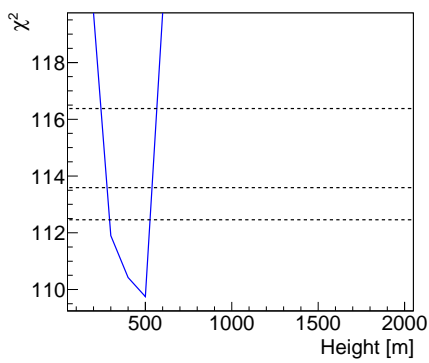
(c)
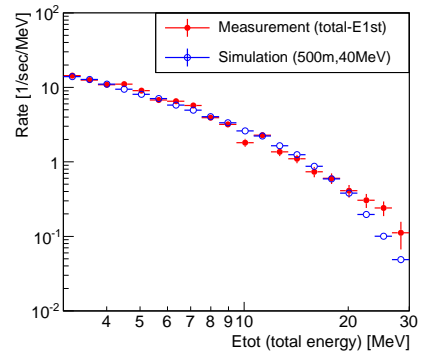
(d)
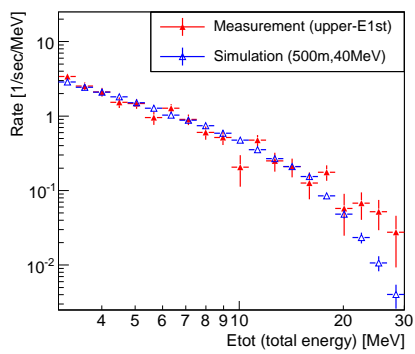
(e)
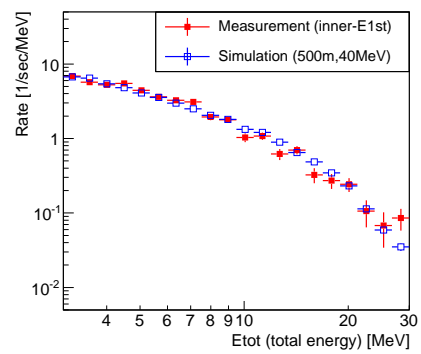
(f)

Figure 7.17: Same as Figure 7.12 but for burst20140823-1

102
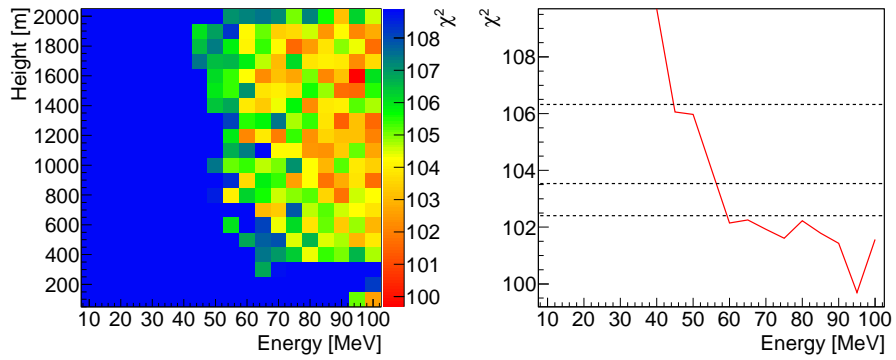
(a)

(b)
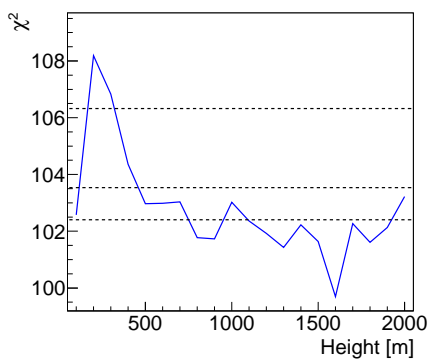
(c)
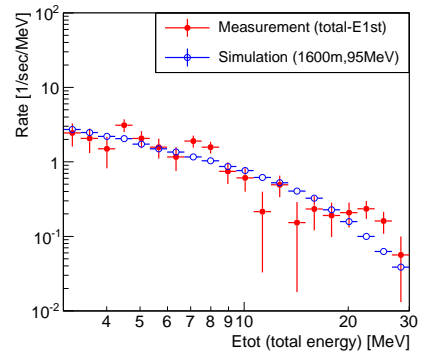
(d)
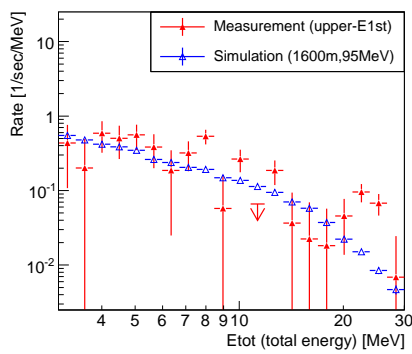
(e)
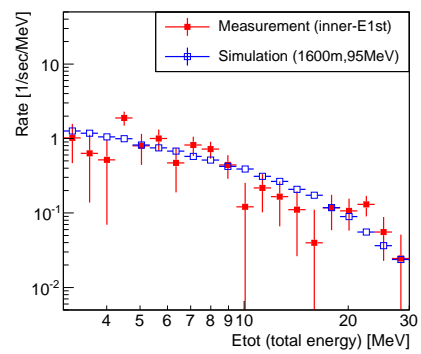
(f)

Figure 7.18: Same as Figure 7.12 but for burst20140826-1
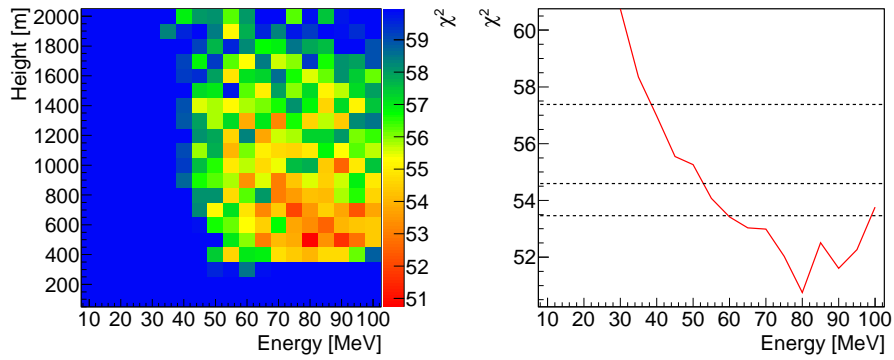
(a)

(b)
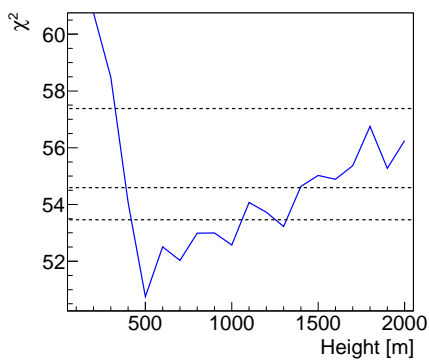
(c)
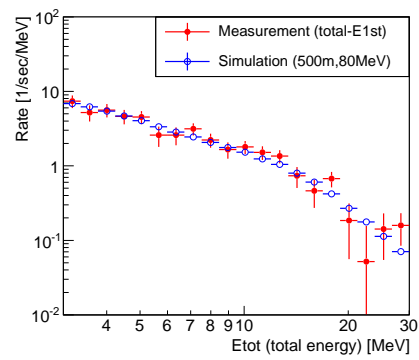
(d)
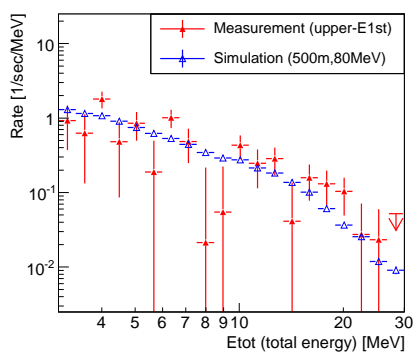
(e)
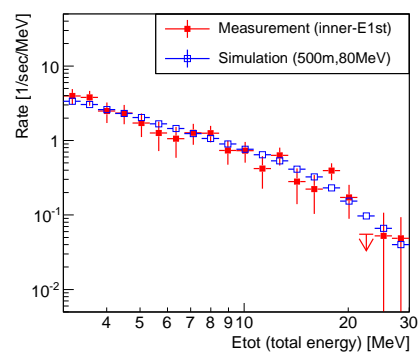
(f)

Figure 7.19: Same as Figure 7.12 but for burst20140830-1
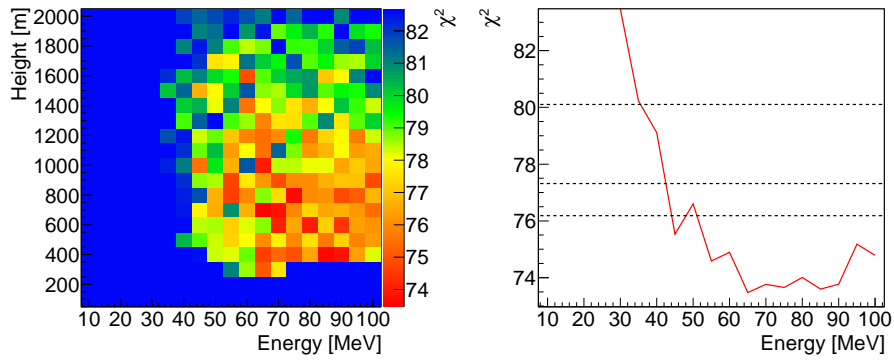
(a)

(b)
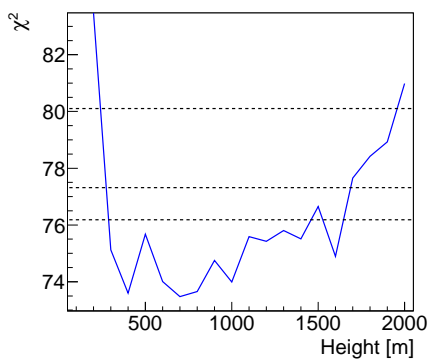
(c)
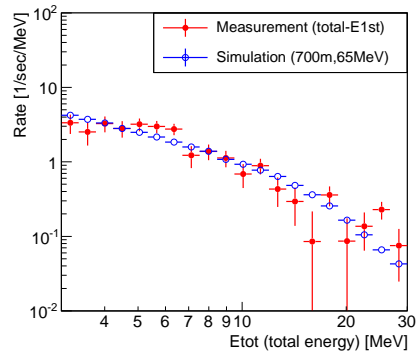
(d)
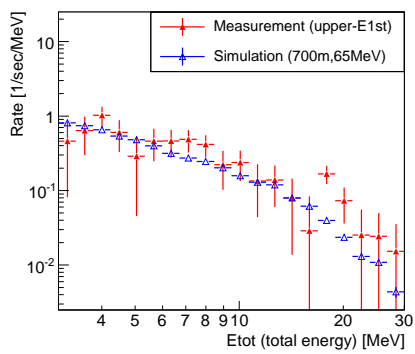
(e)
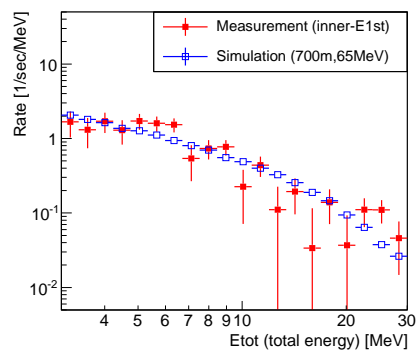
(f)

Figure 7.20: Same as Figure 7.12 but for burst20140830-2
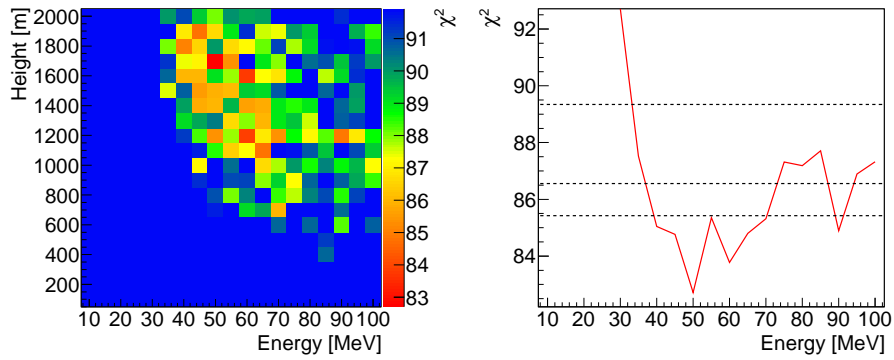
(a)

(b)
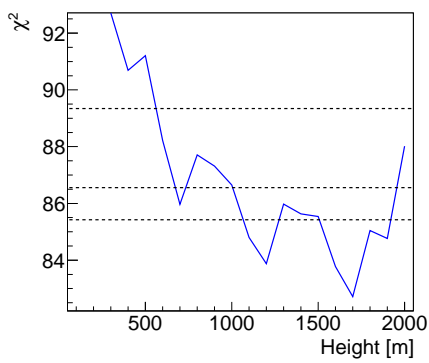
(c)
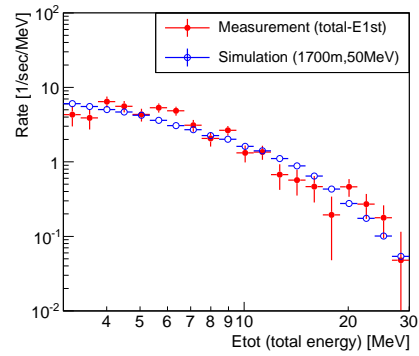
(d)
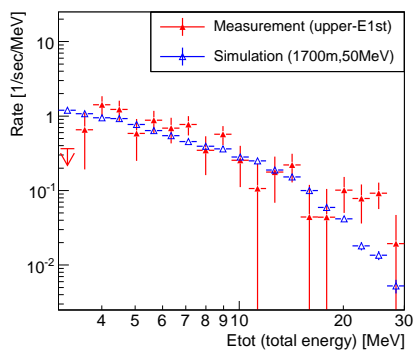
(e)
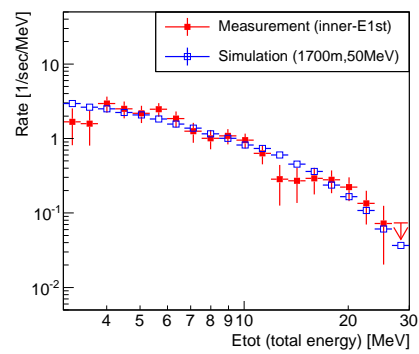
(f)

Figure 7.21: Same as Figure 7.12 but for burst20140905-1
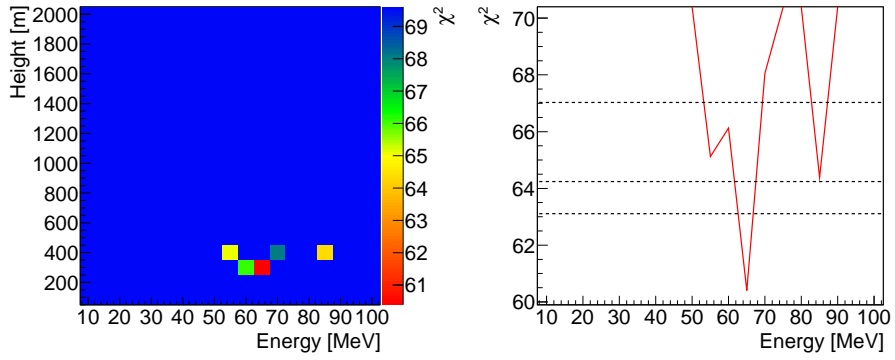
(a)

(b)
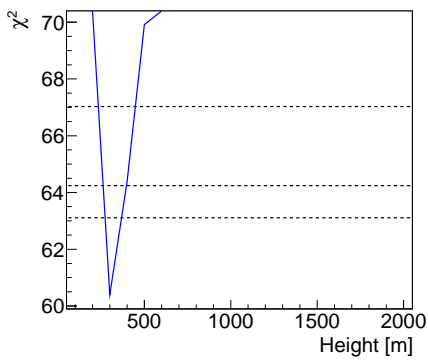
(c)
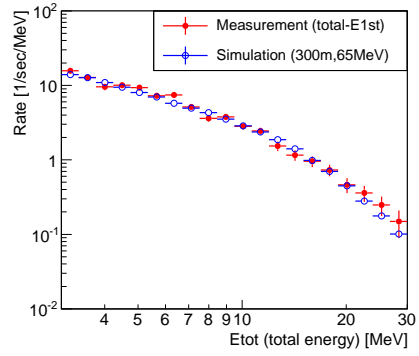
(d)
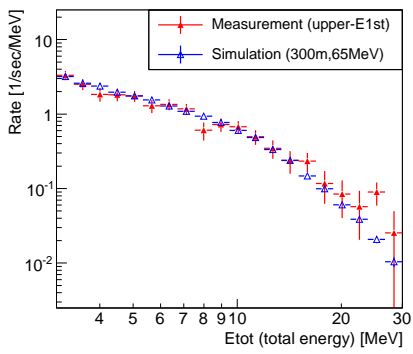
(e)
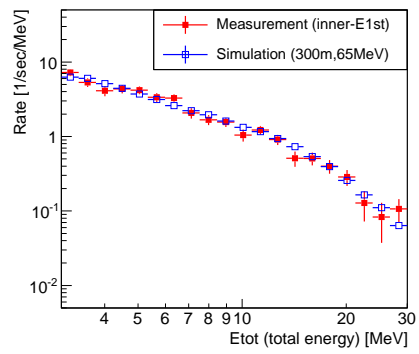
(f)

Figure 7.22: Same as Figure 7.12 but for burst20140905-2
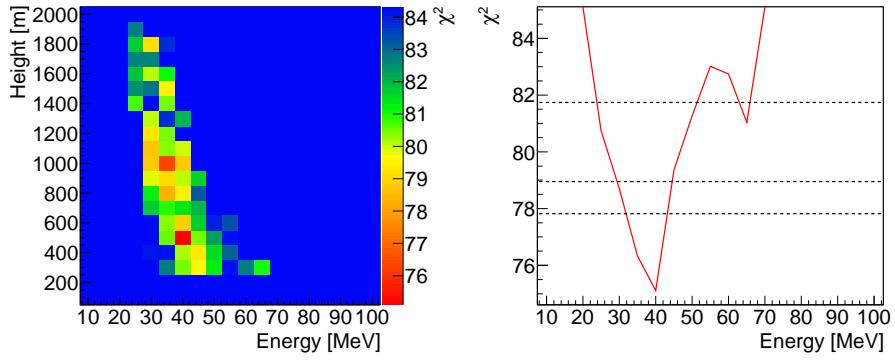
(a)

(b)
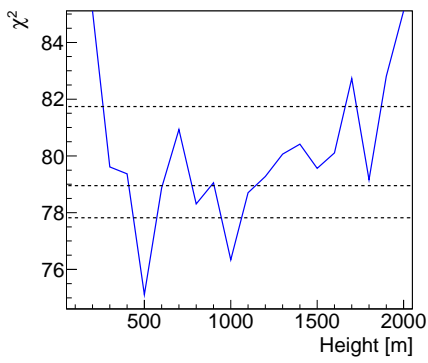
(c)
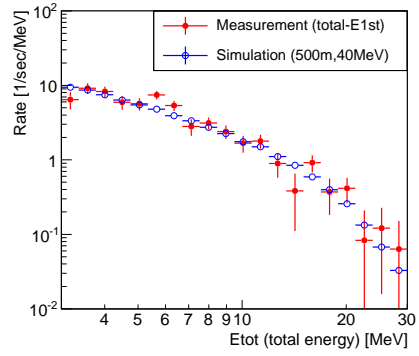
(d)
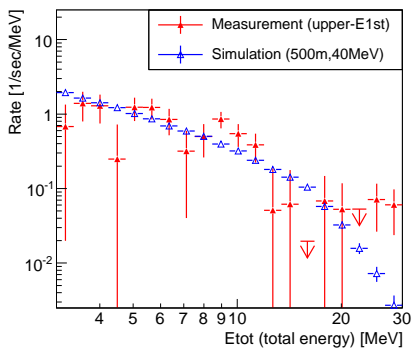
(e)
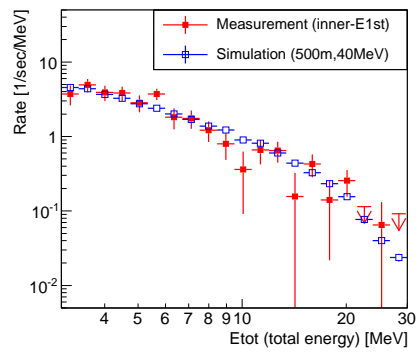
(f)

Figure 7.23: Same as Figure 7.12 but for burst20140905-3

shot to the ground surface was also common for both methods.

The estimated energy of runaway electron source of Ohi's bursts was 16 MeV for all three bursts. Since the minimum of estimated best fit energy of Norikura's 12 bursts was 35 MeV for burst20140731-1 (shown in Table 7.1), it was indicated that the runaway electrons at Norikura generally get higher energy in thundercloud acceleration region compared to those at Ohi. Even if 90 % confidence intervals of Norikura's bursts were taken into account, the lowest limit of 90 % C.L., 25 MeV for burst20140731-1, was higher than three bursts of Ohi.

By estimation of runaway electron sources considering the detector response, it was confirmed that the situation of electron acceleration in thunderclouds differed between Norikura and Ohi, which led to the difference of runaway electron energy. On the other hand, difference could not be found in estimated height of runaway electron sources between Norikura and Ohi.

Table 7.2: The most likely height and energy of runaway electron sources for three bursts observed at Ohi Power Station [2]

Burst	Best fit height	Best fit energy	χ^2/dof
20111225	1100 m	16 MeV	0.96
20120102	1100 m	16 MeV	0.87
20120105	400 m	16 MeV	0.82

7.4.4 Systematic error depending on angular distribution

As described in 7.2.1, runaway electrons were assumed to be vertical against the ground surface in the Monte Carlo simulation of electron propagation in the air. This assumption was common to the past simulation performed for Ohi's bursts [2]. However, we considered the systematic error of the vertical model for better estimation of runaway electron sources.

We performed another Monte Carlo simulation based on different assumption of zenith angular distribution. In this simulation, runaway electrons were shot downward with the angular distribution proportional to $\cos\theta$. It was a rather conservative assumption as described in 7.1.2. After the particles were collected at the ground surface after propagating in the

air, Monte Carlo simulation for detector response was performed in the same manner as the vertical assumption.

The best fit results of runaway electron sources obtained from two angular distribution models are listed in Table 7.3. To figure out the systematic error regarding the angular distribution model, the difference of best fit results of $\cos\theta$ model and vertical model were plotted in Figure 7.24 against the statistical significance of bursts shown in Table 6.2.

The result indicated that larger statistical significance led to smaller systematic error of angular distribution model for both height and energy. Especially two strong bursts, burst20140823-1 and burst20140905-2, seemed to have small systematic error. Here we assumed that these two bursts had model-dependent systematic errors of 100 m for height and 20 % for energy, while other 10 bursts had errors of 1000 m for height and +100 % / −40 % for energy. Under this assumption, the best fit energy of runaway electron sources of Norikura's bursts were still higher than Ohi's bursts, whereas it turned out to be difficult to restrict the height of runaway electron sources especially for statistically small bursts.

Table 7.3: Best fit results of runaway electron sources obtained from vertical model and $\cos\theta$ proportional model

Burst	Best fit height		Best fit energy	
	vertical	$\cos\theta$	vertical	$\cos\theta$
20140708-1	1100 m	700 m	65 MeV	95 MeV
20140718-1	400 m	400 m	50 MeV	90 MeV
20140719-1	300 m	300 m	55 MeV	60 MeV
20140731-1	300 m	300 m	35 MeV	30 MeV
20140822-1	900 m	900 m	55 MeV	45 MeV
20140823-1	500 m	400 m	40 MeV	45 MeV
20140826-1	1600 m	900 m	95 MeV	85 MeV
20140830-1	500 m	900 m	80 MeV	65 MeV
20140830-2	700 m	800 m	65 MeV	60 MeV
20140905-1	1700 m	1600 m	50 MeV	80 MeV
20140905-2	300 m	300 m	65 MeV	65 MeV
20140905-3	500 m	1300 m	40 MeV	30 MeV
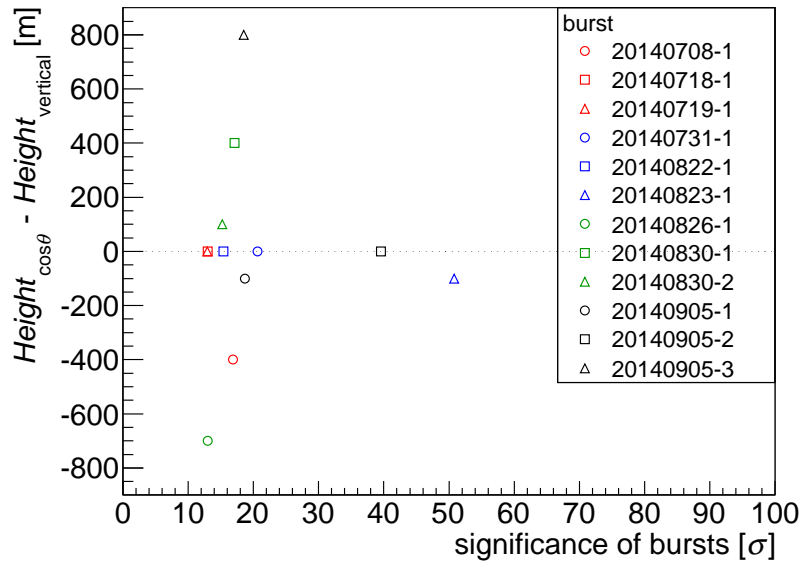
(a) height
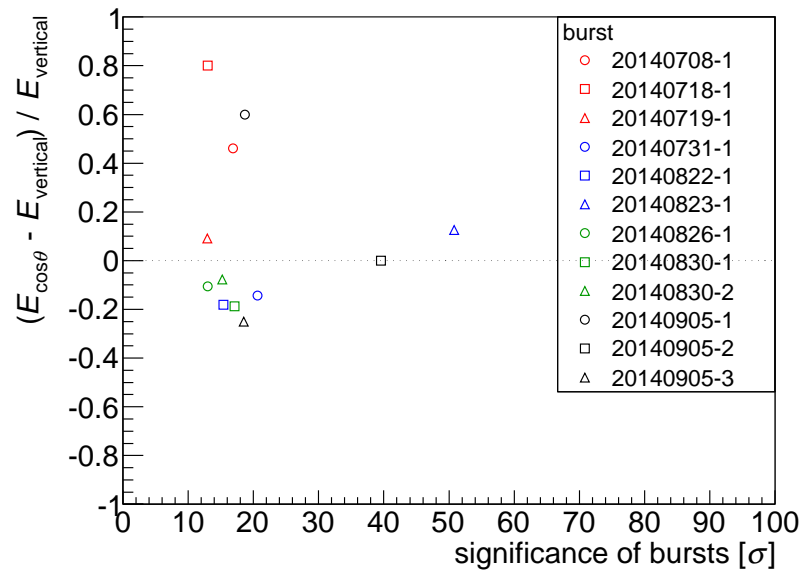
(b) energy

Figure 7.24: Difference of the best fit results of two angular distribution models (vertical and cosθ proportional) against statistical significance of bursts; (a) Difference of height; (b) Differential rate of energy

Chapter 8

Particle components of bursts

8.1 Electron in radiation bursts

It would be important to evaluate the electron component included in thundercloud radiation busts in order to discuss the distance of runaway electron sources as described in 1.3.1. In this section, we estimated the electron component of observed bursts using several analytical approaches.

8.1.1 Range of runaway electrons in the air

Tsuchiya *et al.* reported that electrons were detected simultaneously with gamma-rays during a thunderstorm at Norikura Observatory [35]. Utilizing the energy spectrum of gamma-rays, they estimated the source position of the burst to be at approximately 90 m above the ground.

The range of electrons are 64 m (10 MeV), 109 m (20 MeV), 175 m (40 MeV) and 288 m (100 MeV) at the altitude of Norikura Observatory (2,770 m, 0.72 hPa). In addition, electrons incident on the detector from upward direction have to go through aluminum plates of 6 mm in total (4 mm for the cover of the detector and 2 mm for the ceiling of the van), which is equivalent to the air of 20 - 25 m thickness at 2,770 m. Consequently, the actual electron range upward from the detector is 44 - 263 m for 10 - 100 MeV electrons.

8.1.2 Electron ratio at the most likely runaway electron source

The electron ratio of simulated bursts (Figure 7.6) shows that electrons become dominant only when the source height is 100 m and the energy is higher than 25 MeV. In other cases, gamma-rays become dominant.

As described in 7.4.2, 12 bursts observed by PANDA64 at Norikura Observatory were likely to be generated by the runaway electron sources of higher than 200 m above the detector. The electron-dominant range, i.e. ($h = 100$ m, $E_e \geq 25$ MeV), were out of 90 % confidence region in most bursts. The electron ratio at the best fit height and energy are shown in Table 8.1. The highest electron ratio was 0.21 for burst20140905-2, while it was less than 0.1 for other 11 bursts. Therefore, all bursts observed at Norikura were expected to be gamma-ray-dominant bursts.

Table 8.1: Simulated electron ratio at the best fit results of runaway electron sources

Burst	Best fit		Electron ratio
	height	energy	(simulated)
20140708-1	1100 m	65 MeV	0.04
20140718-1	400 m	50 MeV	0.03
20140719-1	300 m	55 MeV	0.06
20140731-1	300 m	35 MeV	0.02
20140822-1	900 m	55 MeV	0.04
20140823-1	500 m	40 MeV	0.03
20140826-1	1600 m	95 MeV	0.05
20140830-1	500 m	80 MeV	0.04
20140830-2	700 m	65 MeV	0.04
20140905-1	1700 m	50 MeV	0.04
20140905-2	300 m	65 MeV	0.21
20140905-3	500 m	40 MeV	0.03

8.1.3 E_{1st} distribution and temporal variation

As the next step, the electron component included in radiation bursts was investigated by taking advantage of E_{1st} distribution. 30-second temporal variation of count rates of total-E_{1st}, upper-E_{1st} and inner-E_{1st} (defined in 7.3.2) were plotted for all 12 bursts in Figure 8.1 - 8.4. The ratio of

upper-E_{1st} and inner-E_{1st} was also calculated in order to know the temporal variation of E_{1st} distribution.

In Figure 8.5, the simulated distribution of E_{1st} are shown when gamma-rays and electrons of 20 MeV were shot from a flat surface above the detector. Most of incident electrons from upward direction deposited their energy intensively at 8 modules of the top stage and E_{1st} distribution certainly concentrated on those modules. This result was in good agreement with a range of 8.3 cm of 20 MeV electron in plastic scintillator (1.032 g/cm^3, vinyltoluene based). In contrast, E_{1st} of gamma-rays from upward direction distributed relatively homogeneous on all modules compared to electrons.

The ratio of upper-E_{1st} and inner-E_{1st} would therefore increase if electrons were dominantly included in the bursts. However, the temporal variation showed no significant increase of the ratio of upper-E_{1st} and inner-E_{1st} during all burst periods, although the count rates of both inner-E_{1st} and upper-E_{1st} showed simultaneous enhancement.

On the other hand, E_{1st} distribution of observed bursts are shown in Figure 8.6. In the figure, the events of $E_{tot} > 3$ MeV were plotted after subtraction of the background period. The scale of the color bar was set as same as Figure 8.5 to compare with it. Although the plots seemed to be somewhat uneven because of the lack of statistics, we could see that no module on the top stage had more than 10 % of the total counts in contrast with the electron simulation shown in Figure 8.5.

8.1.4 Electron ratio of observed bursts

In order to investigate the electron ratio included in radiation bursts quantitatively, further simulation were performed by injecting gamma-rays and electrons of 10, 20, 50 and 100 MeV toward PANDA64. The ratio of upper-E_{1st} and inner-E_{1st} ($UIratio$) corresponding to each incident particles are shown in Table 8.2.

$UIratio$ values of 12 bursts observed at Norikura Observatory were also calculated after subtracting the background period from the burst period. Calculated $UIratio$ were listed in Table 8.3, which varied from 0.335 (burst20140822-1) to 0.527 (burst20140718-1).

114
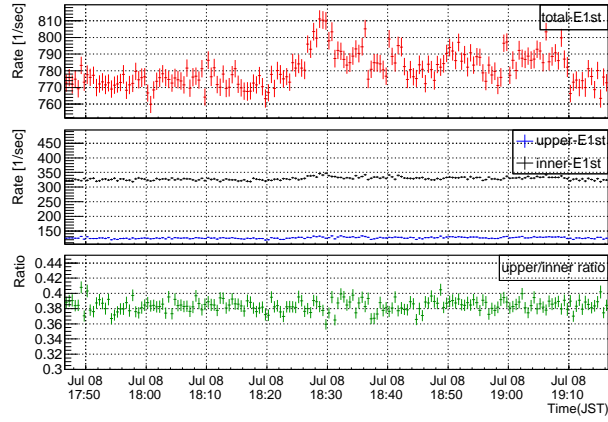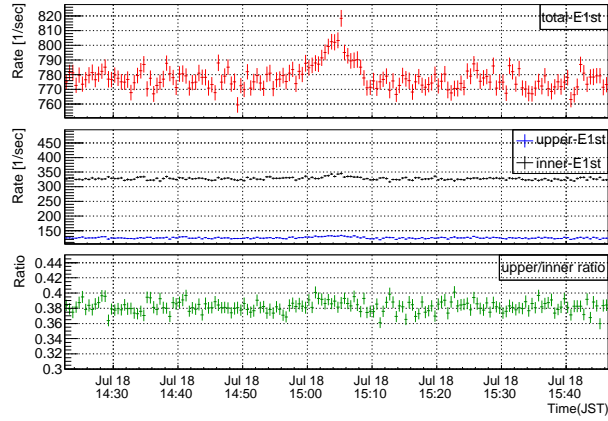
(a) burst20140708-1
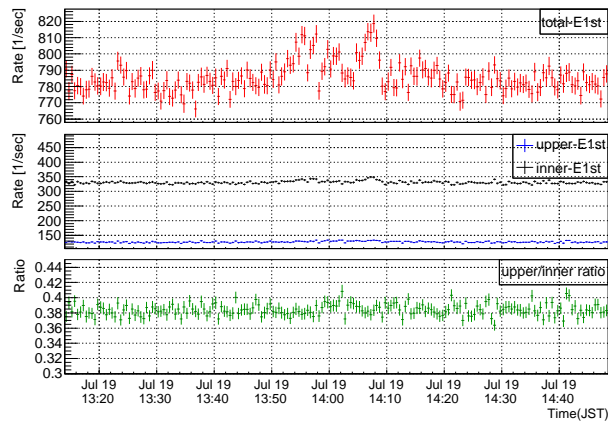
(b) burst20140718-1

(c) burst20140719-1

Figure 8.1: 30-second temporal variation of total-E_{1st} (red), upper-E_{1st} (blue) and inner-E_{1st} (black) count rate along with the ratio of upper-E_{1st} and inner-E_{1st} (green) around burst20140708-1, burst20140718-1 and burst20140719-1

115
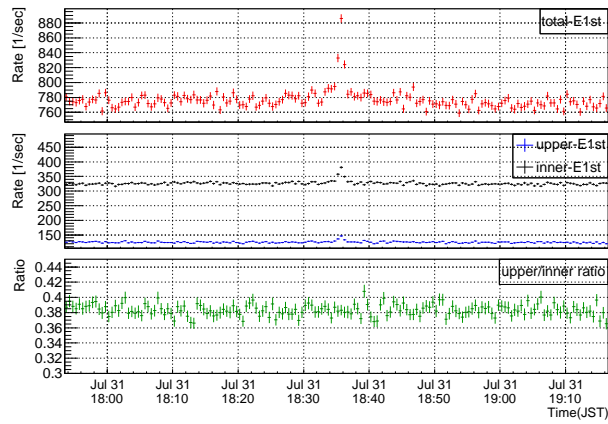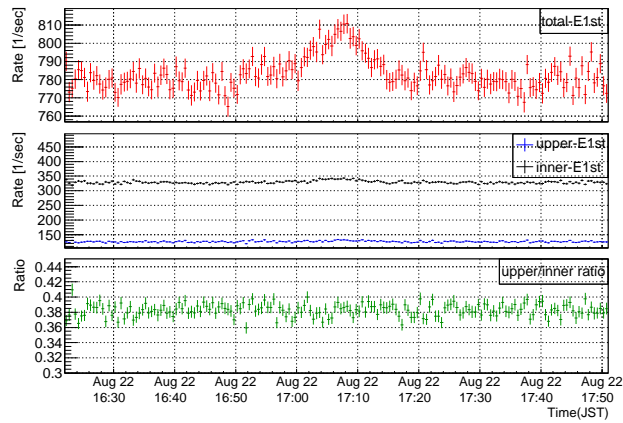
(a) burst20140731-1
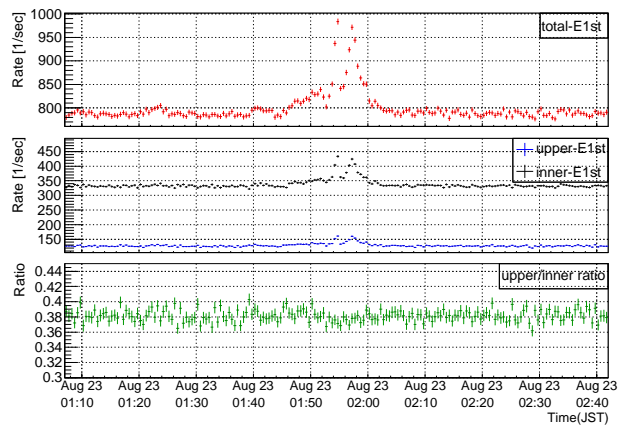
(b) burst20140822-1

(c) burst20140823-1

Figure 8.2: Same as Figure 8.1 but for burst20140731-1, burst20140822-1 and burst20140823-1
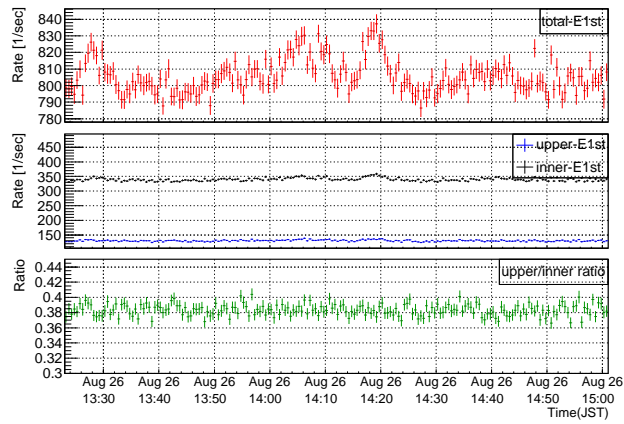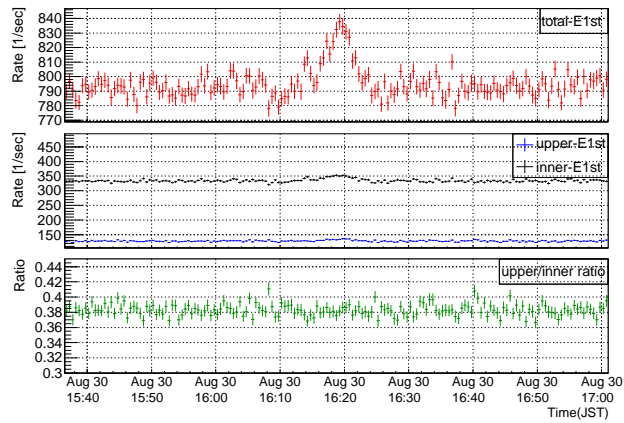
(a) burst20140826-1
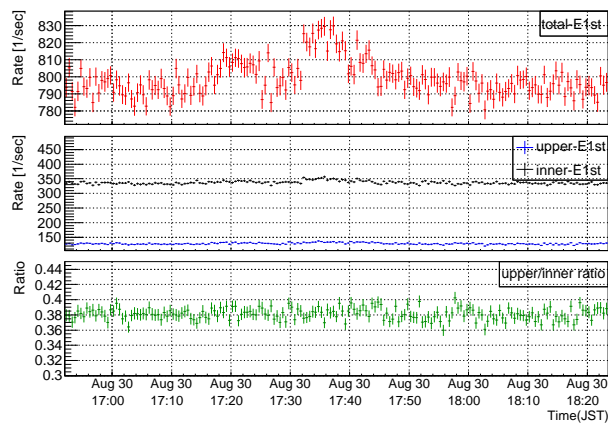
(b) burst20140830-1

(c) burst20140830-2

Figure 8.3: Same as Figure 8.1 but for burst20140826-1, burst20140830-1 and burst20140830-2
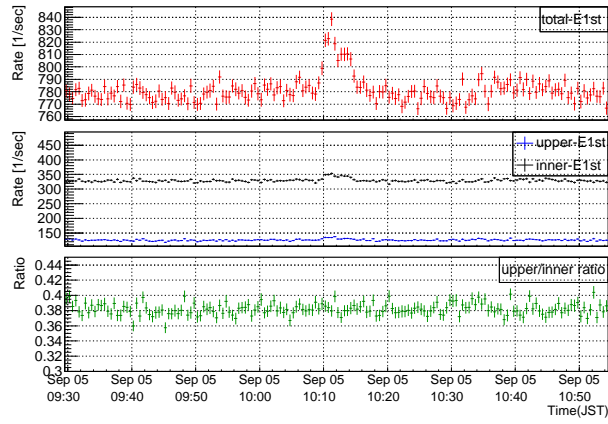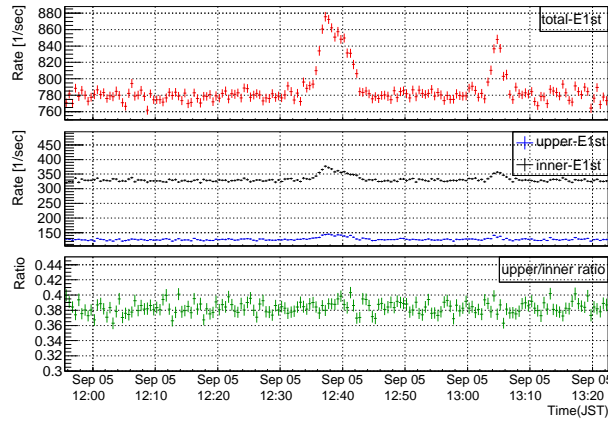
(a) burst20140905-1
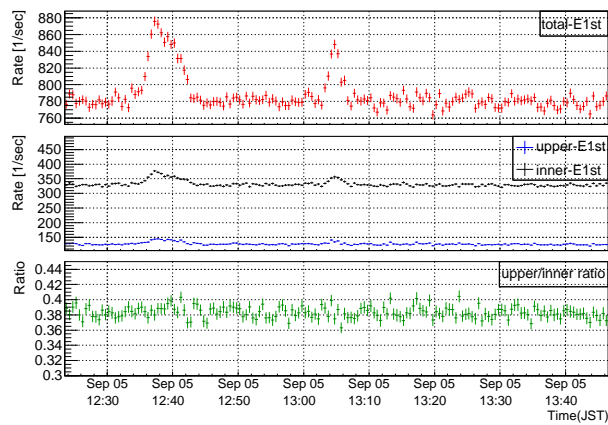
(b) burst20140905-2

(c) burst20140905-3

Figure 8.4: Same as Figure 8.1 but for burst20140905-1, burst20140905-2 and burst20140905-3
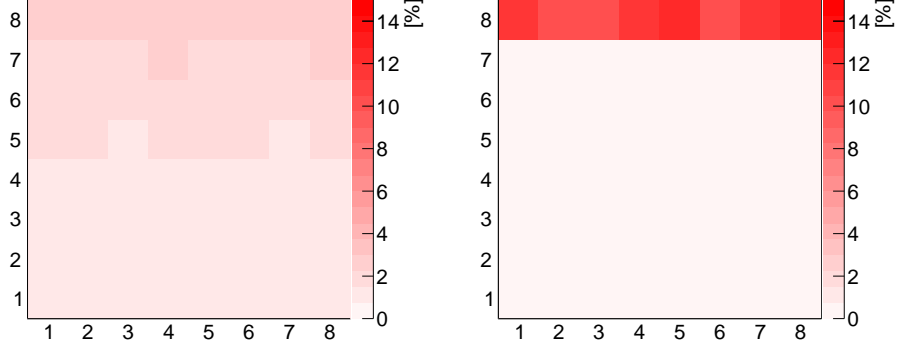
Figure 8.5: Simulated distribution of E_{1st} modules obtained from Monte Carlo simulation of monochromatic particles shot vertically downward to the detector: (left) 20 MeV gamma-rays : (right) 20 MeV electrons

Utilizing obtained $UIratio$, the electron ratio at the injection surface was calculated for each monochromatic energy of gamma-rays and electrons. The electron ratio $d = e^-/(\gamma + e^-)$ could be obtained from the equation below.

$$UIratio_{burst} = \frac{(1-d) \times upper_{\gamma} + d \times upper_{e^-}}{(1-d) \times inner_{\gamma} + d \times inner_{e^-}}, \tag{8.1}$$

where $upper$ and $inner$ are the counts of upper-E_{1st} and inner-E_{1st} events detected by PANDA64 per an incident particle of simulation.

Electron ratios calculated assuming monochromatic gamma-rays and electrons of 10, 20, 50 and 100 MeV were also shown in Table 8.3. The electron ratios were below 0.3 for all combinations of 12 bursts and four monochromatic energies. The maximum electron ratio was $d = 0.29$ for burst20140718-1 at 100 MeV gamma-rays and electrons. In this case, the upper limit of electron ratio was $d = 0.43$ (95 % confidence level). Thus, we concluded that all 12 bursts observed at Norikura Observatory were gamma-ray-dominant bursts.

(a) burst20140708-1 (b) burst20140718-1 (c) burst20140719-1

(d) burst20140731-1 (e) burst20140822-1 (f) burst20140823-1

(g) burst20140826-1 (h) burst20140830-1 (i) burst20140830-2

(j) burst20140905-1 (k) burst20140905-2 (l) burst20140905-3
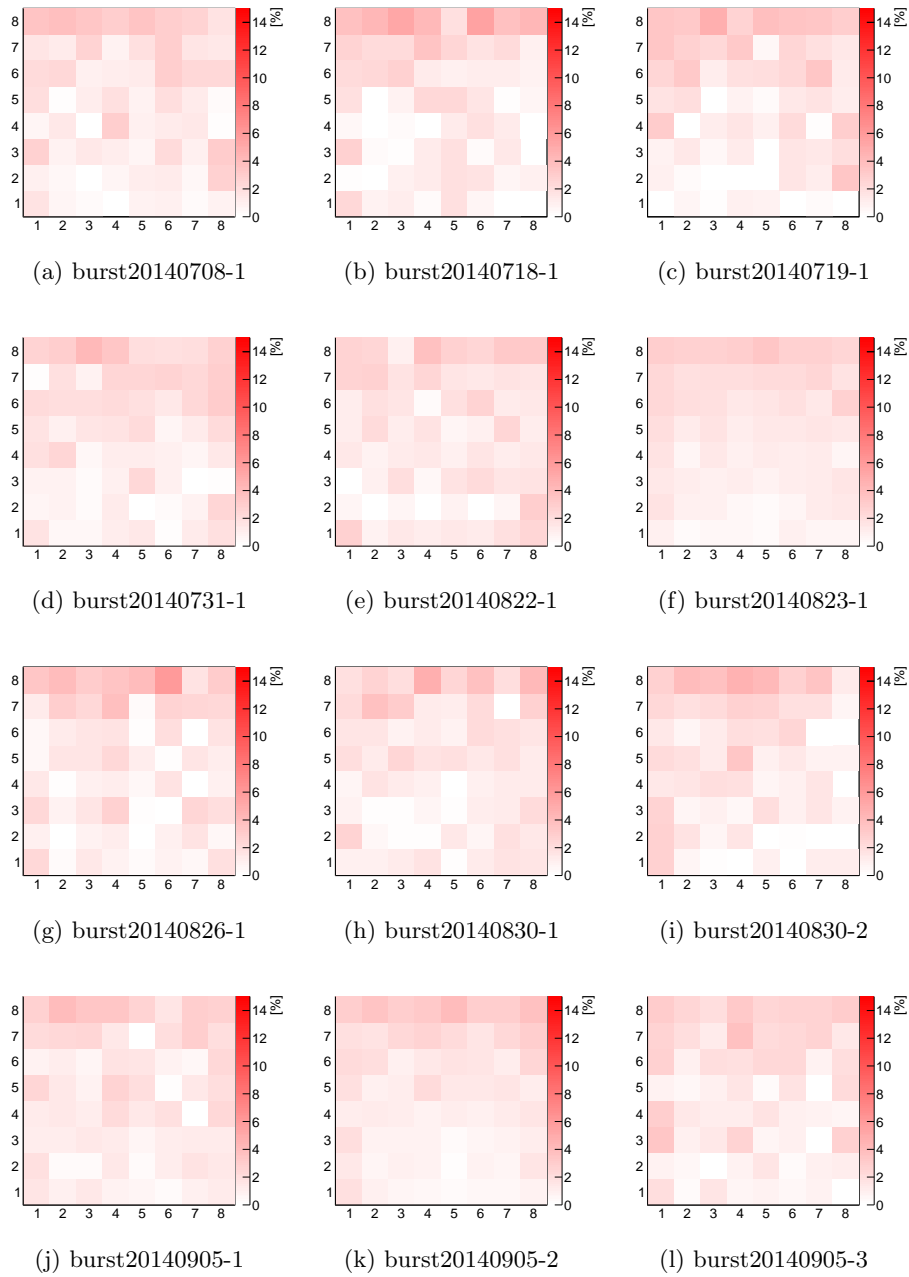
Figure 8.6: Distribution [%] of E_{1st} modules obtained from measurement data of 12 observed bursts

Table 8.2: Simulated ratio of upper-E_{1st} and inner-E_{1st} ($UIratio$) obtained from monochromatic gamma-rays and electrons

Energy	gamma-ray $UIratio$	electron $UIratio$
10 MeV	0.302	20.8
20 MeV	0.282	11.3
50 MeV	0.233	2.47
100 MeV	0.162	1.41

Table 8.3: Ratio of upper-E_{1st} and inner-E_{1st} ($UIratio$) and electron ratio corresponding to four monochromatic energies

Burst	$UIratio$ (BG subtracted)	Electron ratio			
		10 MeV	20 MeV	50 MeV	100 MeV
20140708-1	0.396 ± 0.058	0.12	0.07	0.11	0.19
20140718-1	0.527 ± 0.086	0.25	0.14	0.19	0.29
20140719-1	0.458 ± 0.081	0.19	0.10	0.15	0.24
20140731-1	0.342 ± 0.046	0.06	0.04	0.08	0.14
20140822-1	0.335 ± 0.062	0.05	0.03	0.07	0.14
20140823-1	0.354 ± 0.018	0.07	0.04	0.08	0.15
20140826-1	0.481 ± 0.084	0.21	0.12	0.17	0.26
20140830-1	0.382 ± 0.060	0.11	0.06	0.10	0.18
20140830-2	0.429 ± 0.061	0.16	0.09	0.13	0.21
20140905-1	0.380 ± 0.054	0.10	0.06	0.10	0.17
20140905-2	0.434 ± 0.027	0.16	0.09	0.14	0.22
20140905-3	0.338 ± 0.052	0.05	0.04	0.07	0.14

8.2 Neutron in radiation bursts

As described in 1.3.2, radiation bursts related to thunderclouds might produce neutrons. Thus we investigated whether the neutron component was included in thundercloud radiation bursts observed at Norikura Observatory.

8.2.1 Delayed coincidence for neutron detection

It is suggested that the photonuclear reaction produces neutrons in thunderclouds. Actually some previous experiments detected neutron signal enhancements by neutron counters during radiation bursts. PANDA36 also detected neutrons of 14 ± 5 events per second by delayed coincidence method in one of three bursts observed at Ohi Power Station [2].

A neutron incident on PANDA64 produces two signals within a short time interval. The prompt signal is attributed to proton recoils by the incident neutron, while the delayed signal is caused by the neutron capture by gadolinium. Because thermalization of neutrons takes tens of microseconds in the detector, the two signals can be detected by delayed coincidence.

8.2.2 Selection cuts for delayed coincidence

In order to decide the selection cuts for delayed coincidence, a Monte Carlo simulation was performed by injecting neutrons isotropically toward the detector. Four monochromatic energies (10, 20, 50 and 100 MeV) were tested as the incident neutron energy. Prompt energy (E_{prompt}) spectrum, delayed energy (E_{delayed}) spectrum and the time difference between prompt and delayed events (ΔT) for each neutron energy are shown in Figure 8.7.

First of all, the lower cut of E_{prompt} and E_{delayed} was set to 3 MeV in order to exclude the effect of rain fallout. Although E_{prompt} spectrum seemed to be different depending on the incident neutron energy, we set the higher cut of E_{prompt} as 30 MeV because 99 % of prompt events above $E_{\mathrm{tot}} > 3$ MeV would survive against this upper cut even in the case of 100 MeV neutrons. On the other hand, E_{delayed} spectra did not differ among incident neutron energies because delayed events are mainly invoked by 8 MeV gamma-rays emitted via neutron capture by gadolinium. Therefore, the cut of E_{delayed}

was set to 3 - 8 MeV, whose detection efficiency was 99 % for the events above 3 MeV.

The time difference ΔT also seemed not to depend on neutron energy. Since wider ΔT cut leads to worse S/N due to increasing accidental events, the cut for ΔT was set between 8 μs and 150 μs. The lower cut (8 μs) was attributed to the ADC conversion time of approximately 7.5 μs. The higher cut (150 μs) corresponded to the detection efficiency of 90 % for events of $\Delta T > 8\mu$s. The selection cuts for delayed events are shown in Table 8.4.

Firstly, an event which had E_{tot} of 3 - 30 MeV was tagged as a prompt event, and then a delayed event corresponding to the prompt event was searched between the time window of 8 - 150 μs. E_{tot} of delayed events had to be 3 - 8 MeV. If a delayed event was found in the time window, the pair of prompt and delayed events was counted as a correlated event.

Correlated events obtained from measurement data include pairs of two events which were detected accidentally in the time window. To reject such accidental backgrounds, 1 ms-shifted time window, 1008 - 1150 μs, was introduced and the count rate of events detected in this time window was subtracted from the count rate of correlated events. Through this calculation, the count rate of correlated events could be obtained from the measurement data.

Table 8.4: Selection cuts of delayed coincidence for neutron detection

Cuts	Correlated events	Accidental events
prompt event	$3\text{MeV} < E_{tot} < 30$ MeV	
delayed event	$3\text{MeV} < E_{tot} < 8\text{MeV}$	
time window	$8\mu\text{s} < \Delta T < 150~\mu$s	$1008\mu\text{s} < \Delta T < 1150~\mu$s

8.2.3 Temporal variation of correlated event rate

30-second temporal variation of correlated event rate after subtraction of accidental event rate were plotted for 12 bursts and shown in Figure 8.8 - 8.11. In addition, stability of the count rate of cosmic ray muons which penetrated through PANDA64 was investigated because correlated event rate could be affected by muon spallation around the detector. Penetrating

(a) 10MeV, E_{prompt}

(b) 10MeV, E_{delayed}

(c) 10MeV, ΔT

(d) 20MeV, E_{prompt}

(e) 20MeV, E_{delayed}

(f) 20MeV, ΔT

(g) 50MeV, E_{prompt}

(h) 50MeV, E_{delayed}

(i) 50MeV, ΔT

(j) 100MeV, E_{prompt}

(k) 100MeV, E_{delayed}

(l) 100MeV, ΔT
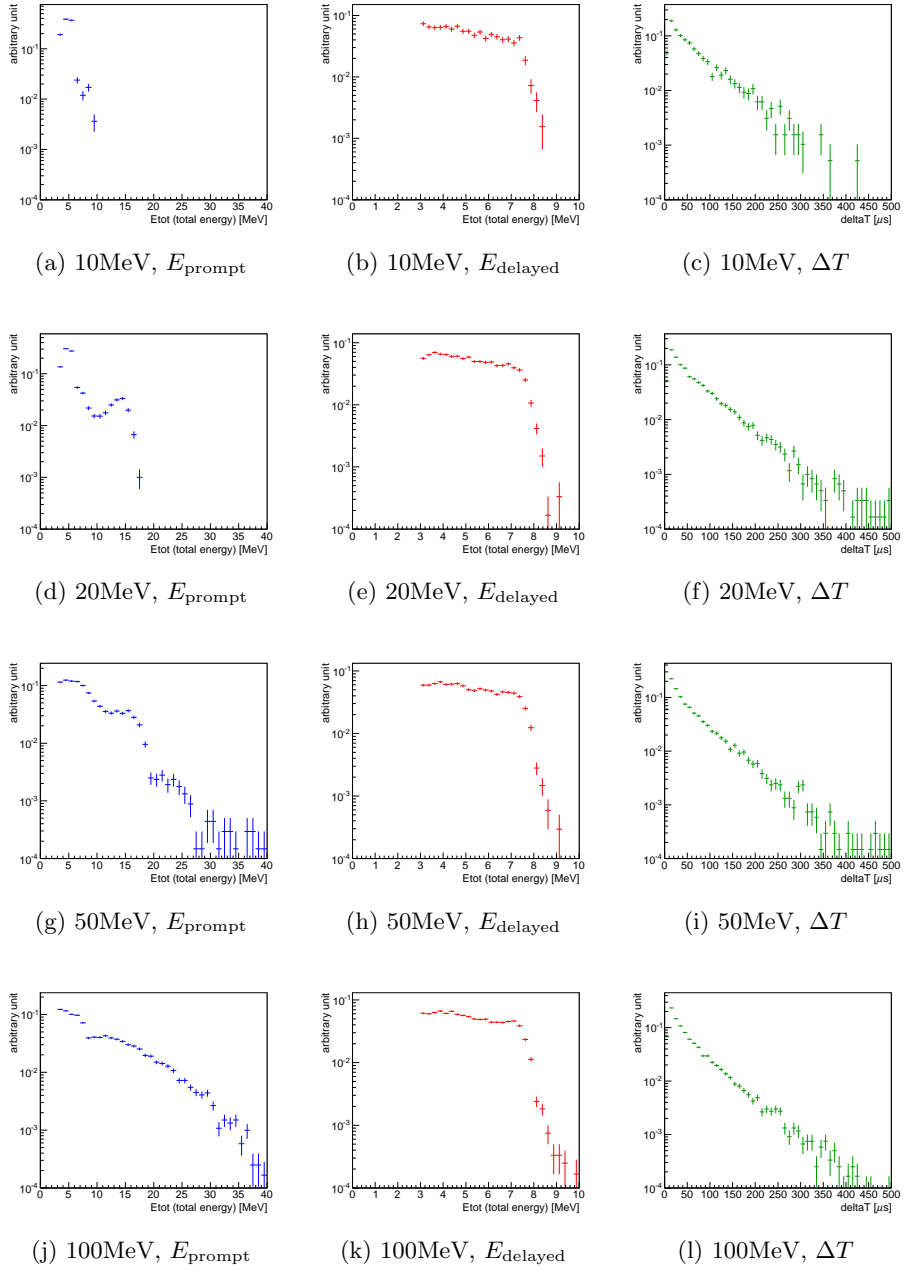
Figure 8.7: Simulated E_{tot} spectra of prompt events (E_{prompt}) and delayed events (E_{delayed}) and coincidence time (ΔT) obtained from Monte Carlo simulation of homogeneously and isotropically incident monochromatic neutrons of 10 MeV, 20 MeV, 50 MeV and 100 MeV.

muons were defined as events which at least one module on each stage of PANDA64 had energy deposit of > 5 MeV. 30-second temporal variation of penetrating muon rate was plotted in the figures along with the correlated event rate.

However, no significant enhancement of correlated event rate was observed in 12 observed bursts. Besides, the count rate of cosmic ray muons seemed to be stable during each burst period.

8.2.4   Upper limit of neutron flux during bursts

In order to investigate quantitatively the neutron flux related to radiation bursts, a Monte Carlo simulation was performed using Geant4 by injecting monochromatic neutrons toward PANDA64. In the simulation, neutrons of 10, 20, 50 and 100 MeV were shot isotropically or vertically to the detector. The detection efficiency of neutrons in each case is shown in Table 8.5. As there was not a big difference between two shooting directions, the detection efficiency of isotropic neutrons were utilized for the calculation below.

Correlated event rate (accidental event rate subtracted) during the burst period was calculated by subtraction of the background period. As shown in Table 8.6, all 12 bursts did not show significant enhancement of correlated event rate.

On the other hand, correlated event rate became negative value in some bursts, especially in burst20140719-1 (2.4σ). Although a possibility could be considered that there was a neutron signal enhancement in the background period, the reason could not be identified. In the cases of negative correlated event rates, the upper limits of confidence intervals shown in Table 8.6 were calculated based on the assumption that the count rate was 0 [/sec] in order to obtain conservative limits.

Subsequently, the upper limit of neutron flux around the detector was calculated utilizing the simulated detection efficiency. The upper limits of 95 % confidence intervals are listed in Table 8.7. The maximum value of the calculated upper limits, 102.9 [/sec/m^2], corresponded to the case that burst20140905-3 was assumed to be accompanied by 10 MeV monochromatic neutrons.
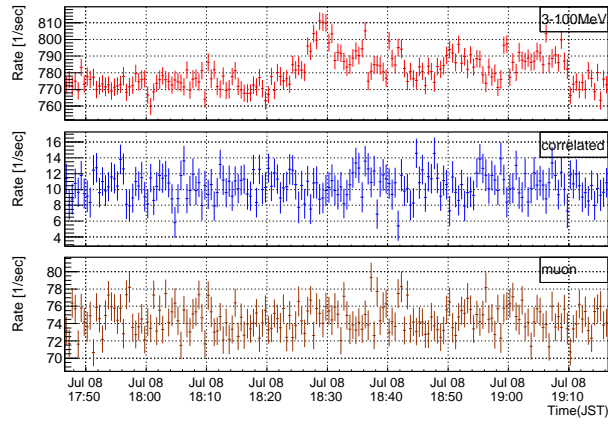
(a) burst20140708-1
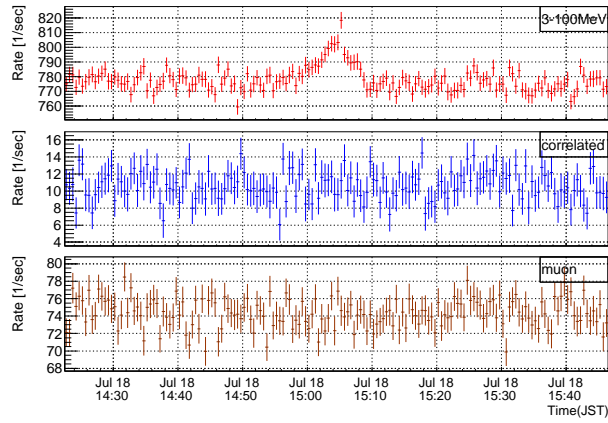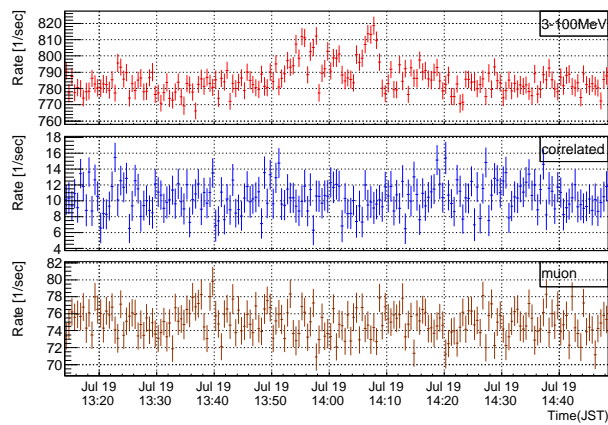
(b) burst20140718-1

(c) burst20140719-1

Figure 8.8:   30-second temporal variation of count rate around burst20140708-1, burst20140718-1 and burst20140719-1; 3 - 100 MeV events (red), correlated events (blue) and penetrating muon events (brown)

126
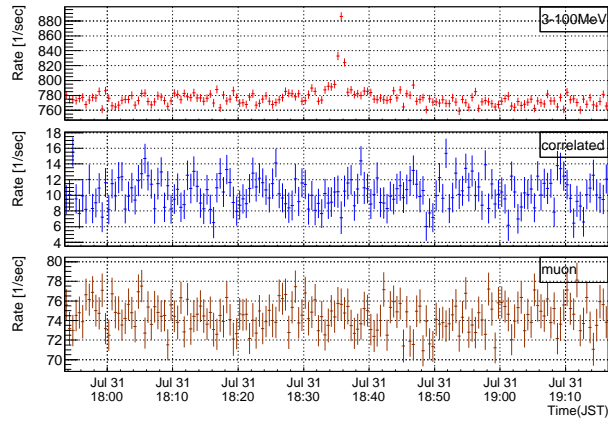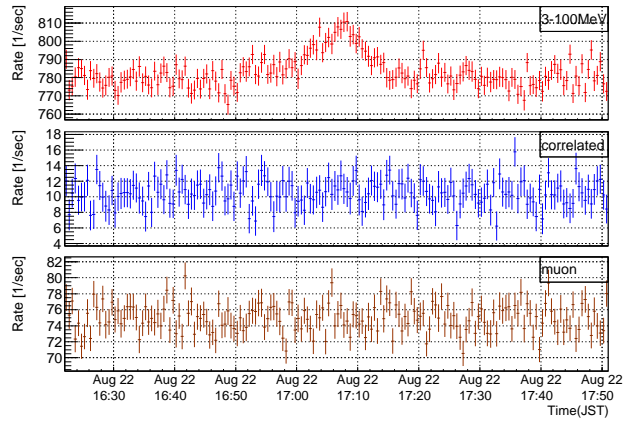
(a) burst20140731-1
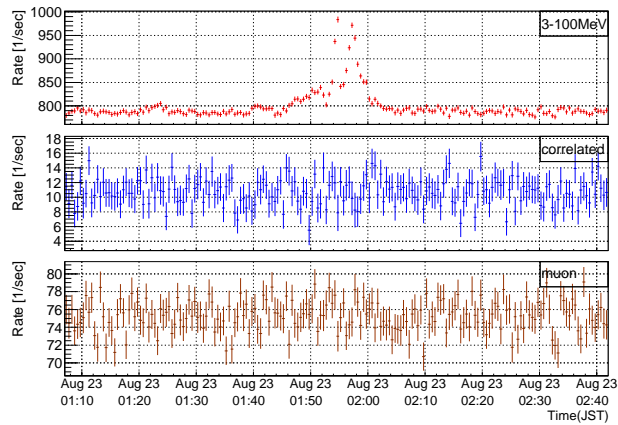
(b) burst20140822-1

(c) burst20140823-1

Figure 8.9: Same as Figure 8.8 but for burst20140731-1, burst20140822-1 and burst20140823-1
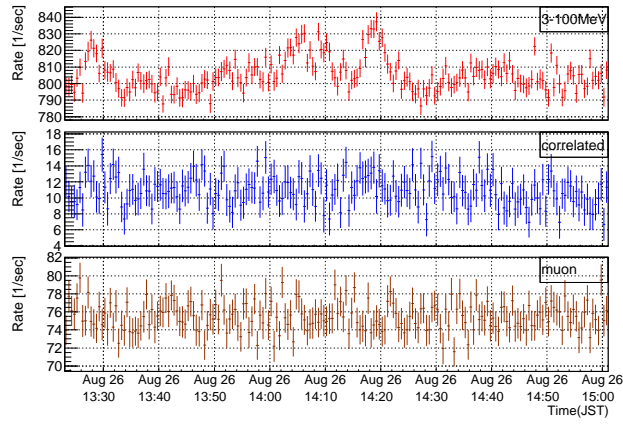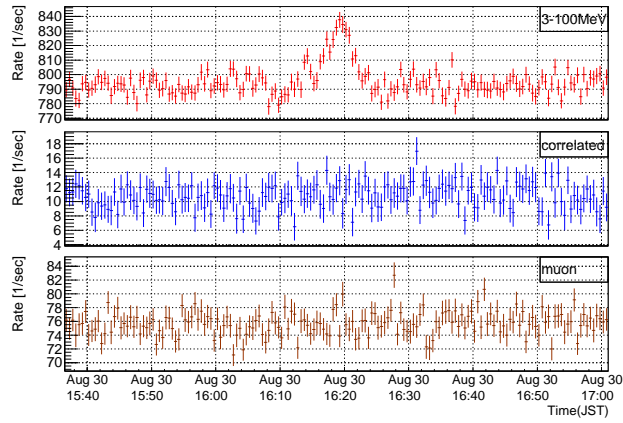
(a) burst20140826-1
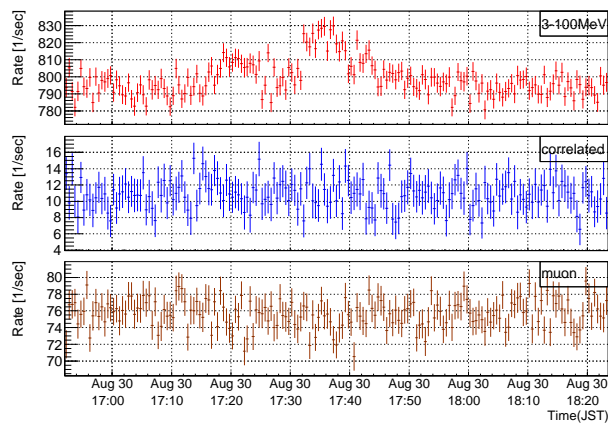
(b) burst20140830-1

(c) burst20140830-2

Figure 8.10: Same as Figure 8.8 but for burst20140826-1, burst20140830-1 and burst20140830-2
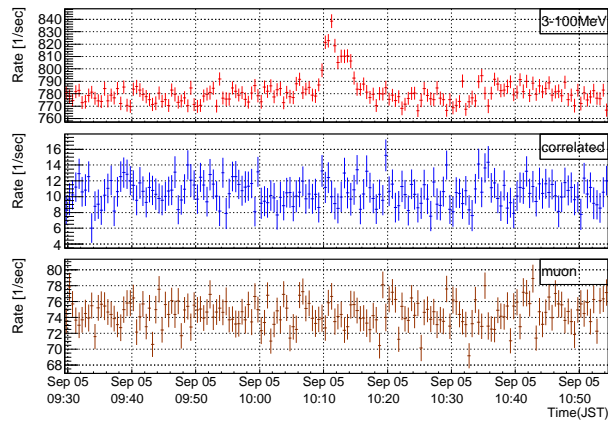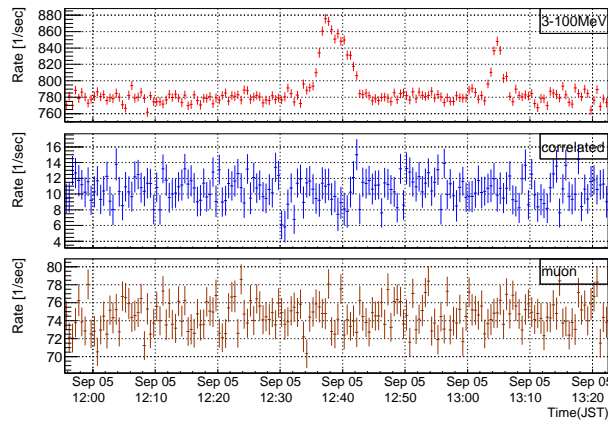
(a) burst20140905-1
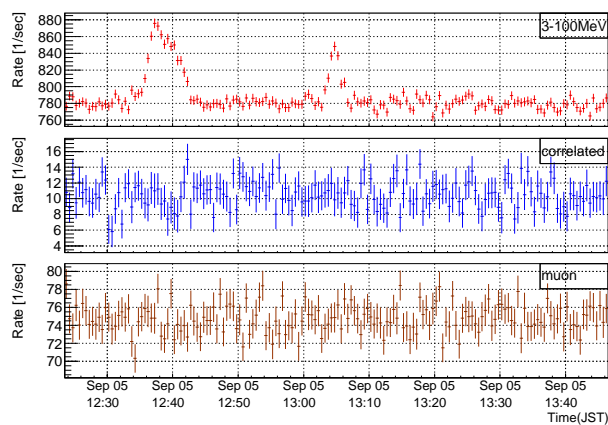
(b) burst20140905-2

(c) burst20140905-3

Figure 8.11: Same as Figure 8.8 but for burst20140905-1, burst20140905-2 and burst20140905-3

Table 8.5: Simulated detection efficiency of PANDA64 against monochromatic neutrons

Neutron energy	Neutron detection efficiency [m^2]	
	isotropic	vertical
10 MeV	0.0182	0.0184
20 MeV	0.0482	0.0491
50 MeV	0.0531	0.0538
100 MeV	0.0895	0.0864

Table 8.6: Correlated event rate during burst periods and its upper limit of several confidence intervals

Burst	Correlated event rate (BG subtracted) [/s]	Upper limit [/s]		
		90 % C.L.	95 % C.L.	99 % C.L.
20140708-1	-0.068 ± 0.495	0.812	0.970	1.277
20140718-1	0.377 ± 0.729	1.573	1.806	2.259
20140719-1	-1.051 ± 0.440	0.722	0.863	1.136
20140731-1	-0.883 ± 0.851	1.395	1.667	2.195
20140822-1	0.382 ± 0.517	1.229	1.394	1.715
20140823-1	0.032 ± 0.449	0.769	0.913	1.191
20140826-1	0.619 ± 0.425	1.316	1.453	1.716
20140830-1	0.094 ± 0.722	1.278	1.509	1.957
20140830-2	0.058 ± 0.493	0.866	1.024	1.330
20140905-1	0.312 ± 0.671	1.412	1.627	2.043
20140905-2	-0.599 ± 0.600	0.984	1.176	1.548
20140905-3	0.184 ± 0.863	1.599	1.876	2.411

Table 8.7: Upper limit (95 % C.L.) of neutron flux around the detector corresponding to four monochromatic neutron energies

Burst	Upper limit of neutron flux (95 % C.L.) [/sec/m^2]			
	10 MeV	20 MeV	50 MeV	100 MeV
20140708-1	53.2	20.1	18.3	10.8
20140718-1	99.1	37.4	34.0	20.2
20140719-1	47.3	17.9	16.3	9.6
20140731-1	91.5	34.6	31.4	18.6
20140822-1	76.5	28.9	26.3	15.6
20140823-1	50.1	18.9	17.2	10.2
20140826-1	79.7	30.1	27.4	16.2
20140830-1	82.8	31.3	28.4	16.9
20140830-2	56.2	21.2	19.3	11.4
20140905-1	89.3	33.7	30.7	18.2
20140905-2	64.5	24.4	22.2	13.1
20140905-3	102.9	38.9	35.3	21.0

Chapter 9

Discussion

9.1 Overview of whole measurement period

Figure 9.1 shows 30-second temporal variation of 3 - 100 MeV count rate, excess against reference count rate, number of grids with each level of Thunder Nowcast and Thunder Information, temperature in the van and electric field strength through whole measurement period. Gray region in the figure corresponds to the period excluded from analysis because of shutdown or maintenance of PANDA64. The electric field data could not be taken during the first half of whole measurement period due to poor connection of a cable. In the figure, 12 observed bursts are drawn as blue vertical lines. It should be noted that two bursts observed on August 30th 2014 and three bursts observed on September 5th 2014 could be seen like wide lines because they were too close.

9.1.1 Count rate

3 - 100 MeV count rate sometimes showed gradual fluctuation during the measurement period, whose fluctuation rate was approximately 10 %/day at maximum. Although it might be related to long operation of PMT or ADC, the cause of the fluctuation could not be identified.

However, the effect would be very small because the fluctuation rate was small enough (< 0.5 %/hour). Since count rate enhancement was searched using reference count rate of two hours prior and posterior to each 30-second time block, the effect on search for bursts would be rather small. Addition-
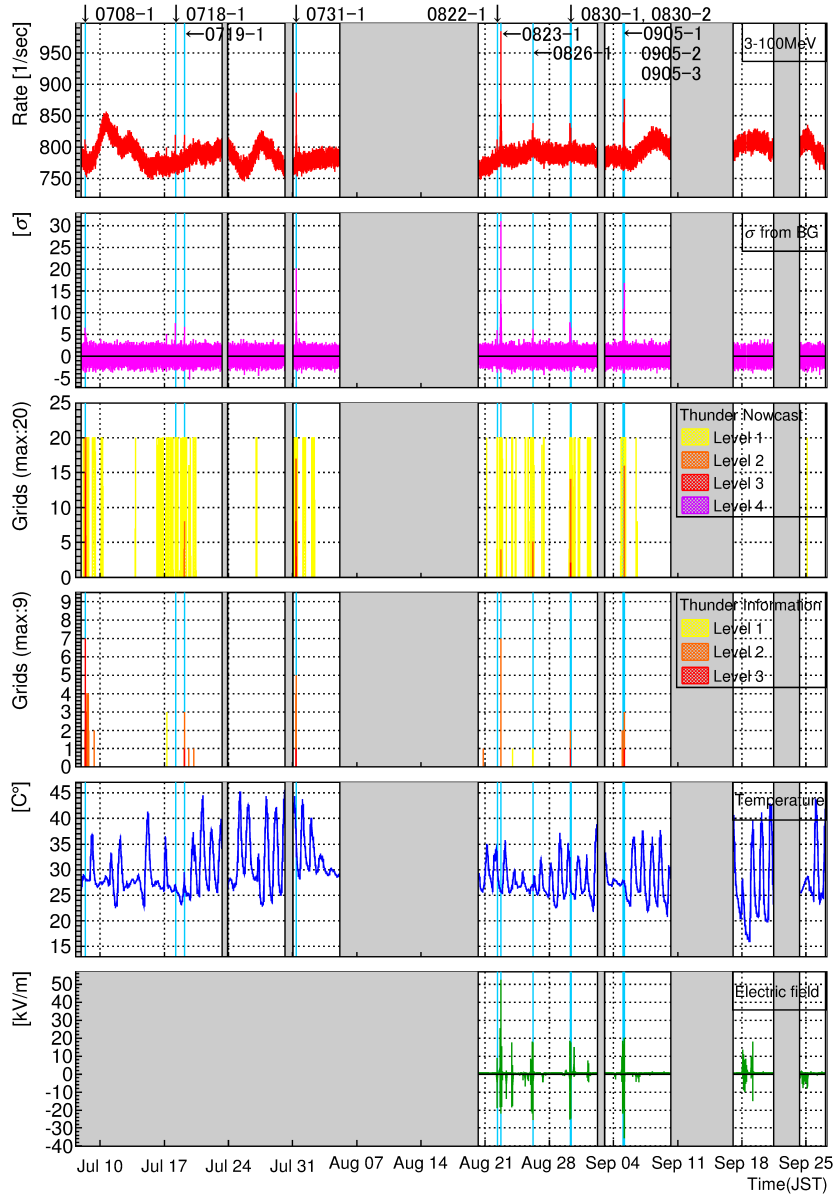
Figure 9.1: 30-second temporal variation of 3 - 100 MeV count rate, excess against reference count rate, number of grids with each level of Thunder Nowcast and Thunder Information, temperature in the van and electric field strength through whole measurement period along with blue vertical lines corresponding to 12 bursts

133

ally, the baseline fluctuation of burst and background periods of 12 bursts would be negligible because these bursts were observed in relatively stable period of count rate.

9.1.2 Electric field

Electric field often showed fluctuation not only in burst periods. Since some of them seemed to be correlated to Level 1 of Thunder Nowcast, there might have existed small scale thunderclouds around the detector although no significant count rate excess of 5 σ could not be observed.

Consequently, the fluctuation of electric field did not necessarily coincide with observation of radiation bursts, although all bursts observed along with electric field data was detected under fluctuation of the electric field.

9.1.3 Thunder Nowcast

Both Thunder Nowcast and Thunder Information seemed to be related to the observed bursts. Especially Level 2 - 4 (shown as orange, red and purple lines) of Thunder Nowcast were obviously coincided with blue lines of bursts in the figure.

As described in 6.2.1, "thunderstorms ($\geq$ Level 2)" were recorded 8 times in 54 days and all of them seemed to be correlated to radiation bursts. In this meaning, the correlation rate of "thunderstorms ($\geq$ Level 2)" with bursts was $8/8 = 1$ and that of "thunderstorms ($\geq$ Level 1)" was $12/121 = 0.099$. However, this correlation rate was based on the assumption that a continuous status of Thunder Nowcast was caused by one thunderstorm.

If each 10-minute data of Level 1 or higher was assumed to be brought by a different thunderstorm, the correlation rate of "thunderstorms ($\geq$ Level 2)" with bursts would be $8/28 = 0.29$ and that of "thunderstorms ($\geq$ Level 1)" would be $12/859 = 0.014$. Furthermore, the correlation rate of "thunderstorms ($\geq$ Level 2)" became $6/28 = 0.21$ under an assumption that a burst which was not observed within 10 minutes from Level 2 or 3 did not correlate to Thunder Nowcast.

9.2 Termination of radiation bursts

9.2.1 Two types of burst termination

There seemed to be two different types of termination of radiation bursts. One type was sudden termination and the other type was gradual termination. As an example, 10-second temporal variation of 3 - 100 MeV count rate and electric field during burst20140823-1 are shown in Figure 9.2.

A sudden termination of count rate enhancement could be seen at around 01:55 A.M. during burst20140823-1. It coincided with sudden fluctuation of electric field from negative to positive. The electric field fluctuated within 1 second and the count rate enhancement terminated almost simultaneously as shown in zoomed Figure 9.3. As shown in the case of burst20140830-1, sudden electric field fluctuation would correspond to a lightning discharge. Therefore, sudden termination of count rate enhancement was inferred to be due to disappearance of electric field caused by a lightning discharge in thunderclouds.

On the other hand, a gradual termination of count rate enhancement could be seen at around 01:58 A.M. during burst20140823-1. In this case, count rate enhancement slowly terminated taking a few minutes while electric field gradually rose from negative to positive. Since the peak shape of count rate enhancement was nearly symmetry, this gradual termination was inferred to be caused by the passage of thundercloud above the detector. This type of termination could be found in most of observed bursts.

9.2.2 Interpretation of burst20140823-1

Here we tried to interpret the correlation between count rate and electric field shown in Figure 9.2. Simple dipole thunderclouds were assumed in the following discussion, which consisted of negative lower layers and positive upper layers.

In Figure 9.2, the first lightning discharge was observed at around 01:52. At that time, strong count rate enhancement was not observed because thunderclouds were not close to the detector as positive electric field showed. Then, electric field turned to negative and an intensive count rate enhance-
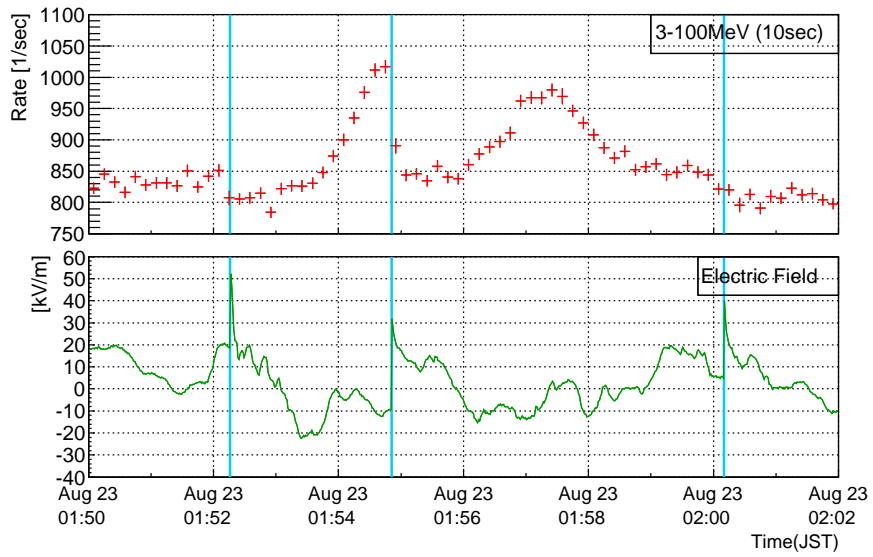
Figure 9.2: 10-second temporal variation of count rate (3 - 100 MeV) and electric field (burst20140823-1) : Blue vertical lines show the sudden fluctuation of electric field which presumably occurred in coincidence with lightning discharges.
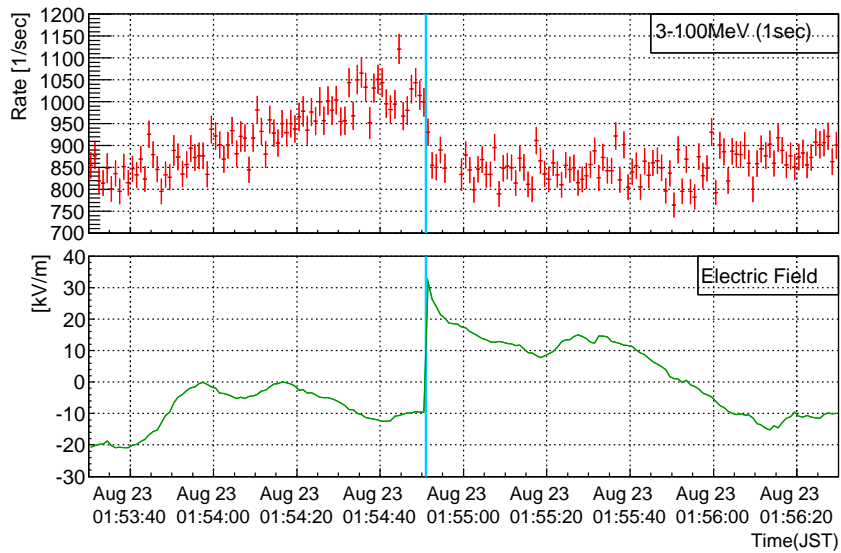
Figure 9.3: Expansion of Figure 9.2 using 1-second temporal variation of count rate (3 - 100 MeV)

ment started (01:53 - 01:55), which indicated that the negative lower layer of thunderclouds came just above the detector.

When the second lightning discharge was observed at 01:55, the count rate enhancement terminated simultaneously with disappearance of electric field. One minute later, a new intensive count rate enhancement appeared at 01:56 - 01:58 because the thundercloud was charged negatively again or another thundercloud came above the detector. However this time, the enhancement terminated gradually taking a few minutes along with slow electric field fluctuation.

The positive value of electric field at around 01:59 showed that the thundercloud had already passed through the detector. When the third lightning discharge was observed at 02:00, thunderclouds were far away and thus no count rate enhancement was observed.

The long-duration bursts have been basically considered to be related to thunderclouds and do not coincide with lightning discharges. Although sudden termination of long-duration electron and gamma-ray bursts in association with lightning discharges were reported respectively [33, 46], the relationship between sudden termination and gradual termination has not been clearly stated because these two termination types were not observed simultaneously.

Burst20140823-1 would be the first example which observed both termination types in a series of bursts. Our group is planning a new experiment of chasing winter thunderclouds in coastal areas of the Sea of Japan by a car equipped with a mobile scintillator in order to observe termination of radiation bursts.

9.3 Difference of observations at Norikura and Ohi

9.3.1 Correlation with Thunder Nowcast

PANDA64 and PANDA36 were almost identical detectors except for the number of modules and the trigger conditions. They were deployed at Norikura Observatory and Ohi Power Station respectively, and both of them detected thundercloud radiation bursts. Mountain areas such as Norikura

Observatory and coastal areas of the Sea of Japan such as Ohi Power Station were typical locations for observation of long duration bursts. The difference of radiation bursts between two locations is discussed below.

Although a number of long duration bursts have been observed at mountains or coastal areas, the correlation with thunder information were seldom reported because it had usually been utilized only to confirm the existence of thunderclouds at the location where signal enhancements were observed. The correlation between radiation bursts and Thunder Nowcast was reported in PANDA36 experiment at Ohi Power Station [2]. It showed that only three radiation bursts were observed in 22 cases of "thunderstorms ($\geq$ Level 2)" although the monitored grids was set wider (20 km $\times$ 20 km) than Norikura. Even when Level 2 grids covered the surrounding area of Ohi Power Station, no count rate enhancement was observed by PANDA36.

On the other hand, PANDA64 detected radiation bursts correlated to all 8 cases of "thunderstorms ($\geq$ Level 2)" without exception. Besides, other 4 bursts were observed during "thunderstorms ($\geq$ Level 1)". The strong correlation between thunder activities and radiation bursts has not been reported before. This result might imply that Norikura's thunderclouds appeared in almost constant altitude, whereas Ohi's thunderclouds appeared in various heights and sometimes bursts could not be detected at the ground surface.

9.3.2 Duration of radiation bursts

Duration of radiation bursts also gave a suggestion about the difference between Norikura and Ohi. The duration of each burst shown in Table 6.1 was defined based on count rate enhancement of 3 σ although some bursts which contain multiple peaks in burst periods should be divided in order to discuss about the typical duration of bursts caused by a thundercloud. Each signal enhancement of Norikura's bursts lasted for 3.0 minutes (e.g. burst20140731-1) up to 9.0 minutes (e.g. burst20140822-1), which was longer than Ohi's bursts (1.5 - 3.0 minutes) or bursts observed in other coastal areas [43, 44]. This might indicate the difference of velocity of thunderclouds or width of electric field in thunderclouds.

138

9.4 Runaway electron flux in the air

9.4.1 Estimation of runaway electron flux

Flux of monochromatic runaway electrons at the most likely source height and energy was calculated based on the simulation results described in 7.2 and 7.3. Arrival rate R_{arrival} and detection efficiency d_{eff} were used for calculation.

At first, peak count rate of particles (i.e. gamma-rays and electrons) detected by PANDA64 was obtained. The peak count rate was the highest count rate among all 30-second time blocks in a burst period. The highest peak count rate among 12 bursts observed at Norikura Observatory was 195.3 ± 6.3[/sec] (burst20140823-1), while the lowest was 31.0 ± 5.4[/sec] (burst20140822-1).

Then, flux at the ground surface f_{ground}[/sec/m^2] corresponding to the peak count rate was calculated by dividing count rate by detection efficiency at the best fit height and energy of runaway electron source. The detection efficiency d_{eff} was obtained from the simulation for detector response by dividing detected count ($E_{\mathrm{tot}} > 3$ MeV) by injected count [/m^2]. As shown in Table 9.1, d_{eff} were approximately 0.5 [m^2] for all 12 bursts. $d_{\mathrm{eff}} \sim 0.5$[/m^2] was rather higher than the detection efficiency of PANDA36 against Ohi's bursts ($d_{\mathrm{eff}} \sim 0.1$[/m^2]) probably due to larger target size and more relaxed trigger condition. Calculated f_{ground} varied from 59.5 to 365.0 [/sec/m^2].

Subsequently, flux in the air at the height of the most likely runaway electron sources f_{air}[/sec/m^2] was calculated by the equation:

$$f_{\mathrm{source}} = f_{\mathrm{ground}}/R_{\mathrm{arrival}}, \qquad (9.1)$$

where R_{arrival} was the arrival rate of gamma-rays and electrons (> 3 MeV) at the ground surface per a runaway electron as is shown in Figure 7.5. The arrival rate differed by a factor of more than 10 among 12 bursts due to difference of the most likely runaway electron sources. It was 0.076 at (1700 m, 50 MeV) as the source of burst20140905-1 and 1.131 at (300 m, 65 MeV) as the source of burst20140905-2. Arrival rate of Ohi's bursts were rather lower because estimated energy of runaway electrons was lower than Norikura's bursts.

The estimated flux at the source height f_{source} are shown for 12 bursts observed at Norikura in Table 9.2 along with the flux at the ground f_{ground} and the peak count rate. f_{source} were estimated to be 1446 ± 139 (95 ± 12) [/sec/m^2] for burst201408231 (burst20140830-1) at maximum (minimum).

In addition, the minimum and maximum values of f_{source} in 90 % confidence region of estimated runaway electron source was obtained from the 2D map of χ^2 values shown in Figure 7.12 - 7.23, which are listed in Table 9.3.

Table 9.1: Simulated detection efficiency and arrival rate at the most likely runaway electron sources of the bursts observed at Norikura Observatory and Ohi Power Station [2]

Location	Burst	Height	Energy	$d_{\mathrm{eff}}[\mathrm{m}^2]$	R_{arrival}
Norikura	20140708-1	1100 m	65 MeV	0.511	0.283
Norikura	20140718-1	400 m	50 MeV	0.521	0.507
Norikura	20140719-1	300 m	55 MeV	0.500	0.724
Norikura	20140731-1	300 m	35 MeV	0.532	0.314
Norikura	20140822-1	900 m	55 MeV	0.520	0.276
Norikura	20140823-1	500 m	40 MeV	0.535	0.284
Norikura	20140826-1	1600 m	95 MeV	0.492	0.295
Norikura	20140830-1	500 m	80 MeV	0.498	0.946
Norikura	20140830-2	700 m	65 MeV	0.509	0.495
Norikura	20140905-1	1700 m	50 MeV	0.535	0.076
Norikura	20140905-2	300 m	65 MeV	0.451	1.131
Norikura	20140905-3	500 m	40 MeV	0.535	0.284
Ohi	20111225	1100 m	16 MeV	0.101	0.003
Ohi	20120102	1100 m	16 MeV	0.101	0.003
Ohi	20120105	400 m	16 MeV	0.096	0.02

9.4.2 Burst flux at Norikura and Ohi

The result of flux calculation of the bursts observed at Norikura Observatory was compared to those observed at Ohi Power Station. Fluxes for three radiation bursts of Ohi Power Station were calculated based on Kuroda's work and shown in Table 9.4. Peak count rate, f_{ground} and f_{source} of each burst observed at Norikura and Ohi are plotted in Figure 9.4.

The peak count rate of radiation bursts observed at Norikura were $O(10^1 - 10^2)$ [/sec]), which were lower than Ohi's count rate ($O(10^2)$ [/sec])

Table 9.2: Peak count rate, flux of bursts incident on the ground surface, and flux of monochromatic runaway electrons at the source height of the bursts

Burst	Peak rate [/sec]	$f_{\text{ground}}[\text{/sec/m}^2]$	$f_{\text{source}}[\text{/sec/m}^2]$
20140708-1	38.0 ± 5.4	74.3 ± 10.5	262 ± 37
20140718-1	43.9 ± 5.8	84.3 ± 11.1	166 ± 22
20140719-1	35.3 ± 5.6	70.6 ± 11.2	98 ± 15
20140731-1	113.4 ± 5.6	212.9 ± 10.6	678 ± 34
20140822-1	31.0 ± 5.4	59.5 ± 10.3	216 ± 37
20140823-1	195.3 ± 6.3	365.0 ± 11.8	1283 ± 42
20140826-1	34.8 ± 5.8	70.7 ± 11.9	240 ± 40
20140830-1	45.0 ± 5.5	90.3 ± 11.0	95 ± 12
20140830-2	32.5 ± 5.6	63.8 ± 11.0	129 ± 22
20140905-1	58.9 ± 5.6	110.0 ± 10.5	1446 ± 139
20140905-2	97.0 ± 5.9	214.9 ± 13.0	190 ± 12
20140905-3	68.2 ± 5.7	127.5 ± 10.7	448 ± 38

Table 9.3: Minimum and maximum values of flux [/sec/m^2] of runaway electrons at the source height in 90 % confidence region

Burst	Lower limit of 90 % C.L.			Upper limit of 90 % C.L.		
	Height	Energy	f_{source}	Height	Energy	f_{source}
20140708-1	400 m	90 MeV	55	1400 m	50 MeV	633
20140718-1	400 m	100 MeV	52	600 m	40 MeV	343
20140719-1	400 m	85 MeV	57	1200 m	30 MeV	1274
20140731-1	200 m	40 MeV	443	800 m	25 MeV	3258
20140822-1	400 m	90 MeV	45	1400 m	40 MeV	799
20140823-1	300 m	40 MeV	914	500 m	40 MeV	1283
20140826-1	500 m	100 MeV	53	1900 m	60 MeV	779
20140830-1	400 m	90 MeV	65	1900 m	55 MeV	1178
20140830-2	400 m	95 MeV	42	1700 m	50 MeV	797
20140905-1	700 m	70 MeV	205	1900 m	40 MeV	2950
20140905-2	400 m	85 MeV	155	300 m	65 MeV	190
20140905-3	300 m	45 MeV	261	1800 m	30 MeV	5727

by a factor of 1.2 - 18. On the other hand, flux at the ground surface (f_{ground}) of Norikura was $O(10^1 - 10^2)$ [/sec/m^2]), while Ohi's bursts had larger f_{ground} of $O(10^3)$ [/sec/m^2] than Norikura's by a factor of 3.8 - 79 due to better detection efficiency of PANDA64 compared to PANDA36. Besides, flux at the estimated source height (f_{source}) of Norikura's bursts was $O(10^1 - 10^3)$ [/sec/m^2]), which were rather smaller than Ohi's f_{source} ($O(10^5 - 10^6)$ [/sec/m^2]) by a factor of 1.7×10^2 - 1.5×10^4. Even when 90 % confidence region of runaway electron sources shown in Table 9.3 was taken into account, Norikura's f_{source} were higher than Ohi's at least by a factor of 42.

The difference of the most likely energy of runaway electrons determined by Monte Carlo simulation caused significant difference in arrival rate R_{arrival} between PANDA36 ($O(10^{-3} - 10^{-2})$) and PANDA64 ($O(10^{-2} - 10^0)$). It led to rather big difference of f_{source}.

Thus, 16 MeV runaway electron sources of Ohi implied very large flux in the air compared to Norikura's bursts. Assuming that the number of seed electrons was common between Norikura and Ohi, radiation bursts observed at Ohi required higher avalanche multiplication factor at least by a factor of 10^2 than Norikura, while the energy of monochromatic runaway electrons at Norikura was higher than Ohi as described in 7.4.

This somewhat confusing result might be attributed to the difference of unknown factor lying between thunderclouds of Norikura and Ohi. Such difference has not been reported before and it indicated the necessity of a new model concerning electron acceleration and multiplication process in electric field of thunderclouds which accounts for long-duration bursts observed at two locations.

Table 9.4: Peak count rate, the flux of bursts incident on the ground surface, and the flux of monochromatic runaway electrons at the source height of the bursts observed at Ohi Power Station calculated based on Kuroda's work [2]

Burst	Peak rate [/sec]	f_{ground}[/sec/m^2]	f_{source}[/sec/m^2]
20111225	$(2.3 \pm 0.1) \times 10^2$	$(1.4 \pm 0.1) \times 10^3$	$(4.7 \pm 0.3) \times 10^5$
20120102	$(5.1 \pm 0.1) \times 10^2$	$(4.1 \pm 0.1) \times 10^3$	$(1.4 \pm 0.0) \times 10^6$
20120105	$(5.5 \pm 0.1) \times 10^2$	$(4.7 \pm 0.2) \times 10^3$	$(2.4 \pm 0.1) \times 10^5$
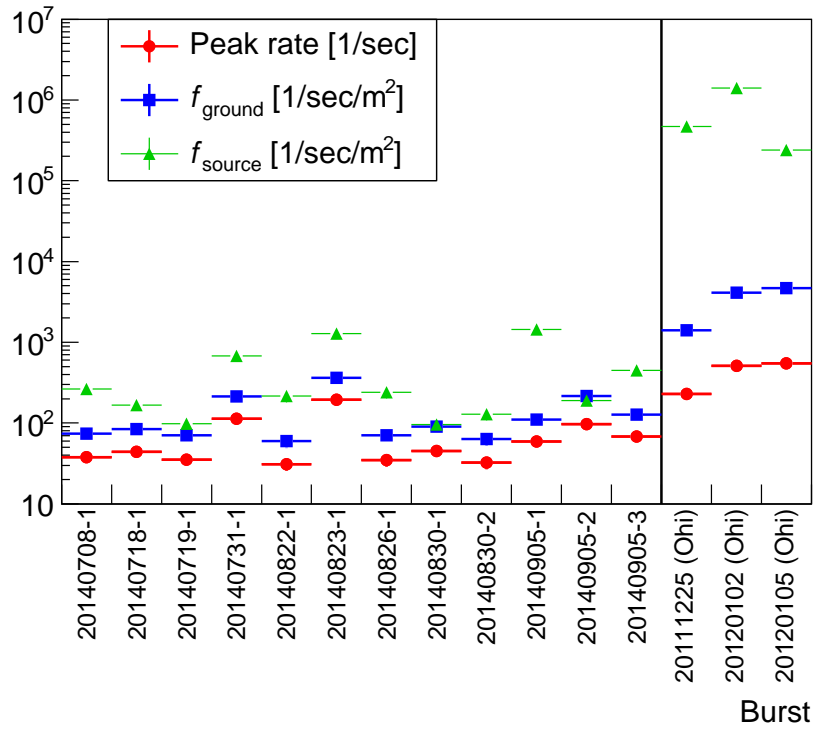
Figure 9.4: Peak count rate, estimated flux on the ground (f_{ground}) and estimated flux at source height (f_{source}) of the bursts observed at Norikura Observatory and Ohi Power Station

Chapter 10

Conclusion

Long-duration radiation bursts related to thunderclouds were observed at a mountaintop using a segmented organic scintillator originally developed as an antineutrino detector for reactor monitoring. The observation was performed at Norikura Observatory (2,770 m above sea level) of The Institute for Cosmic Ray Research, The University of Tokyo in summer of 2014.

During the measurement period, count rate enhancements lasting for a few to ten minutes were observed 12 times in 54 days. Since these enhancements were found in the energy range of > 3 MeV, they were not attributed to the rain fallout of radon and its daughter nuclei. According to Thunder Nowcast, all signal enhancements were observed in temporal and spatial coincidence with Level 1 or higher of thunder activity. Interestingly, signal enhancements were invariably observed whenever Thunder Nowcast indicated thunderstorms of Level 2 or higher in the observation period. Besides, the energy spectra of all signal enhancements extended up to 10 - 25 MeV, which were in good agreement with thundercloud radiation bursts previously observed in mountain areas or coastal areas of the Sea of Japan. Therefore, these 12 signal enhancements were identified as radiation bursts related to thunderclouds. This relatively large number of observed bursts enabled various analysis to investigate the feature of long-duration bursts which seems to have no established theoretical model yet.

Data taken by a field mill and a light sensor installed near the detector gave interesting suggestions regarding correlation with observed bursts. The peak of each burst was observed under strong negative electric field, which

indicated that thunderclouds accelerating electrons downward to the ground existed just above the detector during bursts. In addition, two types of burst termination were detected in this observation. One is sudden termination coinciding with quick electric field fluctuation within 1 second, which would be attributed to lightning discharges. The other is gradual termination taking a few minutes along with slow electric field fluctuation, which would correspond to passage of thunderclouds above the detector. Two different termination types were observed in a series of enhancements lasting for about 10 minutes. The long-duration bursts have been widely considered to be unrelated to lightning discharges in contrast to the short-duration bursts such as TGFs. However, this observation indicated that a long-duration radiation burst might terminate simultaneously with a lightning discharge although this termination type might be rarely observed because thunderclouds usually pass through before occurrence of lightning discharges.

Furthermore, a new suggestion was obtained from energy spectra and Monte Carlo simulation. A simulation was performed in order to estimate height and energy of runaway electron sources. Assuming monochromatic runaway electrons at source height, the most likely height and energy were estimated as 300 - 1700 m and 35 - 95 MeV respectively. The estimated energy was higher than 3 bursts observed at Ohi Power Station. Additionally, runaway electron flux at the source height estimated for Norikura's bursts were remarkably smaller than Ohi's bursts. It meant that the multiplication factor at Norikura was smaller than Ohi at least by a factor of 10^2 if the same number of seed electrons was assumed, whereas runaway electron energy at Norikura was higher than Ohi. The difference implied the necessity of a new model concerning electron acceleration and multiplication process in electric field of thunderclouds.

Chapter 11

Acknowledgments

First of all, I would like to express my sincerest appreciation to Professor M. Minowa, who always led me to right direction for 5 years. Besides, I deeply thank Mr. Y. Inoue for valuable advices on everything from detector development to data analysis.

I am especially grateful to Dr. Y. Kuroda, who made the most important contribution to our project these three years and his work was the initial motivation of my research. I am also grateful to Dr. C. Ito, Dr. S. Oguri and Mr. N. Tomita for their efforts in the reactor monitoring experiment, Professor M. Takita and all members of Norikura Observatory for their cooperation for our observation at Norikura Observatory, Professor K. Makishima, Dr. K. Nakazawa and Mr. D. Umemoto for their advices on radiation burst observation.

Finally, I would like to acknowledge all members of Minowa Group for their support for 5 years.

References

[1] Japan Meteorological Agency. Thunder Nowcast. `http://www.jma.go.jp/jp/radnowc/`.

[2] Y. Kuroda. Observation of gamma ray storms at the earth's surface related to the thunderclouds and a study of their properties. *Ph.D. thesis (The University of Tokyo)*, 2014.

[3] Chubu Electric Power Co., Inc. Thunder Information. `http://www.chuden.co.jp/kisyo/`.

[4] C. T. R. Wilson. The electric field of a thundercloud and some of its effects. *Proceedings of the Physical Society of London*, Vol. 37, No. 1, p. 32D, 1924.

[5] C. T. R. Wilson. The acceleration of -particles in strong electric fields such as those of thunderclouds. *Mathematical Proceedings of the Cambridge Philosophical Society*, Vol. 22, pp. 534–538, 3 1925.

[6] G. K. Parks *et al.* X-ray enhancements detected during thunderstorm and lightning activities. *Geophysical Research Letters*, Vol. 8, No. 11, pp. 1176–1179, 1981.

[7] M. McCarthy, G. K. Parks. Further observations of x-rays inside thunderstorms. *Geophysical Research Letters*, Vol. 12, No. 6, pp. 393–396, 1985.

[8] M. P. McCarthy, G. K. Parks. On the modulation of x ray fluxes in thunderstorms. *Journal of Geophysical Research: Atmospheres*, Vol. 97, No. D5, pp. 5857–5864, 1992.

[9] K. Olive et al. Review of Particle Physics. *Chin.Phys.*, Vol. C38, p. 090001, 2014.

[10] Y.-S. Tsai. Pair production and bremsstrahlung of charged leptons. *Rev. Mod. Phys.*, Vol. 46, pp. 815–851, Oct 1974.

[11] A. Gurevich, G. Milikh, R. Roussel-Dupre. Runaway electron mechanism of air breakdown and preconditioning during a thunderstorm. *Physics Letters A*, Vol. 165, No. 5-6, pp. 463 – 468, 1992.

[12] J. R. Dwyer. A fundamental limit on electric fields in air. *Geophysical Research Letters*, Vol. 30, No. 20, p. 2055, 2003.

[13] A. Gurevich, G. Milikh. Generation of x-rays due to multiple runaway breakdown inside thunderclouds. *Physics Letters A*, Vol. 262, No. 6, pp. 457 – 463, 1999.

[14] A. Gurevich *et al.* Kinetic theory of runaway breakdown in inhomogeneous thundercloud electric field. *Physics Letters A*, Vol. 282, No. 3, pp. 180 – 185, 2001.

[15] L. Babich *et al.* Fundamental parameters of a relativistic runaway electron avalanche in air. *Plasma Physics Reports*, Vol. 30, No. 7, pp. 616–624, 2004.

[16] J. R. Dwyer. Relativistic breakdown in planetary atmospheres. *Physics of Plasmas (1994-present)*, Vol. 14, No. 4, p. 042901, 2007.

[17] G. J. Fishman *et al.* Discovery of intense gamma-ray flashes of atmospheric origin. *Science*, Vol. 264, No. 5163, pp. 1313–1316, 1994.

[18] D. M. Smith *et al.* Terrestrial gamma-ray flashes observed up to 20 mev. *Science*, Vol. 307, No. 5712, pp. 1085–1088, 2005.

[19] B. W. Grefenstette *et al.* First rhessi terrestrial gamma ray flash catalog. *Journal of Geophysical Research: Space Physics*, Vol. 114, No. A2, p. A02314, 2009.

[20] M. S. Briggs *et al.* First results on terrestrial gamma ray flashes from the fermi gamma-ray burst monitor. *Journal of Geophysical Research: Space Physics*, Vol. 115, No. A7, p. A07323, 2010.

[21] M. Marisaldi *et al.* Detection of terrestrial gamma ray flashes up to 40 mev by the agile satellite. *Journal of Geophysical Research: Space Physics*, Vol. 115, No. A3, p. A00E13, 2010.

[22] C. B. Moore *et al.* Energetic radiation associated with lightning stepped-leaders. *Geophysical Research Letters*, Vol. 28, No. 11, pp. 2141–2144, 2001.

[23] J. R. Dwyer *et al.* X-ray bursts associated with leader steps in cloud-to-ground lightning. *Geophysical Research Letters*, Vol. 32, No. 1, p. L01803, 2005.

[24] S. Yoshida *et al.* High energy photon and electron bursts associated with upward lightning strokes. *Geophysical Research Letters*, Vol. 35, No. 10, p. L10804, 2008.

[25] A. Chilingarian, G. Hovsepyan, A. Hovhannisyan. Particle bursts from thunderclouds: Natural particle accelerators above our heads. *Phys. Rev. D*, Vol. 83, p. 062001, Mar 2011.

[26] J. R. Dwyer *et al.* Observation of a gamma-ray flash at ground level in association with a cloud-to-ground lightning return stroke. *Journal of Geophysical Research: Space Physics*, Vol. 117, No. A10, p. A10303, 2012.

[27] J. R. Dwyer *et al.* Energetic radiation produced during rocket-triggered lightning. *Science*, Vol. 299, No. 5607, pp. 694–697, 2003.

[28] J. R. Dwyer *et al.* Measurements of x-ray emission from rocket-triggered lightning. *Geophysical Research Letters*, Vol. 31, No. 5, p. L05118, 2004.

[29] J. R. Dwyer *et al.* A ground level gamma-ray burst observed in association with rocket-triggered lightning. *Geophysical Research Letters*, Vol. 31, No. 5, p. L05119, 2004.

[30] K. B. Eack *et al.* Initial results from simultaneous observation of x-rays and electric fields in a thunderstorm. *Journal of Geophysical Research: Atmospheres*, Vol. 101, No. D23, pp. 29637–29640, 1996.

[31] M. Brunetti *et al.* Gamma-ray bursts of atmospheric origin in the mev energy range. *Geophysical Research Letters*, Vol. 27, No. 11, pp. 1599–1602, 2000.

[32] A. Chubenko *et al.* Intensive x-ray emission bursts during thunderstorms. *Physics Letters A*, Vol. 275, No. 1-2, pp. 90 – 100, 2000.

[33] V. Alexeenko *et al.* Transient variations of secondary cosmic rays due to atmospheric electric field and evidence for pre-lightning particle acceleration. *Physics Letters A*, Vol. 301, No. 3-4, pp. 299 – 306, 2002.

[34] Y. Muraki *et al.* Effects of atmospheric electric fields on cosmic rays. *Phys. Rev. D*, Vol. 69, p. 123010, Jun 2004.

[35] H. Tsuchiya *et al.* Observation of an energetic radiation burst from mountain-top thunderclouds. *Phys. Rev. Lett.*, Vol. 102, p. 255003, Jun 2009.

[36] T. Torii *et al.* Gradual increase of energetic radiation associated with thunderstorm activity at the top of mt. fuji. *Geophysical Research Letters*, Vol. 36, No. 13, p. L13804, 2009.

[37] A. Chilingarian *et al.* Ground-based observations of thunderstorm-correlated fluxes of high-energy electrons, gamma rays, and neutrons. *Phys. Rev. D*, Vol. 82, p. 043009, Aug 2010.

[38] A. Chilingarian *et al.* Remarks on recent results on neutron production during thunderstorms. *Phys. Rev. D*, Vol. 86, p. 093017, Nov 2012.

[39] H. Tsuchiya *et al.* Observation of thundercloud-related gamma rays and neutrons in tibet. *Phys. Rev. D*, Vol. 85, p. 092006, May 2012.

[40] N. Kitagawa, K. Michimoto. Meteorological and electrical aspects of winter thunderclouds. *Journal of Geophysical Research: Atmospheres*, Vol. 99, No. D5, pp. 10713–10721, 1994.

[41] T. Torii, M. Takeishi, T. Hosono. Observation of gamma-ray dose increase associated with winter thunderstorm and lightning activity. *Journal of Geophysical Research: Atmospheres*, Vol. 107, No. D17, pp. ACL 2–1–ACL 2–13, 2002.

[42] T. Torii *et al.* Downward emission of runaway electrons and bremsstrahlung photons in thunderstorm electric fields. *Geophysical Research Letters*, Vol. 31, No. 5, p. L05113, 2004.

[43] H. Tsuchiya *et al.* Detection of high-energy gamma rays from winter thunderclouds. *Phys. Rev. Lett.*, Vol. 99, p. 165002, Oct 2007.

[44] H. Tsuchiya *et al.* Long-duration ray emissions from 2007 and 2008 winter thunderstorms. *Journal of Geophysical Research: Atmospheres*, Vol. 116, No. D9, p. D09113, 2011.

[45] T. Torii *et al.* Migrating source of energetic radiation generated by thunderstorm activity. *Geophysical Research Letters*, Vol. 38, No. 24, p. L24801, 2011.

[46] H. Tsuchiya *et al.* Hardening and termination of long-duration γ rays detected prior to lightning. *Phys. Rev. Lett.*, Vol. 111, p. 015001, Jul 2013.

[47] L. P. Babich *et al.* Source of prolonged bursts of high-energy gamma rays detected in thunderstorm atmosphere in japan at the coastal area of the sea of japan and on high mountaintop. *Journal of Geophysical Research: Space Physics*, Vol. 115, No. A9, p. A09317, 2010.

[48] G. N. Shah *et al.* Neutron generation in lightning bolts. *Nature*, Vol. 313, No. 6005, pp. 773–775, 1985.

[49] A. Shyam, T. C. Kaushik. Observation of neutron bursts associated with atmospheric lightning discharge. *Journal of Geophysical Research: Space Physics*, Vol. 104, No. A4, pp. 6867–6869, 1999.

[50] A. V. Gurevich *et al.* Strong flux of low-energy neutrons produced by thunderstorms. *Phys. Rev. Lett.*, Vol. 108, p. 125001, Mar 2012.

[51] S. Starodubtsev *et al.* First experimental observations of neutron bursts under thunderstorm clouds near sea level. *JETP Letters*, Vol. 96, No. 3, pp. 188–191, 2012.

[52] L. M. Libby, H. R. Lukens. Production of radiocarbon in tree rings by lightning bolts. *Journal of Geophysical Research*, Vol. 78, No. 26, pp. 5902–5903, 1973.

[53] R. L. Fleischer, J. A. Plumer, K. Crouch. Are neutrons generated by lightning? *Journal of Geophysical Research*, Vol. 79, No. 33, pp. 5013–5017, 1974.

[54] L. P. Babich, R. A. Roussel-Dupré. Origin of neutron flux increases observed in correlation with lightning. *Journal of Geophysical Research: Atmospheres*, Vol. 112, No. D13, p. D13303, 2007.

[55] S. S. Dietrich, B. L. Berman. Atlas of photoneutron cross sections obtained with monoenergetic photons. *Atomic Data and Nuclear Data Tables*, Vol. 38, No. 2, pp. 199 – 338, 1988.

[56] L. Babich *et al.* On amplifications of photonuclear neutron flux in thunderstorm atmosphere and possibility of detecting them. *JETP Letters*, Vol. 97, No. 6, pp. 291–296, 2013.

[57] L. Babich. Fundamental processes capable of accounting for the neutron flux enhancements in a thunderstorm atmosphere. *Journal of Experimental and Theoretical Physics*, Vol. 118, No. 3, pp. 375–383, 2014.

[58] L. P. Babich *et al.* Analysis of fundamental interactions capable of producing neutrons in thunderstorms. *Phys. Rev. D*, Vol. 89, p. 093010, May 2014.

[59] H. Tsuchiya. Surrounding material effect on measurement of thunderstorm-related neutrons. *Astroparticle Physics*, Vol. 57-58, pp. 33 – 38, 2014.

[60] IAEA Headquarters. Final Report: Focused Workshop on Antineutrino Detection for safeguards Applications, 2008.

152

[61] N. Bowden *et al.* Experimental results from an antineutrino detector for cooperative monitoring of nuclear reactors. *Nuclear Instruments and Methods in Physics Research Section A: Accelerators, Spectrometers, Detectors and Associated Equipment*, Vol. 572, No. 2, pp. 985 – 998, 2007.

[62] H. Furuta *et al.* A study of reactor neutrino monitoring at the experimental fast reactor joyo. *Nuclear Instruments and Methods in Physics Research Section A: Accelerators, Spectrometers, Detectors and Associated Equipment*, Vol. 662, No. 1, pp. 90 – 100, 2012.

[63] C. L. Cowan *et al.* Detection of the free neutrino: a confirmation. *Science*, Vol. 124, No. 3212, pp. 103–104, 1956.

[64] Y. Klimov *et al.* Neutrino method remote measurement of reactor power and power output. *Atomic Energy*, Vol. 76, No. 2, pp. 123–127, 1994.

[65] Y. Kuroda *et al.* A mobile antineutrino detector with plastic scintillators. *Nuclear Instruments and Methods in Physics Research Section A: Accelerators, Spectrometers, Detectors and Associated Equipment*, Vol. 690, pp. 41 – 47, 2012.

[66] S. Oguri *et al.* Reactor antineutrino monitoring with a plastic scintillator array as a new safeguards method. *Nuclear Instruments and Methods in Physics Research Section A: Accelerators, Spectrometers, Detectors and Associated Equipment*, Vol. 757, pp. 33 – 39, 2014.

[67] D. M. Suszcynsky, R. Roussel-Dupre, G. Shaw. Ground-based search for x rays generated by thunderstorms and lightning. *Journal of Geophysical Research: Atmospheres*, Vol. 101, No. D18, pp. 23505–23516, 1996.

[68] S. Agostinelli *et al.* Geant4 - a simulation toolkit. *Nuclear Instruments and Methods in Physics Research Section A: Accelerators, Spectrometers, Detectors and Associated Equipment*, Vol. 506, No. 3, pp. 250 – 303, 2003.